

A Computational Study of the Inertial Collapse of Gas Bubbles Near a Rigid Surface

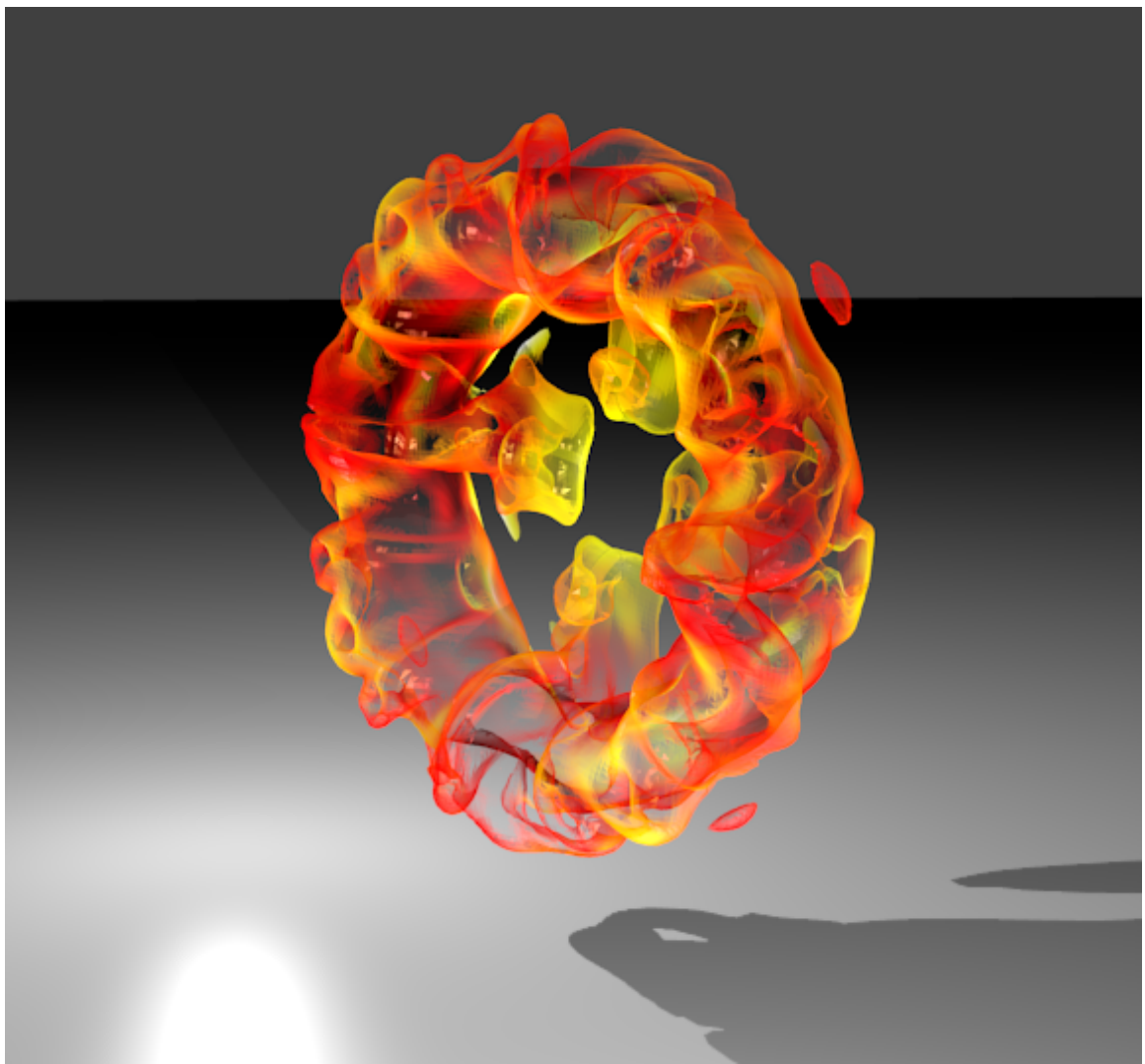
by

Shahaboddin Alahyari Beig

A dissertation submitted in partial fulfillment
of the requirements for the degree of
Doctor of Philosophy
(Mechanical Engineering)
in the University of Michigan
2018

Doctoral Committee:

Associate Professor Eric Johnsen, Chair
Dr. Charlotte N. Barbier, Oak Ridge National Laboratory
Professor Steven L. Ceccio
Professor Kenneth G. Powell
Professor Venkat Raman



Shahaboddin Alahyari Beig

alahyari@umich.edu

ORCID iD: 0000-0002-6865-4858

© Shahaboddin Alahyari Beig 2018

All Rights Reserved

DEDICATION

To my family.

ACKNOWLEDGMENTS

Five years ago, Prof. Eric Johnsen, welcomed me into his group as a Ph.D. student. He believed in me and my potential enough to bring me all the way from Iran and fully support me from day one. He is the reason this dissertation exists today. For his mentorship over the past five years, I am very grateful. I would like to thank my committee members, Prof. Steven Ceccio, Prof. Venkat Raman, Prof. Kenneth Powell, and Dr. Charlotte Barbier for their time and advice towards my dissertation.

I have been lucky enough to make lasting friendships with the people I have worked with in the Autolab: Pooya, Marc, Brandon, Mauro, Anil, Phil, Sam, Kevin, Siddhesh, Suyash, T. J., and Brian. You are all such amazing people and it has been an honor to learn from and work alongside you all. I am eternally indebted to my parents for always putting their wants and needs second to my own in order for me to get further in life. Though my physical absence from their lives has been difficult, they never complained. Thank you, Maman and Baba. A very special thanks to my entire family back home as well, for always keeping me in their prayers, especially Madar, Baba Haji, Maman Ashraf, and Baba Ahmad. Since getting married, my in-laws have become like a second set of parents. They were always there for me when the pressures of graduate school got high, and provided me with encouragement and peace of mind. The most important person I would like to acknowledge is my darling wife, Sahar, who could not have been more supportive, caring, and considerate throughout this whole process. I am blessed to have such a strong and patient woman by my side for the rest of my life. All praise is due to Allah. The Beneficent, the Merciful.

This work was supported by ONR grant N00014-12-1-0751 under Dr. Ki-Han Kim and used resources from the Extreme Science and Engineering Discovery Environment (XSEDE), supported by National Science Foundation grant number ACI-1053575, and Blue Waters, supported by the National Science Foundation (awards OCI-0725070 and ACI-1238993) and the state of Illinois.

TABLE OF CONTENTS

Dedication	ii
Acknowledgments	iii
List of Figures	viii
List of Tables	xi
List of Abbreviations	xii
Abstract	xiii

CHAPTER

1 Introduction	1
1.1 Cavitation in science and engineering	1
1.2 Cavitation erosion	5
1.3 Bubble dynamics	7
1.3.1 Collapse of bubble clouds	7
1.3.2 Single-bubble dynamics	8
1.3.3 Numerical simulations	10
1.4 Thesis overview	12
Part I: A numerical model for multiphase flows	15

CHAPTER

2 Maintaining interface equilibrium conditions in compressible multiphase flows using interface capturing	16
2.1 Abstract	16
2.2 Introduction	17
2.3 Physical model	20
2.3.1 Equations of motion	20
2.3.2 Equation of state	20
2.3.3 Multifluid modeling	21
2.3.3.1 Definitions and basic relations	21
2.3.3.2 Mixture relations	22
2.3.3.3 Transport equation	24
2.4 Numerical models	24
2.5 Analysis of the temperature errors	26
2.5.1 Occurrence of temperature errors	26
2.5.2 Eliminating temperature errors for the different approaches	28
2.5.2.1 γ -based approach	28

2.5.2.2	Volume fraction approach	29
2.5.2.3	Mass fraction approach	31
2.5.3	Summary of the analysis	32
2.6	Numerical implementation	33
2.7	Results	36
2.7.1	1D smooth advection problem	36
2.7.2	1D air/water interface advection	37
2.7.3	1D gas-liquid Riemann problem	38
2.7.4	3D shock-bubble interaction	39
Part II:	Bubble dynamics	48

CHAPTER

3	Physical/numerical modeling	49
3.1	Governing equations	49
3.2	Equation of state	50
3.3	Multiphase model	51
3.4	Numerical framework	52
3.5	Problem description	56
3.5.1	Rayleigh collapse of an isolated vapor bubble in a free field	57
3.5.2	Rayleigh collapse of a single vapor bubble near a rigid boundary	57
3.5.3	Rayleigh collapse of a vapor bubble pair near a rigid surface	58
3.5.4	Grid dependence	60
4	Non-spherical collapse of a single bubble near a rigid wall	61
4.1	Abstract	61
4.2	Spherical collapse	62
4.3	Non-spherical bubble dynamics	67
4.3.1	Jet formation	71
4.3.2	Bubble morphology and collapse non-sphericity	73
4.3.3	Jet velocity	81
4.4	Jet impact, bubble collapse, and shock propagation due to non-spherical bubble collapse	84
4.5	Wall pressures achieved by non-spherical bubble collapse	90
5	Temperatures produced by collapsing a vapor bubble near a rigid wall	93
5.1	Abstract	93
5.2	Introduction	94
5.3	Fluid temperatures produced by a collapsing bubble	95
5.4	Temperature in the Solid	104
6	Inertial collapse of bubble pairs near a rigid wall	108
6.1	Abstract	108
6.2	Introduction	108
6.3	Qualitative dynamics	110
6.4	Jet formation	114

6.4.1	Secondary bubble	116
6.4.2	Primary bubble	118
6.5	Collapse properties	120
6.6	Wall pressure	122
7	Conclusions and future work	125
7.1	Concluding remarks	125
7.1.1	Numerical approach	125
7.1.2	Flow physics	126
7.2	Recommendations for future research directions	129
7.2.1	Physical model	129
7.2.2	Numerical framework	130
7.2.3	Physical investigations	132
Appendix	134
Bibliography	136

LIST OF FIGURES

1.1	Cavity formation	2
1.2	Shock propagation and light emission	3
1.3	Cavitation-induced damage in different applications	4
1.4	Liquid jet formation	9
2.1	L_∞ error for the 1D smooth advection problem	37
2.2	Profile of the advection of an air/water interface after one period	38
2.3	Time histories of normalized L_∞ errors for the advection of an air/water interface after one period	39
2.4	Gas-liquid Riemann problem	40
2.5	Gas-liquid Riemann problem (1D shock-interface)	41
2.6	Shock-induced bubble collapse (case 1, $p_s/p_o = 100$)	43
2.7	Shock-induced bubble collapse (case 2, $p_s/p_o = 1000$)	44
2.8	Shock-induced bubble collapse (case 1, $p_s/p_o = 100$) – Centerline properties	45
2.9	Shock-induced bubble collapse (case 2, $p_s/p_o = 1000$) – Centerline properties	46
2.10	Shock-induced bubble collapse (case 1, $p_s/p_o = 100$) – Time histories	47
2.11	Shock-induced bubble collapse (case 2, $p_s/p_o = 1000$) – Time histories	47
3.1	Weak scaling of the computational code	55
3.2	Strong scaling of the computational code	56
3.3	Schematic of problem setup for Rayleigh collapse of a single vapor bubble near a rigid boundary	58
3.4	Schematic of problem setup for Rayleigh collapse of a vapor bubble pair near a rigid surface	59
3.5	Convergence analysis	60
4.1	Collapse of an isolated bubble in an infinite medium	63
4.2	Time history of bubble radius and pressure at the bubble centre	64
4.3	Liquid pressure versus distance at different instances	66
4.4	Non-spherical collapse of a single bubble near a rigid boundary	70
4.5	Normalized velocity magnitude of the bubble interface as a function of angle at different times	72
4.6	Normalized pressure distribution along the centerline at different instances	73
4.7	Bubble shape and jet formation	74

4.8	The evolution of the bubble shape throughout the collapse for different δ_o and $p_\infty = 5$ MPa	75
4.9	Schematic of the bubble collapse.	76
4.10	Non-sphericity as a function of time	77
4.11	Collapse non-sphericity for varying initial stand-off distances	78
4.12	Normalized minimum volume (collapse intensity) as a function of non-sphericity for different driving pressure.	78
4.13	Bubble centroid location as a function of time	80
4.14	Bubble displacement and centroid location at collapse as a function of initial stand-off for different driving pressures	81
4.15	Time evolution of the jet and distal velocity for three different stand-off distances at $p_\infty = 5$ MPa	82
4.16	Maximum jet velocity vs. initial bubble stand off for different driving pressures	83
4.17	Normalized time difference between the jet impact and collapse as a function of initial stand-off distance for different driving pressure	85
4.18	Formation of different shock waves during the collapse of a single bubble near a rigid surface, with $\delta_o = 2.5$ and $p_\infty = 5$ MPa	86
4.19	Jet impact and shock propagation for different initial bubble stand-off distances, with $p_\infty = 5$ MPa	87
4.20	Shock pressure as a function of angle at $r/R_o = 0.9$ for different initial bubble stand-off with $p_\infty = 5$ MPa, and shock pressure as a function of angle at $\delta_o = 2.5$ for different radial distances from the shock origin with $p_\infty = 5$ MPa	88
4.21	Normalized shock pressure as a function of angle, and maximum shock pressure vs. radial distances from the shock origin at $\delta_o = 2.5$ for different radial distances from the shock origin with $p_\infty = 5$ MPa	89
4.22	Time history of wall pressure along the centerline for different initial stand-off distances with $p_\infty = 5$ MPa	90
4.23	Maximum pressure along the wall as a function of collapse location for different driving pressures	91
4.24	The normalized radius of the affected area where the pressure exceeds the criteria of $p/(\rho_l a_i^2 \Delta p)^{1/2} > 1$, as a function of initial stand-off distance for different driving pressures	92
5.1	Time history of bubble radius and temperature in a spherical collapse of an isolated bubble in water	96
5.2	Rayleigh collapse near a rigid wall ($\delta_o = 1.25$, $p_\infty = 5$ MPa). Top: 3D contours of the bubble's shape colored by temperature. Bottom: 2D slices of temperature (top) and pressure (bottom); white dashed line: initial bubble interface.	97
5.3	Time-evolution of the average bubble temperature and centroid distance from the wall	98
5.4	Maximum average bubble temperature vs. initial stand-off distance	99
5.5	Maximum fluid temperature rise along the wall vs. initial stand-off distance	100
5.6	Normalized time difference between minimum volume and maximum fluid temperature rise along the wall vs. initial stand-off distance	101
5.7	Temperature contours and line along the wall	102
5.8	Scaling of the collapse location vs. δ_o for different driving pressures	103

5.9	Scaling of the maximum fluid temperature rise along the wall vs. δ_o for different driving pressure	104
5.10	Schematic of the thermal boundary layer between the hot fluid and the wall.	105
5.11	Temperature rise of the wall surface for different materials vs. initial stand-off distance	107
6.1	Collapse of a bubble pair near a rigid surface	113
6.2	Schematic of mechanisms inducing the jet formation in the collapse of bubble pairs near a rigid wall	115
6.3	Jet of the secondary bubble at different angles	117
6.4	Jet angle as a function of the initial angle ϕ	117
6.5	Jet of the primary bubble at different angles	118
6.6	Jet and migration angles as a function of the initial angle ϕ	119
6.7	Occurrence of the double jetting event during the collapse of a bubble pair near a wall	119
6.8	Collapse time as a function of the initial angle ϕ	121
6.9	Collapse location as a function of the initial angle ϕ	122
6.10	Collapse pressure as a function of the initial angle ϕ	123
6.11	Maximum wall pressure as a function of the initial angle ϕ	124

LIST OF TABLES

2.1	Relevant constants for the stiffened equation of state.	21
3.1	Relevant constants in the Nobel-Abel Stiffened-Gas equation of state equation of state for water.	51

LIST OF ABBREVIATIONS

EOS Equation of state

HDF Hierarchical Data Format

HPC High-performance computing

MPI Message Passing Interface

NASG Nobel-Abel Stiffened-Gas equation of state

HLL Harten-Lax-van Leer Riemann solver

RC Rayleigh collapse

RP Rayleigh-Plesset equation

UHMWPE Ultra High Molecular Weight Polyethylene

WENO Weighted Essentially Non-Oscillatory

ABSTRACT

Cavitation research is essential to a variety of applications ranging from naval hydrodynamics to medicine and energy sciences. Vapor cavities can grow from sub-micron-sized nuclei to millimeter-sized bubbles, and collapse violently in an inertial fashion. This implosion, which concentrates energy into a small volume, can produce high pressures and temperatures, generate strong shock waves, and even emit visible light. One of the main consequences of cavitation is structural damage to neighboring surfaces due to bubble collapse.

The propagation of shock and rarefaction waves in a multiphase medium results in a complicated multiscale and multiphysics problem. Laboratory experiments of such flows are challenging due to the wide range of spatial and temporal scales, difficult optical access, and limitations of measurement devices. To better understand these flows, we use highly resolved numerical simulations of the inertial collapse of individual vapor bubbles near a rigid surface. For this purpose, we developed a novel numerical multiphase model combined with high-performance computing techniques to perform accurate and efficient simulations of the three-dimensional compressible Navier-Stokes equations for a binary, gas-liquid system. We present the detailed dynamics of the Rayleigh collapse of a single vapor bubble near a rigid wall for different geometrical configurations and driving pressures. We explain that the presence of a rigid boundary breaks the symmetry of the collapse and hinders the energy concentration. As a result, a liquid re-entrant jet directed toward the wall forms, ultimately giving rise to lower pressure and temperatures produced upon collapse. We characterize the collapse non-sphericity, and show that this quantity, which strongly depends on the initial stand-off distance of the bubble from the wall, significantly affects the overall dynamics. We further show that bubbles initially close to the wall or attached to the surface are responsible not

only for the high pressure loads along the wall, but also the elevated temperatures on the solid surface. In fact, for certain soft materials, instantaneous temperatures greater than the melting point may be achieved on the surface, thus confirming that thermal damage is a potential threat to such materials exposed to cavitating flows. Furthermore, the development of scalings for important collapse properties (jet velocity, shock pressure, wall pressures/temperatures), in terms of the initial stand-off distance and driving pressure, not only illustrates universality of non-spherical bubble dynamics but also provides means to predict these phenomena.

Since real flows involve many bubbles, we also investigate the inertial collapse of a pair of vapor bubbles near a rigid surface. We explain that the presence of a second bubble in the vicinity of the original (primary) bubble leads to far more complicated dynamics and completely changes the single-bubble scalings. Strong interactions between the bubbles and the boundary drastically increase the collapse non-sphericity and amplify/hinder the pressures and temperatures produced by the collapse. Our simulations show that the re-entrant jets in both bubbles form at distorted angles, and for certain configurations, “double jetting”, occurs, in which two jets penetrate the primary bubble. The results indicate that bubble-bubble interactions and their effects on collapse dynamics near a wall are non-negligible. Furthermore, given the complexity of even this simple problem and the large number of parameters, the value of extending such high-resolution simulations to develop scalings for the collapse of many bubbles is debatable at the present time; it may be worth considering alternative modeling approaches.

CHAPTER 1

Introduction

This chapter presents a brief introduction on cavitation bubble dynamics, the structural damage due to the inertial collapse of bubbles, and relevant applications in science and engineering. First, a general description of cavitation phenomena is provided; the relevance of this problem to a variety of applications, as well as the motivations behind this study are emphasized. Then, a brief review of past analytical, experimental, and numerical studies regarding cavitation bubble dynamics is performed. At the end, this chapter provides an overview of the thesis, objectives, and main contributions of the present study.

1.1 Cavitation in science and engineering

Cavitation, the process whereby vapor cavities are produced in a liquid, is a ubiquitous phenomenon in high-Reynolds number flows of liquids (Brennen, 1995). In contrast with boiling, in which liquid vaporizes as the temperature rises, cavitation happens due to local pressure reductions; Figure 1.1 shows the inception of cavitation in low-pressure regions, produced by separated shear flow when liquid water passes over a wedge.

Decreases in pressure caused by velocity changes in a liquid may lead to the formation of small-scale vapor bubbles, which dynamically respond to the surrounding flow field by growing and collapsing, sometimes with extreme violence. During the collapse, the cavitation bubbles undergo a rapid compression such that the bubble volume decreases by several orders of magnitude; this implosion, usually occurring within a few microseconds, concentrates energy into a small

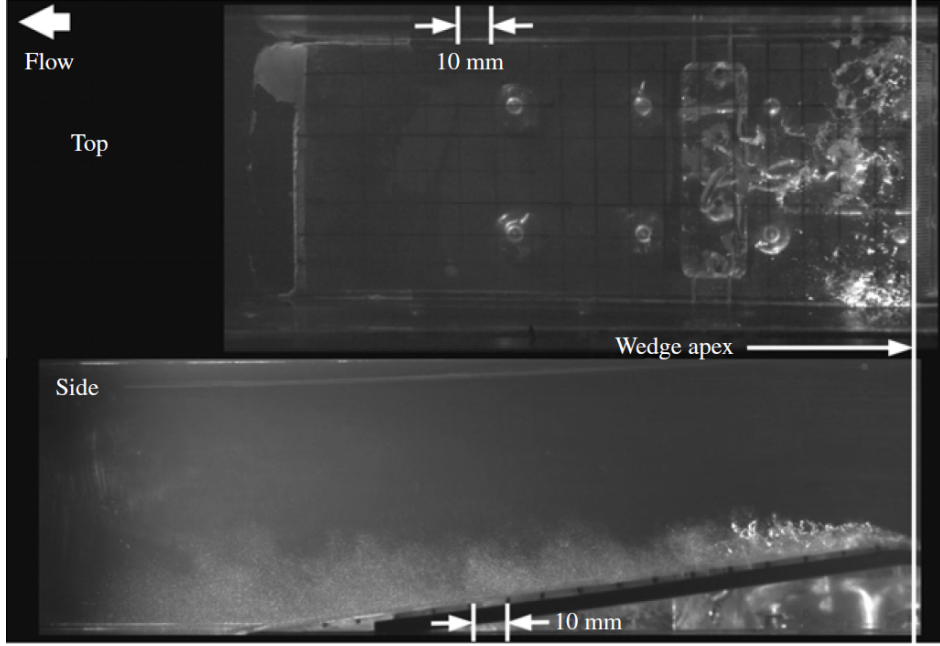


Figure 1.1: Cavity formation in high-speed video snapshot of an incipient cavity forming on the wedge ([Ganesh et al., 2016](#)).

volume, creates regions of high pressure and temperature, and emits radially propagating shock waves ([Rayleigh, 1917](#); [Flannigan et al., 2006](#); [Lauterborn & Kurz, 2010](#)). Sonoluminescence, a phenomenon in which cavitation bubbles radiate visible light due to extreme temperatures (i.e., up to several thousands of degrees Kelvin at collapse), is another major event observed in numerous experiments ([Barber & Putterman, 1991](#); [Brenner et al., 2002](#); [Lohse, 2005](#); [Flannigan & Suslick, 2010](#); [Duplat & Villermaux, 2015](#)). Figure 1.2 shows the shock propagation, and light emission from the spherical collapse of an isolated vapor bubble in a free field.

It is known that high pressures and temperatures, as well as the corresponding shock waves, produced by the collapse of cavitation bubbles, are capable of damaging the nearby objects. This damage is recognized as one of the main consequences of cavitation, and is an essential research topic in a variety of hydrodynamic and acoustic/biomedical applications. Although conceptually similar, there are some differences between hydrodynamic and acoustic/biomedical cavitation, and the structural damage thereby produced. In the former, the dominant collapse is the Rayleigh collapse of a cavitation bubble, in which a vapor bubble grows from a nucleus to a large size, and then collapses inertially ([Rayleigh, 1917](#); [Vogel et al., 1989](#); [Philipp & Lauterborn, 1998](#)). Al-

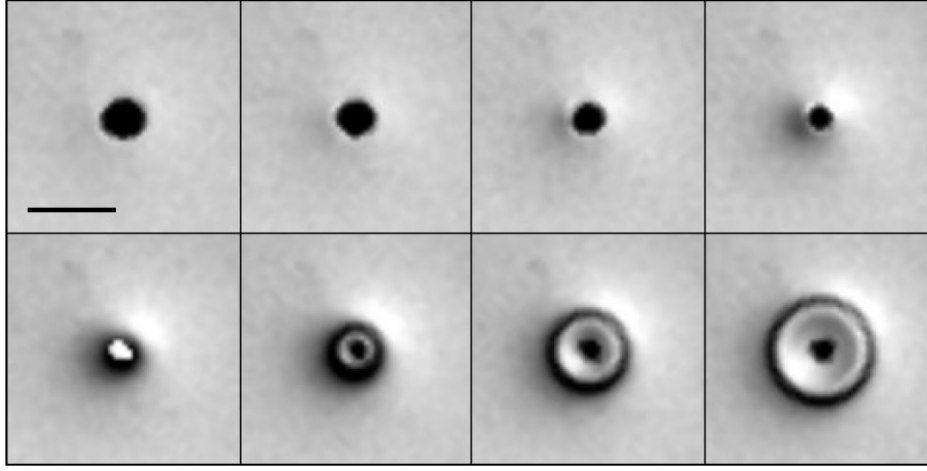


Figure 1.2: Shock propagation and light emission captured by high-speed shadowgraph visualization of the spherical collapse of a vapor bubble ([Supponen et al., 2017](#)).

though such a collapse may occur in the latter, shock-induced collapse also plays an important role because of the high-amplitude incoming pulses that collapse the bubbles ([Xi & Zhong, 2001](#); [Pishchalinikov et al., 2003](#)). In acoustic/biomedical cavitation, the bubbles are typically smaller, such that the pressure impulses, though of similar amplitude, have shorter time scales and are exerted over smaller areas. The materials under consideration in hydrodynamic-cavitation erosion are primarily ductile, as opposed to brittle or even soft (e.g., tissue) in certain biomedical applications such that damage mechanisms may be different.

The destructive nature of cavitation erosion is a significant challenge in naval hydrodynamics; engineers still struggle to cope with the deleterious effects of cavitation erosion on lifting surfaces, turbine blades, propellers, and rudders ([Arndt, 1981](#); [Escaler et al., 2006](#)), as illustrated in Figure 1.3a. In the context of combustion, cavitation may occur in nozzles of Diesel injectors, particularly under high back-pressure conditions. This happens due to the reduction in fuel pressure when the flow from injectors enters the nozzle discharge holes. Thus, Diesel nozzles, which operate at pressures up to 2000 bars, are known to be susceptible to cavitation erosion and fatigue ([Chaves et al., 1995](#); [Gavaises et al., 2007](#); [Giannakis et al., 2008](#)). In recent years, scientists in Spallation Neutron Source (SNS) at Oak Ridge National Laboratory (ORNL) have observed cavitation erosion in their target vessels where liquid mercury flows, shown in Figure 1.3b. At the SNS,

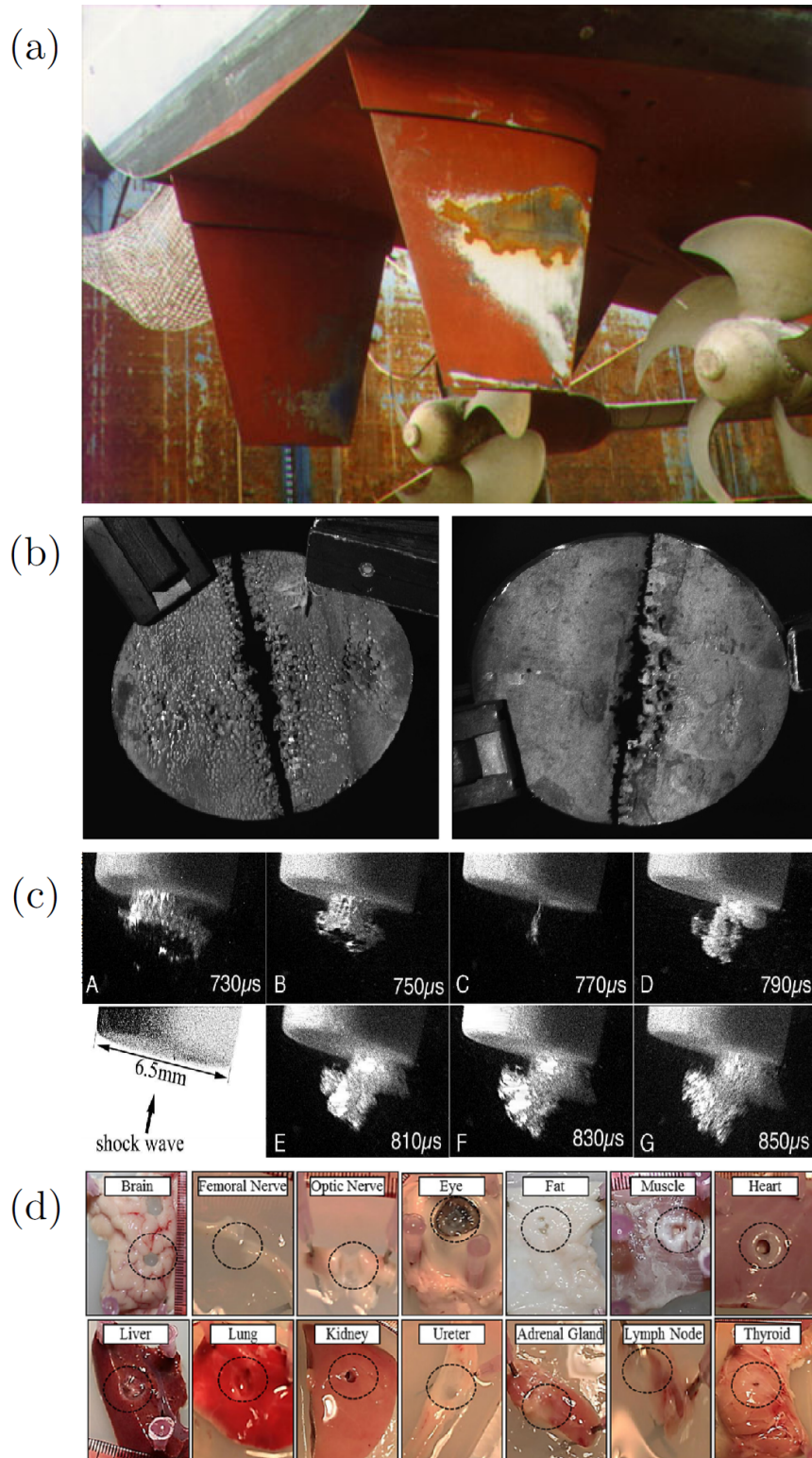


Figure 1.3: Cavitation-induced damage in different applications; (a): erosion on the rudder of a full-scale naval combatant. (Courtesy: U.S. Naval Surface Warfare Center, Carderock Division); (b): erosion on target vessel in SNS ([McClintock et al., 2012](#)); (c): damage to artificial kidney stone ([Pishchalnikov et al., 2003](#)); (d): histotripsy tissue erosion ([Vlaisavljevich et al., 2014](#))

short (microsecond) proton pulses are employed to hit a mercury target and produce neutrons, a process called spallation. Then, the highly intense pulsed neutron beams are used to investigate and understand materials at the atomic level. When the proton beam hits the mercury target, it dramatically increases the temperature and thus generates strong pressure waves (20-30 MPa, depending on the proton beam power), which further leads to the formation of small-scale cavities in mercury. During the operation of the SNS, the inertial collapse of such cavitation bubbles can induce severe damage on the interior surfaces of the target vessel, which is a significant life-limiting factor of SNS target vessels (McClintock *et al.*, 2012; Riemer *et al.*, 2014).

On the other hand, if controlled, this damage can be exploited for therapeutic purposes in biomedical applications. In the context of therapeutic ultrasound, the pressure pulses from the collapse of cavitation bubbles are employed to fragment kidney stones, a treatment called shock-wave lithotripsy (Coleman *et al.*, 1987), illustrated in Figure 1.3c. In a similar framework, histotripsy, another extracorporeal ultrasound technique, utilizes cavitation-induced erosion to produce fractionation of tissue structure in a non-thermal fashion (Maxwell *et al.*, 2009; Hempel *et al.*, 2011), as shown in Figure 1.3d. High intensity focused ultrasound (HIFU) is another example of recent medical technologies in cancer therapy that takes advantage of cavitation damage mechanisms to heat cancerous tissues and produce thermal destruction (Yu *et al.*, 2004).

1.2 Cavitation erosion

Cavitation erosion is a multiphysics and multiscale problem at the intersection of fluid and solid mechanics. The interactions of many bubbles with turbulence, the compressibility of the multiphase mixture and the shock waves produced by bubble collapse are challenging nonlinear and multiscale phenomena in fluid dynamics.

Owing to its wide range of applications, cavitation erosion has been the topic of numerous studies in the past decades. Historically, phenomenological and empirical approaches have been relied upon to predict cavitation erosion (Franc & Michel, 2006); these approaches are typically

tailored to a given application. To develop such models, pitting tests, in which the material itself serves as a sensor of cavitation-induced impact (Knapp, 1955), are usually performed on a model to quantify the aggressiveness of the cavitation (Kim *et al.*, 2014). Then, vibratory devices are typically used to classify the materials according to their resistance to erosion (Preece, 1979) in an accelerated fashion in the laboratory, in which significant mass loss can be obtained in a reasonable exposure time, thus making it possible to explore the advanced stages of erosion (Franc *et al.*, 2011). Finally, the erosion data are correlated from the model to the prototype using appropriate scaling laws. However, such a procedure clearly lacks universality: the classification of materials based on their resistance to erosion depends on the device and operating conditions, and the scaling laws are usually unknown. Thus, given a new design and novel materials, it is generally impossible to predict the onset and aggressiveness of erosion.

The modern description of cavitation erosion to metallic surfaces is based on a sequence of four steps (Franc *et al.*, 2011): production of small-scale vapor structures, impact loads due to bubble collapse defined by a cavitation intensity, pitting (incubation or plastic deformation of the material), and failure evidenced by mass loss. Based on this description, the most advanced model to date was developed for prediction of pitting and mass loss based on the idea of cavitation intensity (Franc *et al.*, 2011). The foundations of this model lie in an accurate characterization of impact loads. In other words, for such a model to function, the (normal and shear) stresses exerted by the hydrodynamics, i.e., bubble dynamics, must be communicated to the solid mechanics model. Although certain experimental (Tomita & Shima, 1986) and computational (Johnsen & Colonius, 2009) studies with quantitative measurements exist, the resolution and fidelity of such data remain lacking. In addition, the exact mechanism by which these loads are produced (e.g., shock emitted upon collapse, microjet impact, coherent cloud collapse, cavitating vortices, Franc & Michel (2006)) is unknown. Further studies of the bubble dynamics and collapse therefore constitute an absolute necessity in order to advance the understanding in this field.

Recent experiments (Deplancke *et al.*, 2015; Hattori *et al.*, 2015) suggest that unlike metallic objects, certain soft materials and polymeric coatings like Ultra High Molecular Weight Polyethy-

lene (UHMWPE) may fail in a different manner. In particular, damage characteristics of local heating and melting are observed for UHMWPE subjected to a cavitating flow, despite the excellent wear resistance of such materials. [Deplancke *et al.* \(2015\)](#) argue that in the case of polymers whose melting temperature is relatively low, thermal effects may play a major role in inducing cavitation erosion. However, due to the wide range of spatial and temporal scales, as well as the limitations of temperature-measuring devices, precise experimental measurements of the local and instantaneous temperatures are extremely challenging. Thus, numerical modeling has the potential to provide a connection between cavitation and heat-induced erosion, such that the damage mechanisms can be determined.

1.3 Bubble dynamics

Given that the key unknown in the most sophisticated model for cavitation erosion is the impact load produced by collapsing bubbles, we discuss the dynamics of bubble clouds and individual bubbles.

1.3.1 Collapse of bubble clouds

In the vast majority of cavitation applications, large numbers of bubbles are present and interact with each other hydrodynamically and acoustically. The generation of bubble clouds may be the response to a periodic disturbance imposed on the flow or may occur as a result of the shedding of bubble-filled vortices ([Arndt, 2002](#)). The dynamics of bubble clouds have received much attention in the linear regime, assuming that perturbations of the bubbles from equilibrium are small ([Brennen, 1995](#)). However, nonlinear effects are expected to strongly affect the dynamics and acoustics. For instance, [Hansson *et al.* \(1982\)](#) showed that the coherent collapse of a bubble cloud leads to the formation of a an inward-propagating shock that focuses at the center of the cloud and magnifies the noise and damage potential. In another study, [Reisman *et al.* \(1998\)](#) observed other local events that lead to high pressures generated along neighboring surfaces. At the present

time, the computational costs of direct numerical simulation of the Navier-Stokes equations for clouds of bubbles over repeated oscillations are prohibitive (Seo *et al.*, 2010). Instead, a continuum approach is usually followed, in which volume- or ensemble-averaged equations are solved to simulate the cloud, and the relevant flow properties, such as mixture density, are defined based on the local void fraction of the gas (Van Wijngaarden, 1968; Zhang & Prosperetti, 1994; Fuster & Colonius, 2011). Such models are typically based on spherical bubble dynamics in incompressible and inviscid liquids, i.e., the Rayleigh-Plesset equation. Arguably one of the most accurate models is that of Fuster & Colonius (2011), which accounts for compressibility effects of the liquid and acoustic interactions between bubbles.

However, in none of these models are non-spherical bubble dynamics, which will be discussed in greater detail in section 1.3.2, or merging/fission included. In an attempt to understand bubble-bubble interactions, Tiwari *et al.* (2015) conducted direct simulations of the collapse of 50 bubbles and showed that the collapse propagates inward and the re-entrant jets are directed towards the interior of the cloud. They further showed that peak pressures nearly ten time smaller than those predicted by different cloud models are measured on the wall. In another numerical study, Schmidt *et al.* (2014) simulated the collapse of a bubble cluster including 125 spherical vapor bubbles near a rigid wall, and compared the results to the collapse of a locally homogeneous two-phase mixture under the same condition. They concluded that although the simulation of the homogeneous mixture collapse predicts a maximum wall pressure two orders of magnitude lower than the highly resolved case, the overall collapse intensity and its duration are fairly obtained.

1.3.2 Single-bubble dynamics

The problem at the center of cavitation erosion, as well as cloud collapse, is the collapse of a single bubble. Rayleigh (1917) conducted the first detailed investigations spherical collapse of cavitation bubbles; this research forms the basis of cavitation studies. The well-known Rayleigh-Plesset

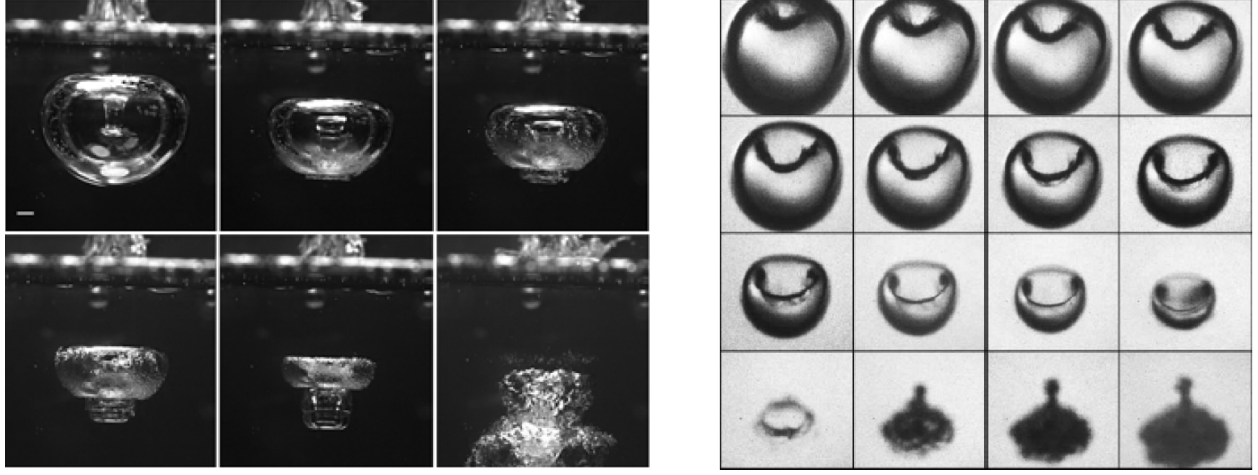


Figure 1.4: Liquid jet formation penetrating the collapsing bubbles; left: collapse near a free surface ([Supponen et al., 2016](#)); right: collapse near a rigid boundary ([Lindau & Lauterborn, 2003](#)).

equation has been widely used to describe the dynamics of a spherical collapse:

$$\rho_l \left(\ddot{R}R + \frac{3}{2}\dot{R}^2 \right) = p_v - p_\infty + p_{G_o} \left(\frac{R_o}{R} \right)^{3\gamma}, \quad (1.1)$$

where ρ_l is the liquid density, $R(t)$ is the bubble radius, p_v is the vapor pressure, p_∞ is the pressure at infinity, γ is the polytropic constant and p_{G_o} is the initial partial pressure of the gas. Thereafter, many improvements, such as viscosity and surface tension, liquid compressibility, and thermal effects were introduced into Rayleigh's theory ([Plesset, 1949](#); [Gilmore, 1952](#); [Plesset & Zwick, 1954](#); [Hickling, 1963](#); [Plesset & Prosperetti, 1977](#)). Damage produced by cavitation bubbles was initially thought to be caused by the shock waves, and high pressure regions produced at collapse ([Hickling & Plesset, 1964](#); [Fujikawa & Akamatsu, 1980](#)).

However, in the vicinity of a neighboring boundary, bubble collapse becomes asymmetric, as evidenced by the formation of a re-entrant jet of liquid penetrating the bubble ([Naudé & Ellis, 1961](#); [Benjamin & Ellis, 1966](#); [Plesset & Chapman, 1971](#)). High-speed photography reveals that the re-entrant jet accelerates towards a rigid object, while a free surface drives the jet away from the boundary ([Lindau & Lauterborn, 2003](#); [Supponen et al., 2016](#)), as illustrated in Figure 1.4. Although this asymmetry hinders energy concentration, the impact of the re-entrant jet upon the

distal side of the bubble or directly onto the neighboring solid generates a water-hammer shock, thus producing high pressures (Tomita & Shima, 1986). Therefore, a second damage mechanism, the water-hammer pressure due to the jet impact, was proposed in a theoretical study by Kornfeld & Suvorov (1944), and later confirmed in numerous other studies, both experimental and analytical (Naudé & Ellis, 1961; Benjamin & Ellis, 1966; Plesset & Chapman, 1971).

Early on, a spark discharge method was being used to study cavitation bubble dynamics experimentally (Naudé & Ellis, 1961; Benjamin & Ellis, 1966; Tomita & Shima, 1986). However, one major difficulty of this technique is the interference of electrodes with the flow field. Lauterborn & Bolle (1975) used a laser to vaporize water, and create a bubble. Although it is debatable whether optically produced cavitation behaves in a fashion similar to hydrodynamically or acoustically generated bubbles, this technique, combined with high-speed photography, has enabled more accurate experiments, leading to a better understanding of non-spherical bubble dynamics (Vogel *et al.*, 1989; Philipp & Lauterborn, 1998; Lindau & Lauterborn, 2003; Supponen *et al.*, 2016).

1.3.3 Numerical simulations

The combination of compressibility effects of high-impedance fluids (e.g., liquids), propagation of shock/rarefaction waves in a multiphase medium, and their interactions with material interfaces and nearby solid boundaries results in a complex multiscale and multphysics problem. Diagnosing these flows experimentally is particularly challenging, e.g., due to the wide range of spatial and temporal scales, difficult optical access, and intrusiveness of measurement devices; thus, highly resolved numerical simulations have become beneficial complements to experimental studies.

From the numerical standpoint, there exist several models to describe the different phases in the simulation of cavitating flows. One is based on the assumption that the vapor and water form a homogeneous mixture. In this approach, the water or vapor phase is determined by computing the density of the fluid at a given grid point; appropriate equations of state for the vapor (ideal gas) and the liquid water (modified Tait equation) are then applied (Saurel *et al.*, 1999). This approach has been used to study various large-scale cavitating flows (Saurel *et al.*, 1999; Schnerr *et al.*, 2008), in

which large numbers of bubbles were present. This model has been validated against experimental data at saturated conditions. Another approach is to treat each fluid component separately, while using a single equation of state describing the different fluids, e.g., the Nobel-Abel Stiffened-Gas equation of state (Le Métayer & Saurel, 2016). This model has been validated against another set of experimental data for shocks in water and at saturated conditions. The different fluid components are defined based on the values of the constant(s) that enter the equation. This approach has been used to simulate cavitating flows (Paillere *et al.*, 2003; Le Métayer *et al.*, 2005). If following this approach, special care must be taken to prevent the generation of spurious pressure and temperature oscillations across interfaces (Shyue, 1998; Johnsen & Colonius, 2006; Johnsen & Ham, 2012; Beig & Johnsen, 2015a).

However, performing accurate simulations of cavitation-bubble dynamics is also challenging, owing to algorithmic difficulties. Early studies relied on an incompressible framework, e.g., Particle In Cell, incompressible Boundary Integral, and incompressible Boundary Element, which relied on potential flow theory to predict the bubble deformation and jet formation at early stages of the collapse (Plesset & Chapman, 1971; Blake *et al.*, 1986; Robinson *et al.*, 2001; Klaseboer *et al.*, 2005; Supponen *et al.*, 2016). With these methods, it is difficult to handle the topology change after the jet impact, as well as capturing the shocks and rarefactions when compressibility effects become important, and thus cannot be used to accurately solve for the flow physics during the collapse. Several other approaches have been used to simulate such flows by solving the compressible Euler equations. However, the main difficulty is to resolve the shock waves and interfaces in a robust and stable fashion. Ball *et al.* (2000) implemented a two-dimensional second-order accurate Free-Lagrange Method to simulate the shock-induced collapse of an air cavity in water; Turangan *et al.* (2008) extended this approach to the axisymmetric collapse of an air bubble in water. However, difficulties with remeshing such complex phenomena limit the usability of this approach in three-dimensional simulations. Hu *et al.* (2006) employed a level-set approach with corrections for conservation losses to simulate the two-dimensional shock-induced collapse, while Lauer *et al.* (2012) extended this approach to three dimensions, and simulated the Rayleigh

collapse of a vapor bubble near a rigid wall. However, the modifications to resolve conservation issues near interfaces are computationally expensive and not practical for high-resolution three-dimensional simulations. Sussman (2003) developed a coupled level-set/volume-of-fluid approach to simulate the growth and collapse of vapor bubbles, and Hawker & Ventikos (2012) used a front-tracking method to simulate the shock-induced collapse of a cylindrical air bubble based on the experiments of Bourne & Field (1992). The main drawback of these approaches is potential violation of conservation laws. Recently, high-order accurate shock- and interface-capturing methods have been employed to perform simulations of collapsing cavitation bubbles (Johnsen & Colonius, 2009; Tiwari *et al.*, 2015; Beig & Johnsen, 2015a). This approach is conservative, and easily applicable to three dimensions.

1.4 Thesis overview

The objective of this thesis is to use high-resolution numerical simulations to better understand the collapse of individual vapor bubbles near rigid boundaries, and predict the pressures and temperatures produced by the collapse. This knowledge will paint a clearer picture of the detailed physics of such complex phenomena, elucidate the damage mechanisms, and potentially mitigate erosion.

The main contributions to the field of numerical simulations of cavitation, and bubble dynamics can be categorized as:

- A novel numerical algorithm, which is capable of solving the three-dimensional compressible Navier-Stokes equations for a multiphase system accurately and efficiently, is developed (Chapter 2). This approach that prevents spurious pressure and temperature oscillations across the material interfaces, benefits from a solution-adaptive high-order accurate central difference/ discontinuity-capturing approach, and can be used to perform precise simulations of compressible multiphase flows. Verification and validation for a variety of problems are demonstrated.
- The detailed dynamics of Rayleigh collapse of a single vapor bubble near a rigid wall is pre-

sented. The bubble configuration is systematically varied to study the collapse morphology, from perfectly spherical to highly non-spherical, for different values of pressure driving the collapse. The re-entrant liquid jet formation is explained, the non-sphericity of the collapse is quantified, and energy concentration and collapse intensity based on the non-sphericity parameter are discussed. The directionality of radially propagating shock waves from the collapse is studied, and the subsequent pressure loads along the wall are determined. We specifically show that the non-spherical behavior of the bubble, which is expected to be only a function of bubble proximity to the boundary, plays a key role in the collapse dynamics by hindering the energy concentration; the higher the collapse non-sphericity, the lower the collapse intensity. Accordingly, we explain that the bubbles initially located close to the wall collapse in a more asymmetric fashion, thus producing less energetic shocks and, subsequently, lower pressures. However, because of their high proximity to the wall, these bubbles are likely to be the most destructive. We further provide scaling for important collapse parameters (e.g., jet velocity, pressure distribution along the emitted shock, and pressure loads along the wall) that can be used to estimate the behavior of single bubble collapse (Chapter 4).

- The temperatures produced in the fluid and solid are measured for the collapse of a bubble near a rigid surface, and the responsible mechanisms for the elevated temperatures along the wall are identified. We show that, depending on the initial stand-off distance of the bubble from the wall, these high temperatures are caused by either the collapsing bubble coming in contact with the wall or the shock wave from the collapse. A scaling is developed to describe the maximum fluid temperature along the wall as a function of the geometrical configuration and collapse driving pressure. To predict the temperature of the solid, a semi-analytical heat transfer model is developed. We further show that, for certain soft materials, instantaneous temperatures greater than the melting point are produced on the solid surface during the bubble collapse (Chapter 5).

- Inertial collapse of a bubble pair near a rigid surface is simulated for a wide range of geometrical configurations. The interactions between the collapsing bubbles, and their effects on the overall dynamics, jet formation, emitted shock waves, and pressures thereby produced by the collapse of the bubble pair are investigated. It is shown that the bubble-bubble interactions substantially raise the collapse non-sphericity and, depending on the initial bubbles' arrangement, may increase or decrease the the pressure loads along the wall. (Chapter 6).

Accordingly, the current thesis is organized as follows. Part I: Chapter 2 presents a novel numerical framework for multiphase flow. Part II: Chapter 3 defines the implemented physical/numerical modeling to perform the relevant simulations for the bubble dynamics study. Chapter 4 discusses the non-spherical collapse of a single bubble near a rigid wall. Extensive validations for the presented simulations against experimental data are provided in this chapter. Temperature and its potential role in cavitation erosion is explained in Chapter 5. The effects of bubble-bubble interactions on collapse dynamics are investigated in Chapter 6. Finally, Chapter 7 provides concluding remarks and potential further work for the current research topic.

Part I:

A numerical model for multiphase flows

CHAPTER 2

Maintaining interface equilibrium conditions in compressible multiphase flows using interface capturing

This chapter is adapted from Beig & Johnsen (2015a).

2.1 Abstract

An accurate treatment of material interfaces in compressible multiphase flows poses important challenges for high-resolution numerical methods. Although high-order interface-capturing schemes have been used to accurately simulate gas/liquid interfaces with the Euler equations, these methods can result in temperature spikes at material discontinuities. While this phenomenon is not problematic for Euler simulations, it gives rise to numerical errors when heat conduction is included. In this chapter, we identify the source of these errors and propose a methodology to prevent their occurrence for various models used to represent gas/liquid interfaces in compressible flows based on a “single-fluid” formulation, in which interfaces are represented by discontinuities in the material properties. Our focus lies in materials (gases and liquids primarily, but also solids) that can be described by a stiffened equation of state, though our approach is generalizable to other relations. We show that numerical approaches that prevent pressure oscillations at interfaces may generate temperature errors, which affect the energy (and pressure) through the heat conduction term. We

demonstrate that the material properties entering the equation of state must be computed according to suitable transport equations in conservative or non-conservative forms; the pressure and temperature must be calculated based on the appropriate properties. To verify the analysis and compute problems with gas/liquid interfaces of relevance, we develop a three-dimensional, high-order accurate, solution-adaptive finite difference framework. In particular, we show that temperatures and pressures may be significantly overestimated in calculations of shock-induced bubble collapse in water if temperature errors are not prevented.

2.2 Introduction

Compressible multiphase flows are central to a number of engineering applications, including cavitation erosion and high-speed combustion. One of the main challenges in accurately simulating these flows lies in simultaneously representing shock waves, interfaces separating fluids of large density ratios and physical diffusion processes, due to spurious numerical errors commonly generated at interfaces, which may eventually affect the entire flow field. The present work focuses on developing Eulerian approaches to accurately simulate shock waves and gas/liquid interfaces, with viscous and heat diffusion included.

Numerical methods for Eulerian simulations of compressible flows with interfaces typically fall in one of two categories, tracking or capturing. In this article, we focus on the latter because it is relatively simple to implement even for high-order methods and is a logical approach to treat physical diffusion; tracking, which includes front-tracking (Glimm *et al.*, 1998) and level-set (Osher & Sethian, 1988) methods, will not be discussed further here. Similarly to shock capturing, interfaces between fluids of different composition can be captured by regularizing them over a few grid points, while maintaining the correct jump conditions. By adding one transport equation for mass conservation of one of the fluids, an extension of the Euler equations to multiple fluids/phases is seemingly straightforward, as such an equation can be solved in conservative form with standard shock-capturing techniques. However, such a naive implementation has long been

known to give rise to spurious pressure oscillations for isolated interfaces between fluids of different material properties (i.e., properties entering the equation of state) (Abgrall, 1996; Shyue, 1998). Furthermore, since material interfaces are linearly degenerate, there is no physical mechanism to steepen interfaces, unlike shock waves. Thus, to prevent interfaces from being overly smeared by numerical diffusion, high-order solution-adaptive (Movahed & Johnsen, 2013; Henry de Frahan *et al.*, 2015) or sharpening (Kokh & Lagoutiere, 2010; Shyue & Xiao, 2014; Tiwari *et al.*, 2013) techniques are often used in practice.

In this context, Abgrall (1996) was the first to recognize that, for interfaces separating two gases of different specific heats ratios γ , an additional transport equation solved for a distinct function of γ in non-conservative (advection) form prevents such oscillations. Shyue (1998) later expanded this idea to solving a transport equation for the mass fraction, again in non-conservative form, and to liquids and solids obeying a stiffened equation of state. Johnsen & Colonius (2006) further extended these approaches to high-order Weighted Essentially Non-Oscillatory (WENO, Shu, 1998) methods to simulate non-spherical bubble collapse (Johnsen & Colonius, 2009), which (Coralic & Colonius, 2014) further refined. Such high-order finite volume methods can be computationally expensive in multiple dimensions. To address this difficulty, finite difference (for gases only, Movahed & Johnsen, 2013; Kawai & Terashima, 2011; Terashima *et al.*, 2013) and discontinuous Galerkin (Henry de Frahan *et al.*, 2015) methods have been proposed, in which high-order limiting is applied only at discontinuities. In simulations of the compressible Navier-Stokes equations for two gases with different specific heats ratios, Johnsen & Ham (2012) noticed that an inconsistent treatment of temperature causes similar errors and significant temperature undershoots due to the coupling via the heat diffusion term; they proposed approaches to overcome these problems based on γ or mass fraction formulations. Although temperature errors may occur in Euler simulations, they have no influence on the results since temperature is a derived quantity. However, such temperature errors are problematic when accounting for heat diffusion, reacting flows, phase change and other temperature-dependent phenomena.

Recent developments in interface capturing for compressible multiphase flows originated from

the seven-equations two-phase flow model (Baer & Nunziato, 1986), in which balance equations for mass, momentum and energy of each phase, as well as an equation for volume fraction evolution, are solved. The additional volume fraction equation prevents the occurrence of spurious pressure oscillations. For many problems of practical importance, five-equations models (e.g., that in Kapila *et al.*, 2001) describe the physics accurately, in which pressure and velocity equilibria between the phases are assumed; thus, equations for mass balance of each phase, for total momentum and energy, and for the volume fraction evolution are solved. This latter model and extensions thereof have been used to study a wide range of phenomena (Allaire *et al.*, 2002; Saurel & Abgrall, 1999a; Perigaud & Saurel, 2005; Kreeft & Koren, 2010; Kapila *et al.*, 2001; Murrone & Guillard, 2005; Petitpas *et al.*, 2009; Flåtten *et al.*, 2010; Braconnier & Nkonga, 2009). With these models, a consistent and efficient high-order extension to accurately include heat diffusion and predict temperature has yet to be proposed.

The objective of the present work is to develop a treatment for temperature in compressible multiphase flows that is physically consistent and efficient, and that does not produce spurious errors in simulations of gas/liquid interfaces and shocks, with viscous and heat diffusion included. Our approach is general in that it applies to γ (as in Abgrall, 1996), mass fraction (as in Shyue, 1998) and volume fraction (e.g., five-equations, Kapila *et al.*, 2001) models. Through our analysis, we identify the causes for numerical errors caused by an inconsistent treatment of temperature using high-order shock-capturing schemes and show how these errors can be prevented so that accurate simulations with physical diffusion can be performed. The resulting 3D finite difference scheme is high-order accurate, conservative and prevents pressure and temperature errors. Our contribution advances the current understanding of compressible multiphase flows in that it generalizes the methodology of Johnsen & Ham (2012) for gases, in which temperature errors are prevented, to gas/liquid flows and different capturing approaches and extends the work of Coralic & Colonius (2014) to prevent temperature errors in such flows.

2.3 Physical model

2.3.1 Equations of motion

Assuming no mass transfer or surface tension, the compressible Navier-Stokes equations govern the gas/liquid flows of interest:

$$\frac{\partial \rho}{\partial t} + \frac{\partial}{\partial x_j}(\rho u_j) = 0, \quad (2.1a)$$

$$\frac{\partial \rho u_i}{\partial t} + \frac{\partial}{\partial x_j}(\rho u_i u_j + p \delta_{ij}) = \frac{\partial \tau_{ij}}{\partial x_j}, \quad (2.1b)$$

$$\frac{\partial E}{\partial t} + \frac{\partial}{\partial x_j}[u_j(E + p)] = \frac{\partial}{\partial x_j}(u_i \tau_{ij} - Q_j), \quad (2.1c)$$

where ρ is the density, u_i the velocity vector, p the pressure, $E = \rho e + \rho u_i u_i / 2$ the total energy, e the internal energy and δ_{ij} the identity tensor. The viscous stress tensor τ_{ij} and heat flux Q_j are given by:

$$\tau_{ij} = \mu \left(\frac{\partial u_i}{\partial x_j} + \frac{\partial u_j}{\partial x_i} - \frac{2}{3} \frac{\partial u_k}{\partial x_k} \delta_{ij} \right) + \mu_B \frac{\partial u_k}{\partial x_k} \delta_{ij}, \quad Q_j = -\kappa \frac{\partial T}{\partial x_j}, \quad (2.2)$$

where μ is the dynamic shear viscosity, μ_B the bulk viscosity and κ the heat conductivity.

2.3.2 Equation of state

A relation between pressure, temperature and internal energy valid for gases and liquids is required. Although homogeneous equilibrium and tabular relationships have been used for cavitating flows (Schnerr *et al.*, 2008; Kim *et al.*, 2014), the stiffened equation of state introduced by Le Métayer *et al.* (2005) is a simple and sufficiently accurate model, which has been validated against experiments for shock propagation in water and certain solids, and has been used to simulate cavitating flows (Saurel *et al.*, 2008; Goncalvès & Patella, 2010). The relationships between pressure, tem-

Coefficients	Air	Water
n	1.4	2.35
$B (MPa)$	0	1000
$c (J/kgK)$	718	1816
$q (J/kg)$	0×10^6	-1.167×10^6

Table 2.1: Relevant constants for the stiffened equation of state.

perature and internal energy are given by:

$$\rho(e - q) = \frac{p}{n - 1} + \frac{nB}{n - 1}, \quad (\text{pressure-wise}) \quad (2.3a)$$

$$= \rho cT + B, \quad (\text{temperature-wise}) \quad (2.3b)$$

where n , B , q , and c are material properties fit to experimental data. For air and water, the relevant constants take the values shown in Table (2.1). In the limit of ideal gases, $n = \gamma$ represents the specific heat ratio, $c = c_v$ is the specific heat at constant volume, and B and q are zero, such that the ideal gas law is recovered. For multiphase flows, we follow a “single-fluid” formulation, in which the same thermodynamic relationship holds in the entire domain, with material interfaces denoted by changes in the material properties, which are advected by the flow.

2.3.3 Multifluid modeling

2.3.3.1 Definitions and basic relations

The volume fraction $\alpha^{(k)}$ is the volume of fluid k divided by the total mixture volume in a control volume, and the mass fraction $z^{(k)}$ represents the mass of fluid k divided by the mass of the mixture in the control volume, with $\sum_k \alpha^{(k)} = 1$ and $\sum_k z^{(k)} = 1$. Accordingly, the mixture density ρ is defined:

$$\rho = \sum_k \rho^{(k)} \alpha^{(k)} = \sum_k \rho z^{(k)}, \quad (2.4)$$

where the superscripts (k) denote phase/fluid k . Similarly, the internal energy of the mixture per unit mass e is:

$$e = \sum_k z^{(k)} e^{(k)}, \quad \text{and} \quad \rho e = \sum_k \rho^{(k)} \alpha^{(k)} e^{(k)}. \quad (2.5)$$

The mass fraction and volume fraction are related by:

$$z^{(k)} = \rho^{(k)} \alpha^{(k)} / \rho, \quad \text{with} \quad \frac{1}{\rho} = \sum_k \frac{z^{(k)}}{\rho^{(k)}}. \quad (2.6)$$

For ideal gases, with γ equivalent to n , the following relationship further holds:

$$\left(\frac{1}{\gamma - 1}\right) \frac{1}{M} = \sum_k z^{(k)} \left(\frac{1}{\gamma^{(k)} - 1}\right) \frac{1}{M^{(k)}}. \quad (2.7)$$

In the above relationships, $z^{(k)}$, $\alpha^{(k)}$, $\rho^{(k)}$ and $e^{(k)}$ may vary in space and time, but $\gamma^{(k)}$ and $M^{(k)}$ do not.

2.3.3.2 Mixture relations

Although we focus on gas/liquid interfaces that are initially sharp, capturing regularizes these interfaces over a few grid points, so that mixture regions exist. For the transport coefficients, we use the mixture relations of Perigaud & Saurel (2005): $\mu = \sum_k \alpha^{(k)} \mu^{(k)}$ and $\kappa = \sum_k \alpha^{(k)} \kappa^{(k)}$. For the thermodynamic quantities, we seek to express the material properties that enter the equation of state in an appropriate form for mixtures. Substituting the pressure-based relation stiffened equation (2.3a) into Eq. (2.5) yields:

$$\frac{p}{(n-1)} + \frac{nB}{(n-1)} + \rho q = \sum_k \alpha^{(k)} \frac{p^{(k)}}{(n^{(k)}-1)} + \sum_k \alpha^{(k)} \frac{n^{(k)} B^{(k)}}{(n^{(k)}-1)} + \sum_k \alpha^{(k)} \rho^{(k)} q^{(k)}, \quad (2.8)$$

while substituting the temperature-based stiffened equation (2.3b) into Eq. (2.5) yields:

$$\rho c T + B + \rho q = \sum_k \alpha^{(k)} \rho^{(k)} c^{(k)} T^{(k)} + \sum_k \alpha^{(k)} B^{(k)} + \sum_k \alpha^{(k)} \rho^{(k)} q^{(k)}. \quad (2.9)$$

Assuming isobaric ($p^{(k)} = p$) and isothermal ($T^{(k)} = T$) closure between the phases (Allaire *et al.*, 2002), it follows that

$$\begin{aligned}\frac{1}{n-1} &= \sum_k \alpha^{(k)} \left(\frac{1}{n^{(k)} - 1} \right), \quad \frac{nB}{n-1} = \sum_k \alpha^{(k)} \left(\frac{n^{(k)} B^{(k)}}{n^{(k)} - 1} \right), \\ B &= \sum_k \alpha^{(k)} B^{(k)}, \quad \rho q = \sum_k \rho^{(k)} \alpha^{(k)} q^{(k)}, \quad \rho c = \sum_k \rho^{(k)} \alpha^{(k)} c^{(k)}.\end{aligned}\quad (2.10)$$

As a result, we can reformulate ρe in terms of volume fractions:

$$\rho e = \begin{cases} p \sum_k \alpha^{(k)} \frac{1}{n^{(k)} - 1} + \sum_k \alpha^{(k)} \frac{n^{(k)} B^{(k)}}{n^{(k)} - 1} + \sum_k \rho^{(k)} \alpha^{(k)} q^{(k)} & \text{(pressure-wise),} \\ T \sum_k \rho^{(k)} \alpha^{(k)} c^{(k)} + \sum_k \alpha^{(k)} B^{(k)} + \sum_k \rho^{(k)} \alpha^{(k)} q^{(k)} & \text{(temperature-wise).} \end{cases} \quad (2.11)$$

A similar procedure can be followed using the energy relation based on the mass fraction in Eq. (2.5). For the pressure-wise case,

$$\frac{p}{\rho(n-1)} + \frac{nB}{\rho(n-1)} + q = \sum_k z^{(k)} \frac{p^{(k)}}{\rho^{(k)}(n^{(k)} - 1)} + \sum_k z^{(k)} \frac{n^{(k)} B^{(k)}}{\rho^{(k)}(n^{(k)} - 1)} + \sum_k z^{(k)} q^{(k)}, \quad (2.12)$$

while for the temperature-wise relation:

$$cT + \frac{B}{\rho} + q = \sum_k z^{(k)} c^{(k)} T^{(k)} + \sum_k z^{(k)} \frac{B^{(k)}}{\rho^{(k)}} + \sum_k z^{(k)} q^{(k)}. \quad (2.13)$$

Likewise, Eqs. (2.12) and (2.13) can be rearranged as:

$$\begin{aligned}\left(\frac{1}{n-1} \right) \frac{1}{\rho} &= \sum_k z^{(k)} \left(\frac{1}{n^{(k)} - 1} \right) \frac{1}{\rho^{(k)}}, \quad \left(\frac{nB}{n-1} \right) \frac{1}{\rho} = \sum_k z^{(k)} \left(\frac{n^{(k)} B^{(k)}}{n^{(k)} - 1} \right) \frac{1}{\rho^{(k)}}, \\ \frac{B}{\rho} &= \sum_k z^{(k)} \frac{B^{(k)}}{\rho^{(k)}}, \quad q = \sum_k z^{(k)} q^{(k)}, \quad c = \sum_k z^{(k)} c^{(k)}.\end{aligned}\quad (2.14)$$

Thus, ρe can be written in terms of mass fractions:

$$\rho e = \begin{cases} p \sum_k \rho z^{(k)} \frac{1}{\rho^{(k)}(n^{(k)}-1)} + \sum_k \rho z^{(k)} \frac{n^{(k)}B^{(k)}}{\rho^{(k)}(n^{(k)}-1)} + \sum_k \rho z^{(k)} q^{(k)} & \text{(pressure-wise),} \\ T \sum_k \rho z^{(k)} c^{(k)} + \sum_k \rho z^{(k)} \frac{B^{(k)}}{\rho^{(k)}} + \sum_k \rho z^{(k)} q^{(k)} & \text{(temperature-wise).} \end{cases} \quad (2.15)$$

2.3.3.3 Transport equation

With the present “single-fluid” formulation, changes in composition are denoted by changes in material properties, which depend on the mass and/or volume fraction. From fundamental principles, the mass conservation equation for either of the phases, assuming no mass transfer, is:

$$\frac{\partial}{\partial t}(\rho z^{(k)}) + \frac{\partial}{\partial x_j}(\rho z^{(k)} u_j) = 0. \quad (2.16)$$

The continuity equation can be used to write this equation in advection form:

$$\frac{\partial z^{(k)}}{\partial t} + u_j \frac{\partial z^{(k)}}{\partial x_j} = 0, \quad \text{or} \quad \frac{\partial f}{\partial t} + u_j \frac{\partial f}{\partial x_j} = 0, \quad (2.17)$$

where f is any function of z .

2.4 Numerical models

Eqs. (2.1), (2.2), (2.3) and (2.16), along with an appropriate relations between the mass fraction and the material properties in the equation of state form a closed system. However, the discretization of this system may result in spurious pressure oscillations for flows with variable n if care is not taken ([Abgrall, 1996](#); [Shyue, 1998](#)). Three main interface-capturing approaches have been used to prevent such errors, by solving the transport equation in a different form, usually non-conservative:

- γ -based approach: Here, transport equations for specific functions of the material properties

entering the equation of state must be solved:

$$\frac{\partial}{\partial t} \left(\frac{1}{n-1} \right) + u_j \frac{\partial}{\partial x_j} \left(\frac{1}{n-1} \right) = 0, \quad \frac{\partial}{\partial t} \left(\frac{nB}{n-1} \right) + u_j \frac{\partial}{\partial x_j} \left(\frac{nB}{n-1} \right) = 0. \quad (2.18)$$

This approach was proposed by [Abgrall \(1996\)](#) for gases and extended to the stiffened equation of state by [Shyue \(1998\)](#). If needed, mass and/or volume fraction can be computed from the expressions in section 2.3.3.2, as long as there are only two components with different n . It requires additional transport equations for different material properties in the equation of state (e.g., [Shyue, 1999](#)).

- Volume fraction approach (five-equations model): Rather than solving transport equations for each of the material properties, Eq. (2.16) is rewritten in terms of the volume fraction (see Appendix A):

$$\frac{\partial \rho^{(k)} \alpha^{(k)}}{\partial t} + \frac{\partial}{\partial x_j} (\rho^{(k)} \alpha^{(k)} u_j) = 0, \quad (2.19a)$$

$$\frac{\partial \alpha^{(k)}}{\partial t} + u_j \frac{\partial \alpha^{(k)}}{\partial x_j} = \Gamma_{kk'} \frac{\partial u_j}{\partial x_j}, \quad \Gamma_{kk'} = \alpha^{(k)} \alpha^{(k')} \frac{\rho^{(k')}(a^{(k')})^2 - \rho^{(k)}(a^{(k)})^2}{\alpha^{(k)} \rho^{(k')}(a^{(k')})^2 + \alpha^{(k')} \rho^{(k)}(a^{(k)})^2} \quad (2.19b)$$

where $a^{(k)}$ is the sound speed in phase/fluid k . This approach written as such was introduced by [Murrone & Guillard \(2005\)](#) and is not restricted to the stiffened equation of state. Eq. (2.19b) is required to prevent pressure oscillations. For sharp-interface problems, $\Gamma_{kk'}$ is commonly set to zero ([Allaire *et al.*, 2002](#); [Perigaud & Saurel, 2005](#); [Shukla *et al.*, 2010](#)), which corresponds to the limit of infinite resolution. For the analysis presented in this chapter, we also follow this convention.

- Mass fraction approach: Eq. (2.20) is solved,

$$\frac{\partial z^{(k)}}{\partial t} + u_j \frac{\partial z^{(k)}}{\partial x_j} = 0. \quad (2.20)$$

This approach was introduced by [Shyue \(1998\)](#); an alternate form of Eq. (2.7) to relate z to

γ (for gases) in which it is implicitly assumed $M_1 = M_2$ is necessary to prevent pressure oscillations, which is not true in general. This approach is not restricted to the stiffened equation of state, and only one transport equation is needed for each extra component/phase.

Although these approaches prevent the generation of pressure errors, they do not necessarily maintain temperature equilibrium. In the case of gases for instance, [Johnsen & Ham \(2012\)](#) showed that the mass fraction approach must be modified to prevent temperature errors. This issue is not problematic for Euler simulations since temperature is a derived quantity that does not enter the equations; however, they matter for Navier-Stokes simulations, as failure to maintain temperature equilibrium generates errors in the energy (and thus pressure) through the heat conduction term, which then affect all variables. In the next section, we identify the origin of temperature errors in gas/liquid flows and discuss how to eliminate them.

2.5 Analysis of the temperature errors

2.5.1 Occurrence of temperature errors

To illustrate the occurrence of temperature errors, we consider the 1D advection of an isolated material interface between a gas and a liquid at a constant velocity, pressure, and temperature, inspired by the analysis of [Johnsen & Ham \(2012\)](#). Initially, p , u and T are constant, and ρ and the material properties entering the equation of state are discontinuous. The exact solution for this problem is that this discontinuous front propagates at speed u ; from the computational viewpoint, although the initially discontinuous profiles diffuse numerically, p , u and T are expected to remain constant (to round-off). We start with the compressible Navier-Stokes equations (2.1) and discretize them spatially using any of the three approaches in section 2.4. Since these approaches are all designed to preserve velocity and pressure equilibrium across the interface with no heat transfer, the continuity and momentum equations demonstrate that velocity equilibrium is preserved. The energy

equation simplifies to the following semi-discrete form, with the interface lying in cell j :

$$\frac{d(\rho e)}{dt} = -uD_j^a(\rho e) + D_j^d(\kappa D_j^d(T)), \quad (2.21)$$

where D_j^a and D_j^d are spatial difference operators for advection and diffusion that are assumed to have the following properties (Johnsen & Ham, 2012):

$$D_j(A + cB) = D_j(A) + cD_j(B), \quad (2.22)$$

for c constant, A and B variable; such properties are not trivial but can be enforced, even with high-order methods (Johnsen & Colonius, 2006; Coralic & Colonius, 2014). Substituting the stiffened equation of state (2.3) into Eq. (2.21) yields for the pressure (assuming ρq is treated appropriately, as described in the next section):

$$p \frac{d}{dt} \left(\frac{1}{n-1} \right)_j + \frac{d}{dt} \left(\frac{nB}{n-1} + \rho q \right)_j = -up D_j^a \left(\frac{1}{n-1} \right) - uD_j^a \left(\frac{nB}{n-1} + \rho q \right) + D_j^d(\kappa D_j^d(T)). \quad (2.23)$$

Pressure equilibrium (i.e., the pressure at the next time step remains the same across the entire domain) is maintained if (i) the difference operators obey Eq. (2.22), (ii) the material properties entering the equation of state are evolved in a consistent fashion and (iii) the pressure is computed from the appropriate quantities (Abgrall, 1996; Shyue, 1998; Johnsen & Colonius, 2006).

Similarly, for the temperature:

$$\frac{d}{dt} (\rho c T + B + \rho q)_j = -uT D_j^a(\rho c) - uD_j^a(B) - uD_j^a(\rho q) + D_j^d(\kappa D_j^d(T)). \quad (2.24)$$

Temperature equilibrium (i.e., the temperature at the next time step remains the same across the entire domain) is maintained if (i) the difference operators obey Eq. (2.22), (ii) the material properties entering the equation of state are evolved in a consistent fashion and (iii) the temperature is computed from the appropriate quantities. Following the results in the previous section, the difference

operator for diffusion must be constructed such that $D_j(c) = 0$ for c constant (e.g., see Johnsen & Ham, 2012). There are thus two main sources for temperature errors: spatial discretization (i) and numerical model (ii and iii). A failure to maintain temperature equilibrium produces energy (and thus pressure) errors via the heat diffusion term in Eq. (2.23), which then affect the continuity and momentum equations. This issue is relevant only to problems in which heat diffusion is present.

2.5.2 Eliminating temperature errors for the different approaches

The goal is to determine the form of the transport equations to be solved and the appropriate relationships between quantities of interest to maintain temperature equilibrium for this isolated interface advection problem based on the approaches described in section 2.4.

2.5.2.1 γ -based approach

The pressure-internal energy relation (2.23) can be re-written:

$$\left[\frac{d}{dt} \left(\frac{1}{n-1} p \right)_j + up D_j^a \left(\frac{1}{n-1} \right) \right] + \left[\frac{d}{dt} \left(\frac{nB}{n-1} \right)_j + uD_j^a \left(\frac{nB}{n-1} \right) \right] + \left[\frac{d}{dt} (\rho q)_j + D_j^a (\rho qu) \right] = 0. \quad (2.25)$$

Similarly, the temperature-internal energy relation (2.24) can be re-written:

$$\left[\frac{d}{dt} (\rho c T)_j + TD_j^a (\rho cu) \right] + \left[\frac{dB_j}{dt} + uD_j^a (B) \right] + \left[\frac{d}{dt} (\rho q)_j + D_j^a (\rho qu) \right] = 0. \quad (2.26)$$

Eqs. (2.25) and (2.26) hold for any material, pressure and temperature, therefore each term in brackets must be zero for the pressure and temperature equilibria to be maintained, in which case p and T can be factored out of the time derivative in Eqs. (2.25) and (2.26). Thus,

$$\frac{d}{dt} \begin{pmatrix} 1/(n-1) \\ nB/(n-1) \\ B \end{pmatrix} + uD_j^a \begin{pmatrix} 1/(n-1) \\ nB/(n-1) \\ B \end{pmatrix} = \mathbf{0}, \quad \text{and} \quad \frac{d}{dt} \begin{pmatrix} \rho q \\ \rho c \\ \rho uc \end{pmatrix} + D_j^a \begin{pmatrix} \rho uq \\ \rho uc \\ \rho uc \end{pmatrix} = \mathbf{0}. \quad (2.27)$$

Eqs. (2.27) indicate that, to maintain pressure equilibrium in time and space with the γ -based approach, the transport equations for $1/(n - 1)$ and $nB/(n - 1)$ must be solved in non-conservative form and that for q in conservative form; pressure must be computed from these specific quantities using Eq. (2.3a). To maintain temperature equilibrium, the transport equations for B must be solved in non-conservative form and those for c and q in conservative form; temperature must be computed from these specific quantities in Eq. (2.3b).

2.5.2.2 Volume fraction approach

Considering the mixture relations for volume fraction (2.11), the pressure-internal energy relation (2.23) can be re-written:

$$\left[\frac{d}{dt} \left(\sum_k \alpha^{(k)} \frac{1}{(n^{(k)} - 1)} p \right)_j + up D_j^a \left(\sum_k \alpha^{(k)} \frac{1}{(n^{(k)} - 1)} \right) \right] + \left[\frac{d}{dt} \left(\sum_k \alpha^{(k)} \frac{n^{(k)} B^{(k)}}{(n^{(k)} - 1)} \right)_j + u D_j^a \left(\sum_k \alpha^{(k)} \frac{n^{(k)} B^{(k)}}{(n^{(k)} - 1)} \right) \right] + \left[\frac{d}{dt} \left(\sum_k \rho^{(k)} \alpha^{(k)} q^{(k)} \right)_j + D_j^a \left(\sum_k \rho^{(k)} \alpha^{(k)} q^{(k)} u \right) \right] = 0. \quad (2.28)$$

Likewise, the temperature-internal energy relation (2.24) can be expressed as:

$$\left[\frac{d}{dt} \left(\sum_k \rho^{(k)} \alpha^{(k)} c^{(k)} T \right)_j + TD_j^a \left(\sum_k \rho^{(k)} \alpha^{(k)} c^{(k)} u \right) \right] + \left[\frac{d}{dt} \left(\sum_k \alpha^{(k)} B^{(k)} \right)_j + u D_j^a \left(\sum_k \alpha^{(k)} B^{(k)} \right) \right] + \left[\frac{d}{dt} \left(\sum_k \rho^{(k)} \alpha^{(k)} q^{(k)} \right)_j + D_j^a \left(\sum_k \rho^{(k)} \alpha^{(k)} q^{(k)} u \right) \right] = 0. \quad (2.29)$$

Since pressure and temperature must remain constant in time and space, arguments similar to those made in the previous section hold, so that p and T can be factored out of Eqs. (2.28) and (2.29).

Thus,

$$\begin{aligned} \frac{d}{dt} \begin{pmatrix} \sum_k \alpha^{(k)} / (n^{(k)} - 1) \\ \sum_k \alpha^{(k)} n^{(k)} B^{(k)} / (n^{(k)} - 1) \\ \sum_k \alpha^{(k)} B^{(k)} \end{pmatrix} + u D_j^a \begin{pmatrix} \sum_k \alpha^{(k)} / (n^{(k)} - 1) \\ \sum_k \alpha^{(k)} n^{(k)} B^{(k)} / (n^{(k)} - 1) \\ \sum_k \alpha^{(k)} B^{(k)} \end{pmatrix} &= \mathbf{0}, \\ \frac{d}{dt} \begin{pmatrix} \sum_k \rho^{(k)} \alpha^{(k)} q^{(k)} \\ \sum_k \rho^{(k)} \alpha^{(k)} c^{(k)} \end{pmatrix} + D_j^a \begin{pmatrix} \sum_k \rho^{(k)} \alpha^{(k)} q^{(k)} \\ \sum_k \rho^{(k)} \alpha^{(k)} c^{(k)} \end{pmatrix} &= \mathbf{0}. \end{aligned} \quad (2.30)$$

Since only mixture density, species density and volume fraction vary in time and space, Eqs.(2.30) are discretizations of the following two transport equations for volume fraction:

$$\frac{\partial(\rho^{(k)} \alpha^{(k)})}{\partial t} + \frac{\partial}{\partial x} (\rho^{(k)} \alpha^{(k)} u) = 0, \quad (2.31a)$$

$$\frac{\partial \alpha^{(k)}}{\partial t} + u \frac{\partial \alpha^{(k)}}{\partial x} = 0. \quad (2.31b)$$

Eqs. (2.31) indicate that, to maintain pressure equilibrium in time and space for the volume fraction approach, the calculation of $1/(n - 1)$ and $nB/(n - 1)$ in Eq. (2.10) must be done using volume fraction computed from the non-conservative form of the transport equation for $\alpha^{(k)}$, and that of ρq in Eq. (2.10) using the conservative form of the transport equation for $\alpha^{(k)}$. To maintain temperature equilibrium in time and space, the calculation of B in Eq. (2.10) must be done using volume fraction computed from the non-conservative form of the transport equation for $\alpha^{(k)}$, and that of ρq and ρc in Eq. (2.10) using the conservative form of the transport equation for $\alpha^{(k)}$.

We note that Eqs. (2.31) hold for the present interface advection problem only, in which the velocity is constant for all time and space. Although Eq. (2.31a) is exact, the non-conservative form of the transport equation for volume fraction is Eq. (2.19b) (Miller & Puckett, 1996); volume fraction is not simply advected, but is additionally modified by a dilatation-dependent source term that represents the mixture compressibility. This equation can be solved but may lead to numerical difficulties, e.g., positivity of the volume fraction or maintaining correct shock jump conditions (Perigaud & Saurel, 2005; Abgrall & Perrier, 2006). We note that, in the limit of sharp interface,

numerical mixture regions vanish and the right-hand-side of Eq. (2.19b) goes to zero. Past studies have indeed followed such an approach (five-equations model, Allaire *et al.*, 2002; Perigaud & Saurel, 2005; Shukla *et al.*, 2010; Shukla, 2014; Coralic & Colonius, 2014), which we do as well.

2.5.2.3 Mass fraction approach

Using the mixture relations for mass fraction (2.15), the pressure-internal energy Eq. (2.23) can be re-written:

$$\left[\frac{d}{dt} \left(\sum_k z^{(k)} \frac{\rho}{\rho^{(k)}(n^{(k)} - 1)} p \right)_j + u D_j^a \left(\sum_k z^{(k)} \frac{\rho}{\rho^{(k)}(n^{(k)} - 1)} p \right) \right] + \left[\frac{d}{dt} \left(\sum_k z^{(k)} \frac{n^{(k)} B^{(k)} \rho}{\rho^{(k)}(n^{(k)} - 1)} \right)_j + u D_j^a \left(\sum_k z^{(k)} \frac{n^{(k)} B^{(k)} \rho}{\rho^{(k)}(n^{(k)} - 1)} \right) \right] + \left[\frac{d}{dt} \left(\sum_k \rho z^{(k)} q^{(k)} \right)_j + D_j^a \left(\sum_k \rho z^{(k)} q^{(k)} u \right) \right] = 0. \quad (2.32)$$

Similarly, the temperature-internal energy relation (2.24) can be re-written:

$$\left[\frac{d}{dt} \left(\sum_k \rho z^{(k)} c^{(k)} T \right)_j + T D_j^a \left(\sum_k \rho z^{(k)} c^{(k)} u \right) \right] + \left[\frac{d}{dt} \left(\sum_k z^{(k)} \frac{B^{(k)} \rho}{\rho^{(k)}} \right)_j + u D_j^a \left(\sum_k z^{(k)} \frac{B^{(k)} \rho}{\rho^{(k)}} \right) \right] + \left[\frac{d}{dt} \left(\sum_k \rho z^{(k)} q^{(k)} \right)_j + D_j^a \left(\sum_k \rho z^{(k)} q^{(k)} u \right) \right] = 0. \quad (2.33)$$

Following the same arguments as in the previous sections, Eqs. (2.32) and (2.33) can be re-organized:

$$\begin{aligned} \frac{d}{dt} \begin{pmatrix} \sum_k \rho z^{(k)} / [\rho^{(k)}(n^{(k)} - 1)] \\ \sum_k \rho z^{(k)} n^{(k)} B^{(k)} / [\rho^{(k)}(n^{(k)} - 1)] \\ \sum_k \rho z^{(k)} B^{(k)} / \rho^{(k)} \end{pmatrix} + u D_j^a \begin{pmatrix} \sum_k \rho z^{(k)} / [\rho^{(k)}(n^{(k)} - 1)] \\ \sum_k \rho z^{(k)} n^{(k)} B^{(k)} / [\rho^{(k)}(n^{(k)} - 1)] \\ \sum_k \rho z^{(k)} B^{(k)} / \rho^{(k)} \end{pmatrix} &= \mathbf{0}, \\ \frac{d}{dt} \begin{pmatrix} \sum_k \rho z^{(k)} q^{(k)} \\ \sum_k \rho z^{(k)} c^{(k)} \end{pmatrix} + D_j^a \begin{pmatrix} u \sum_k \rho z^{(k)} q^{(k)} \\ u \sum_k \rho z^{(k)} c^{(k)} \end{pmatrix} &= \mathbf{0}. \end{aligned} \quad (2.34)$$

Since only mixture density, species density, and species mass fraction vary in time and space, Eqs.(2.34) are discretizations of the following two transport equations for mass fraction:

$$\frac{\partial}{\partial t}(\rho z^{(k)}) + \frac{\partial}{\partial x}(\rho z^{(k)} u) = 0, \quad (2.35a)$$

$$\frac{\partial}{\partial t}\left(\frac{\rho}{\rho^{(k)}}z^{(k)}\right) + u\frac{\partial}{\partial x}\left(\frac{\rho}{\rho^{(k)}}z^{(k)}\right) = 0. \quad (2.35b)$$

From Eq. (2.6), Eqs. (2.35) are mathematically equivalent to those for volume fraction, such that the same conditions as those listed in section 2.5.2.2 hold to maintain pressure and temperature equilibria.

2.5.3 Summary of the analysis

The analysis in the previous section indicates that all three approaches (γ , volume fraction and mass fraction) can be designed to prevent pressure and temperature errors. For two fluids, the γ -based approach is computationally more expensive because one transport equation must be solved for each property in the equation of state (five here); for more than two fluids it may become more attractive, but if fluids have the same properties additional transport equations must be solved to distinguish the different fluids.

The volume fraction and mass fraction approaches are mathematically equivalent. These approaches are not tailored to a given equation of state; however, analysis is required to determine how to calculate the material properties entering the equation of state. For each additional fluid, two additional transport equations must be computed. The reduced five-equation model (with $\Gamma_{kk'} = 0$) is strictly applicable only to flows of immiscible fluids (no physical mixture regions); for miscible flows, $\Gamma_{kk'} \neq 0$ and the source term in the transport equation must be computed, which may lead to difficulties with shock jump conditions and positivity of volume fraction. These approaches can be extended to more general equations of state, such as Mie-Grüneisen (e.g., see [Henry de Frahan et al., 2015](#)).

2.6 Numerical implementation

For the simulations presented in this work, time marching is handled with a third-order accurate explicit strong stability preserving Runge-Kutta scheme Gottlieb & Shu (1996). For the spatial discretization, a solution-adaptive high-order accurate central difference/discontinuity-capturing method is proposed. This method can represent both broadband flow motions and discontinuities accurately and efficiently. The basic idea is that non-dissipative methods are used where the solution is smooth, while the more dissipative and computationally expensive capturing schemes are applied near discontinuous regions. For this purpose, a discontinuity sensor discriminates between smooth and discontinuous (shocks, contacts and interfaces) regions, which all require a different treatment; smooth regions are computed using central differences, a finite difference weighted essentially non-oscillatory (WENO Jiang & Shu, 1996) scheme with Lax-Friedrichs flux splitting handles shock waves, and the approach of Johnsen & Colonius (2006) is used for material interfaces.

To illustrate the specifics, we consider the semi-discrete form of the 1D Euler equations for simplicity,

$$\frac{d}{dt}u + \frac{F_{i+1/2} - F_{i-1/2}}{\Delta x} = 0, \quad (2.36)$$

where u is the vector of conserved variables and F is the numerical flux, which can be written

$$F_{i+1/2} = b_1 F_{i+\frac{1}{2}}|_{central} + b_2 F_{i+\frac{1}{2}}|_{shock} + b_3 F_{i+\frac{1}{2}}|_{int}, \quad (2.37)$$

where b_i represent the value of the sensor in different regions. The sensor values are $b_1 = 1$ and $b_2, b_3 = 0$ for smooth regions, $b_2 = 1$ and $b_1, b_3 = 0$ for shocks and $b_3 = 1$ and $b_1, b_2 = 0$ for interfaces. The capability of the sensor to distinguish between discontinuous and smooth regions highly affects the overall accuracy and performance (Johnsen *et al.*, 2010). We adapt the sensor of Henry de Frahan *et al.* (2015) to finite differences. At each cell edge, L and R denote the value of the corresponding variable at the left and right of the computational cell respectively. Accordingly,

shocks are detected using the function below:

$$\Phi = \frac{2\phi}{(1 + \phi)^2}, \quad \phi = \frac{p_R - p_L}{p_R + p_L}. \quad (2.38)$$

If Φ is greater than 0.01, the corresponding cell is flagged to be treated by shock capturing. Contact discontinuities, also treated by shock capturing, are detected as follows:

$$\Xi = \frac{2\xi}{(1 + \xi)^2}, \quad \xi = \frac{\rho_R - \rho_L}{\rho_R + \rho_L}. \quad (2.39)$$

Finally, material interfaces, to be handled with the method of [Johnsen & Colonius \(2006\)](#) are detected as follows:

$$Z = \frac{2\zeta}{(1 + \zeta)^2}, \quad \zeta = \frac{n_R - n_L}{n_R + n_L}. \quad (2.40)$$

The thresholds for Ξ or Z are set to be 0.01. Although the optimal threshold values for both shocks and interfaces may be problem-dependent, our numerical experiments show a robust detection of discontinuities for the chosen values, which are slightly different from those in [Henry de Frahan et al. \(2015\)](#) because of the different spatial discretization. This approach is easily applicable to multiple dimensions.

In smooth regions, fourth-order central differences are used for the convective terms, both for the conservative and non-conservative equations as proposed by [Movahed & Johnsen \(2013\)](#):

$$F_{i+1/2}^{Central} = \frac{1}{12}(-F_{i+2} + 7F_{i+1} + 7F_i - F_{i-1}). \quad (2.41)$$

Second derivatives (e.g., for diffusion) are also treated with fourth-order differences; for an arbitrary variable A ,

$$A_{xx}|_i = \frac{-A_{i+2} + 16A_{i+1} - 30A_i + 16A_{i-1} - A_{i-2}}{12\Delta x^2}. \quad (2.42)$$

Shock waves are captured using the fifth-order accurate finite difference WENO of [Jiang &](#)

Shu (1996). For this purpose, we use Lax-Friedrichs flux splitting,

$$F^\pm(u) = \frac{1}{2}(F(u) \pm \lambda u), \quad \text{with } F_{i+1/2}^{LXF} = \hat{F}_{i+1/2}^+ + \hat{F}_{i+1/2}^-. \quad (2.43)$$

where $\lambda = \max_u |F'(u)|$ over the relevant range of u . Since these regions are not flagged as material discontinuities, the central scheme can be used to solve the advection equation for the (constant) material properties.

For material interfaces, the WENO procedure proposed by Johnsen & Colonius (2006) is used, which corresponds to a second-order finite difference approximation; however, this reduction in order is not problematic since this approach is used at material discontinuities only, where the solution reduces to first order anyways. An HLL Riemann solver (Harten *et al.*, 1983) is used for upwinding. To correctly treat the non-conservative transport equations, we extend the expression in Saurel & Abgrall (1999b) to high-order WENO:

$$F_{i+1/2}^{HLL} = \frac{S^+ F_{i+1/2}^L - S^- F_{i+1/2}^R + S^+ S^- (U_{i+1/2}^R - U_{i+1/2}^L)}{S^+ - S^-}, \quad (2.44)$$

where $U_{i+1/2}^R$ and $U_{i+1/2}^L$ are the reconstructed variables on the right and left of cell $i+1/2$, $F_{i+1/2}^R$ and $F_{i+1/2}^L$ are the corresponding fluxes, and S^+ and S^- are the right and left wave speed, respectively, calculated from:

$$S^+ = \max(0, u_{i+1/2}^R + a_{i+1/2}^R, u_{i+1/2}^L + a_{i+1/2}^L), \quad S^- = \min(0, u_{i+1/2}^R - a_{i+1/2}^R, u_{i+1/2}^L - a_{i+1/2}^L), \quad (2.45)$$

where u and a stand for velocity and sound speed, respectively. The discretized form of the non-conservative transport equation for an arbitrary variable A is

$$\begin{aligned} A_i^{n+1} = A_i^n - \frac{\Delta t}{\Delta x} \left[\frac{u_i^n (S_{i+1/2}^+ A_{i+1/2,R}^n - S_{i+1/2}^- A_{i+1/2,L}^n) + S_{i+1/2}^+ S_{i+1/2}^- (A_{i+1/2,R}^n - A_{i+1/2,L}^n)}{S_{i+1/2}^+ - S_{i+1/2}^-} \right. \\ \left. - \frac{u_i^n (S_{i-1/2}^+ A_{i-1/2,R}^n - S_{i-1/2}^- A_{i-1/2,L}^n) + S_{i-1/2}^+ S_{i-1/2}^- (A_{i-1/2,R}^n - A_{i-1/2,L}^n)}{S_{i-1/2}^+ - S_{i-1/2}^-} \right]. \end{aligned} \quad (2.46)$$

2.7 Results

The compressible Navier-Stokes equations, non-dimensionalized by the density and sound speed of air at atmospheric pressure, characteristic length $L = 0.2$ mm, and $T = 300$ K, are solved for all problems. The time step is adaptively set to satisfy the advection and diffusion constraints, with CFL number 0.95 and VNN 0.475. We consider the γ , volume fraction (or “ α ”) and mass fraction (or “ z ”) models described in section 2.5.2; when referring to our proposed approach, we mean an approach that preserves velocity, pressure and temperature equilibria (for an isolated interface). We make comparisons to current schemes in the literature designed to maintain velocity and pressure equilibria in the absence of heat conduction, which we call “pressure only” (e.g., the methods in [Abgrall, 1996](#); [Shyue, 1998](#)); with these approaches, temperature is computed from the available data; e.g., for the γ -model, B would be computed from $nB/(n - 1)$ and $1/(n - 1)$, rather than being advected as we propose. The α and z “pressure only” approaches are identical, so only the z approach is considered. Water and air have values taken from Table 2.1.

2.7.1 1D smooth advection problem

We consider the advection of a smooth distribution in density and n to show that our solution-adaptive method achieves the correct convergence rate for smooth problems. The following initial conditions are used

$$(\rho, u, p, T, n) = (1 + 0.2 \sin(4\pi x), 1, 1, 1, 1.4 + 0.2 \sin(\pi x)). \quad (2.47)$$

This distribution moves at constant speed u , with constant pressure and temperature in the periodic domain $x \in [0, 1]$. The L_∞ errors in n , pressure and temperature are shown in Figure (2.1) after one period and for different resolutions. Pressures and temperatures remain near round-off, thus demonstrating that pressure and temperature equilibria are maintained. The convergence rate (in n) is fourth, the order of the finite difference scheme.

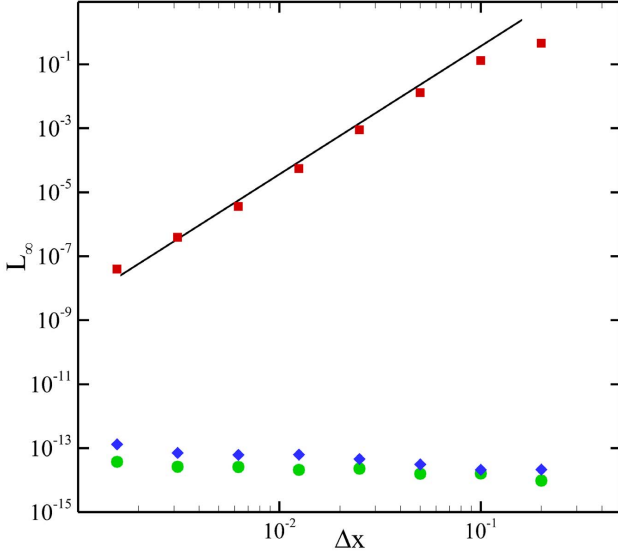


Figure 2.1: L_∞ error for the 1D smooth advection problem. Red squares: n ; blue diamonds: pressure; green circles: temperature.

2.7.2 1D air/water interface advection

We numerically verify our theoretical development for the isolated interface advection problem in section 2.5.1, e.g., for a 1D air bubble in water. We consider an initially sharp top-hat distribution of air in water at the same temperature and pressure, moving at a constant speed u in the periodic domain $x \in [0, 1]$. The initial conditions are,

$$(\rho, u, p, T) = \begin{cases} (1, 0.5, 0.716, 1) & \text{if } x/L \in [0.25, 0.75] \\ (848.28, 0.5, 0.716, 1) & \text{otherwise} \end{cases} \quad (2.48)$$

The properties entering the equation of state are initialized using the same top-hat distribution. The results for all three models with the “pressure only” and our proposed approaches using 200 points are shown in Figures 2.2 (density, pressure and temperature profiles after one period) and 2.3 (time evolution of the L_∞ error in u, p, T). The results clearly indicate that our proposed approaches do not introduce errors in pressure, temperature or velocity. On the other hand, if using approaches that are designed to only preserve pressure and velocity equilibria, and using only the available data to compute temperature, then errors are produced in the temperature, which then propagate to the

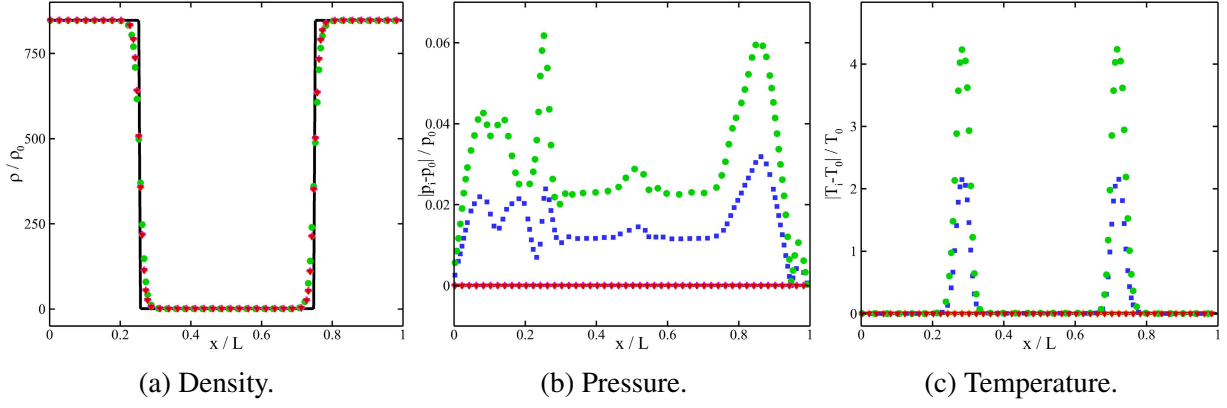


Figure 2.2: Profile of the advection of an air/water interface after one period. Black solid line: initial and exact solution; green circles: “pressure only” γ approach; blue squares: “pressure only” z approach; pink pluses: proposed γ approach; red triangles: proposed α approach; orange diamonds: proposed z approach.

other fields due to the heat diffusion and pressure terms. The resulting errors are non-negligible, particularly for the temperature. If the Fourier heat conduction term had not been included no such errors would occur.

2.7.3 1D gas-liquid Riemann problem

We consider gas-liquid Riemann problems to compare the “pressure only” and our proposed α approaches for shock-dominated interfacial flows; similar results are obtained with the other models. The initial conditions (with water on the left, air on the right) are (Allaire *et al.*, 2002; Murrone & Guillard, 2005):

$$(\rho, u, p) = \begin{cases} (1000, 0, 8300) & \text{if } x/L \in [0, 0.7] \\ (50, 0, 0.83) & \text{if } x/L \in [0.7, 1] \end{cases} \quad (2.49)$$

The domain is discretized with 1,000 cells and the exact solution is the converged solution on 5,000 cells. The profiles of density, pressure, temperature, velocity, and volume fraction for both approaches are shown in Figure (2.4). Our proposed approach shows good agreement with the exact solution. For the “pressure only” approach at this high pressure ratio (10,000:1) and heavy gas, temperature errors are clear at the interface, but pressure errors are not substantial.

Another gas-liquid Riemann problem is considered with initial conditions more relevant to our

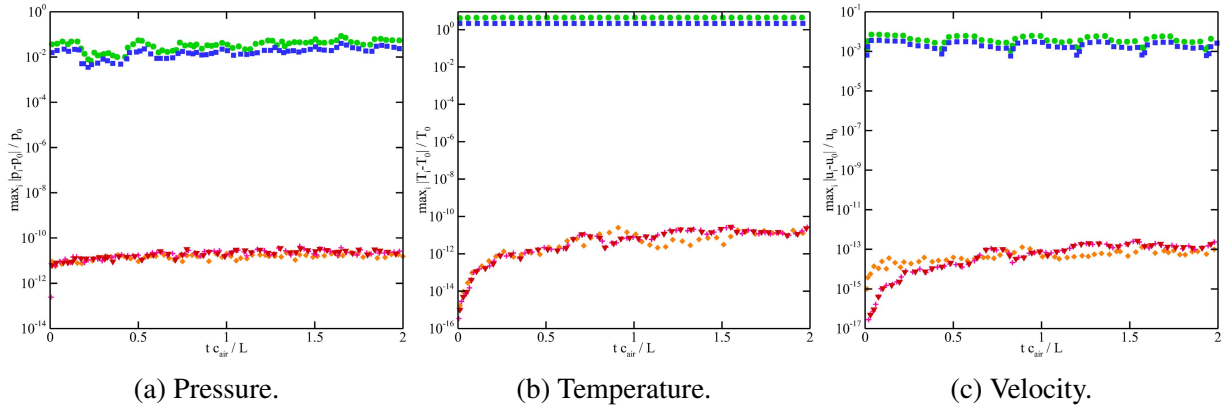


Figure 2.3: Time histories of normalized L_∞ errors for the advection of an air/water interface after one period. Black solid line: initial and exact solution; green circles: “pressure only” γ approach; blue squares: “pressure only” z approach; pink pluses: proposed γ approach; red triangles: proposed α approach; orange diamonds: proposed z approach.

interests (1D shock-bubble interaction):

$$(\rho, u, p) = \begin{cases} (881.6, 0.184, 714) & \text{if } x/L \in [0, 0.7] \\ (1, 0, 0.714) & \text{if } x/L \in [0.7, 1] \end{cases} \quad (2.50)$$

The domain is discretized with 1000 cells and the exact solution is the converged solution on 5,000 cells. The profiles of density, pressure, temperature, velocity, and volume fraction for both approaches are shown in Figure (2.5). The numerical solution agrees well with the exact solution. In this problem, the effect of heat diffusion is significant inside the bubble. On the other hand, the “pressure only” approach gives rise to a large temperature error at the interface, as well as erroneous density, velocity, pressure and temperature between the interface and shock.

2.7.4 3D shock-bubble interaction

To determine the implications for relevant bubble dynamics problems, we consider the interaction of a shock wave in water with an air bubble near a rigid wall, as in Johnsen & Colonius (2009).

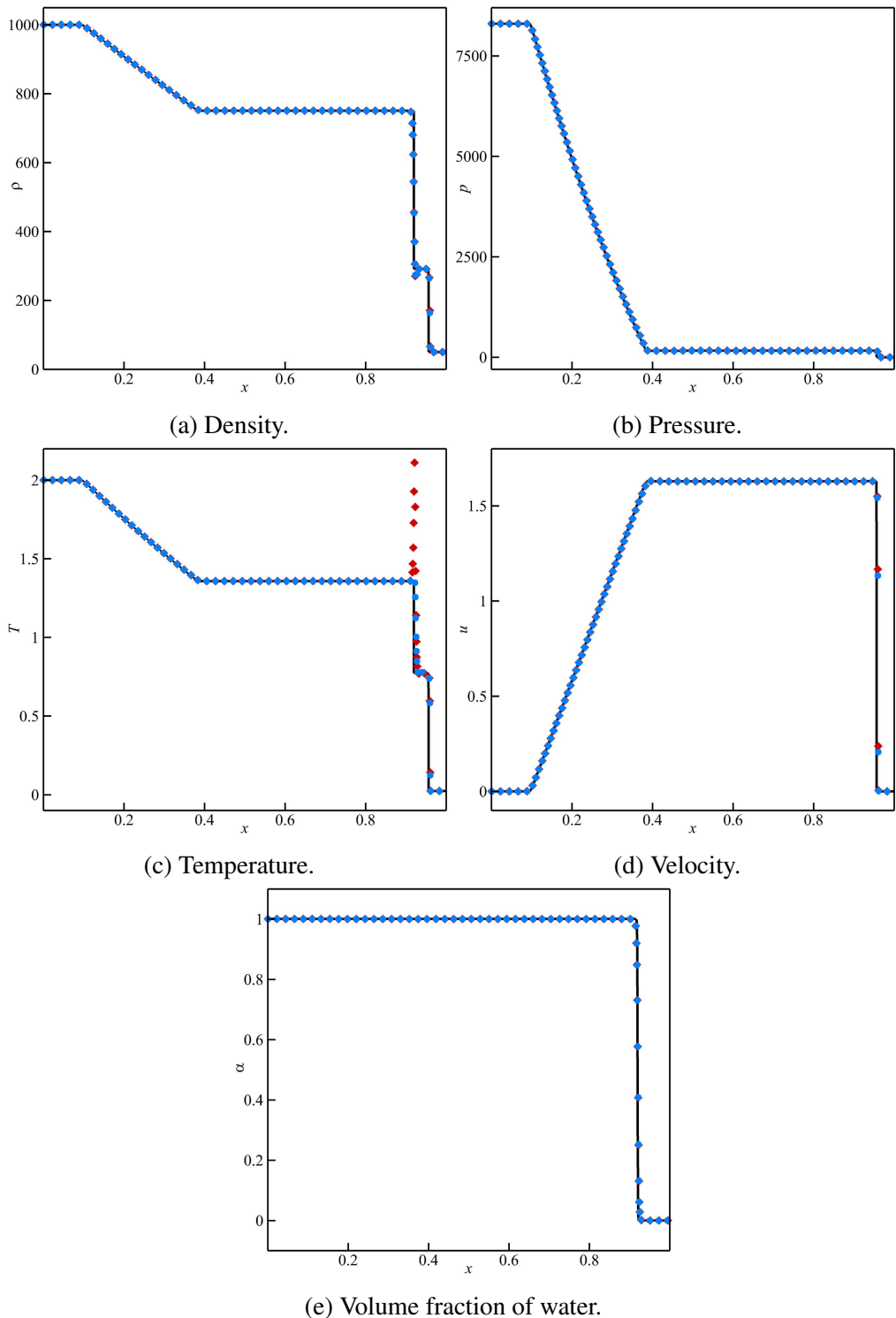


Figure 2.4: Gas-liquid Riemann problem. Black solid line: exact solution; blue filled circles: proposed approach; red filled diamonds: “pressure only” approach.

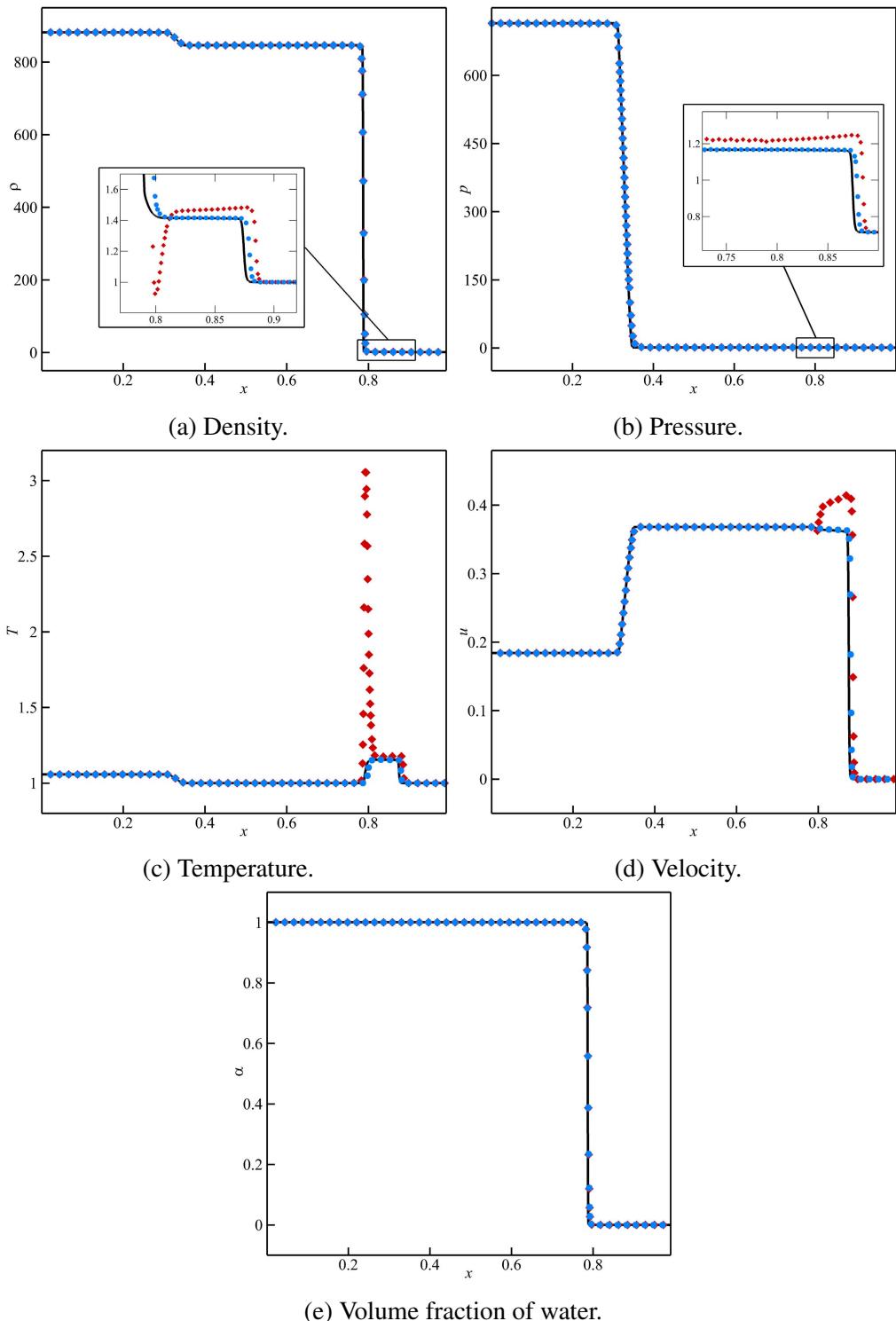


Figure 2.5: Gas-liquid Riemann problem (1D shock-interface). Black solid line: exact solution; blue filled circles: proposed approach; red filled diamonds: “pressure only” approach.

Initially, the spherical bubble is in equilibrium with its surroundings:

$$(\rho, u, v, w, p, T) = \begin{cases} (1, 0, 0, 0, 0.714, 1) & \text{in the bubble,} \\ (846.2, 0, 0, 0, 0.714, 1) & \text{in the water upstream of the shock.} \end{cases} \quad (2.51)$$

Two different shock strengths are considered:

- Case 1: weak shock wave with pressure ratio of 100 (Mach 1.0035)

$$(\rho, u, v, w, p, T) = (849.8, 0.0188, 0, 0, 71.4, 1.006) \quad \text{in the water downstream of the shock.} \quad (2.52)$$

- Case 2: strong shock wave with pressure ratio of 1000 (Mach 1.035)

$$(\rho, u, v, w, p, T) = (881.6, 0.184, 0, 0, 714, 1.06) \quad \text{in the water downstream of the shock.} \quad (2.53)$$

This problem is simulated using the “pressure only” and our proposed α approaches on a $500 \times 400 \times 400$ uniform grid for both cases. The initial stand-off distance of the bubble from the wall is 1.1. By symmetry, only a quarter of the bubble is computed, with symmetry boundary conditions along the relevant planes. The wall a purely reflecting, with no slip. Zero gradient conditions are used along the remaining boundaries.

The results are compared to evaluate the effects of temperature errors; quantities related to pressures and temperatures along the wall, as well as bubble dynamics are of particular interest. Figures. (2.6) and (2.7) show the pressure gradient magnitude and temperature contours at different times during the process. The right-moving shock interacts with the bubble, thus producing a reflected rarefaction wave. As the bubble starts its collapse, the incoming shock hits the rigid wall and reflects back onto the bubble. During the collapse, a re-entrant jet directed toward the wall is produced, which, upon impact with the distal side, generates an outward propagating shock. Even though the “pressure only” approach is designed to prevent pressure errors, such errors are

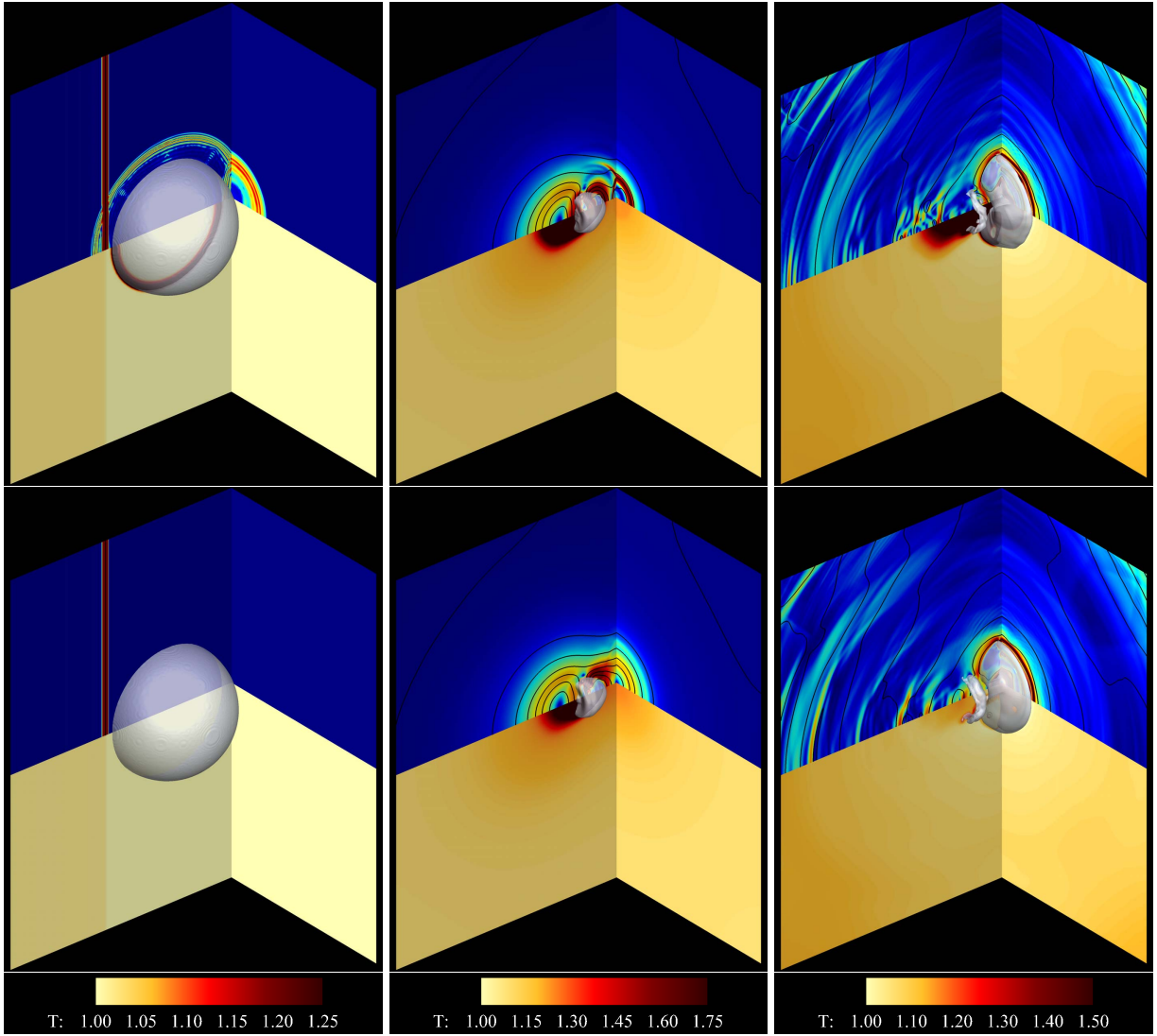


Figure 2.6: Shock-induced bubble collapse (case 1, $p_s/p_o = 100$) at different times $t = 0.04, 1.49, 2.05$. top row: “pressure only” approach; bottom row: proposed approach; top contour: pressure gradient magnitude; bottom contour: temperature.

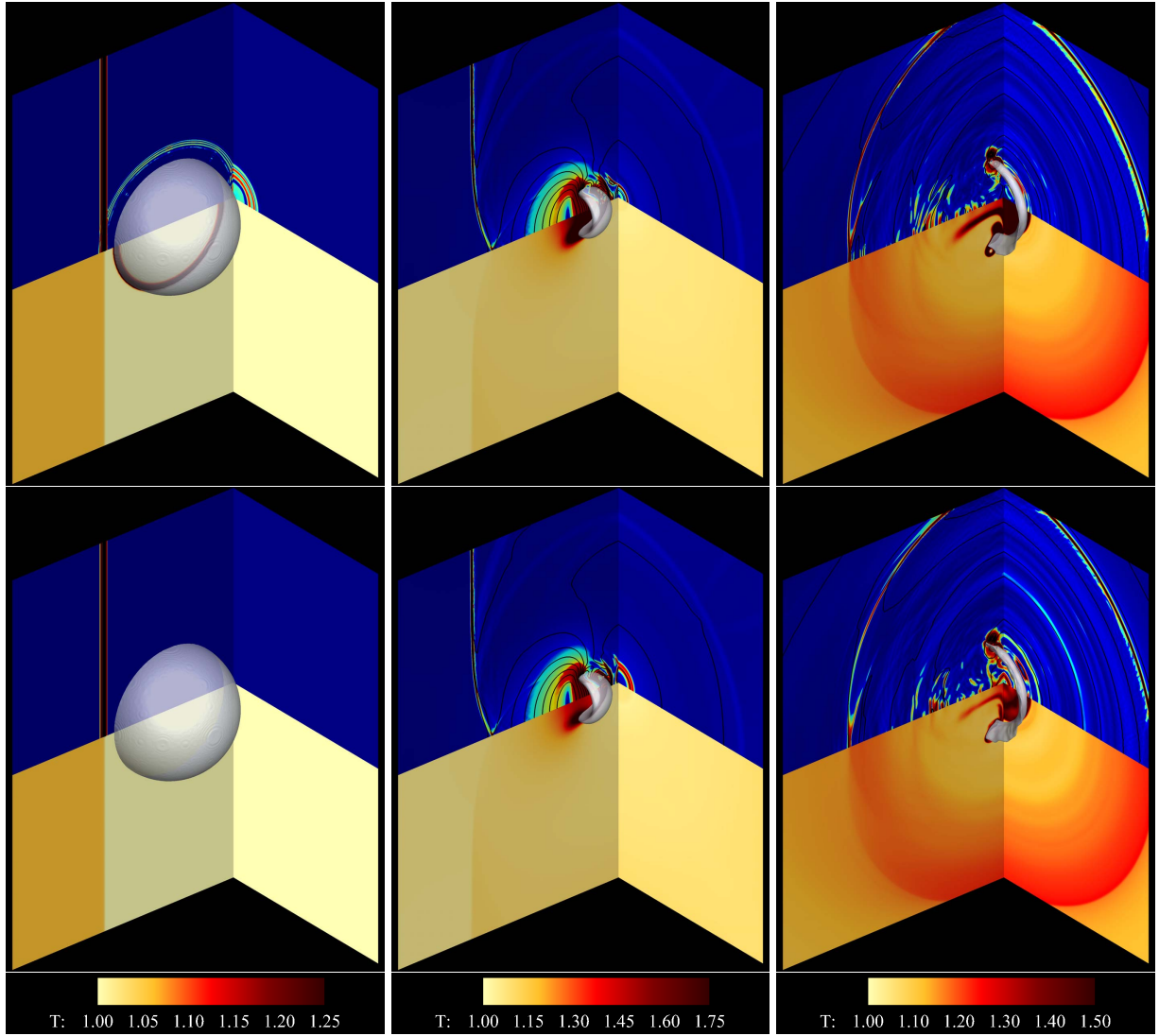


Figure 2.7: Shock-induced bubble collapse (case 2, $p_s/p_o = 1000$) at different times $t = 0.03, 0.6, 0.92$. top row: “pressure only” approach; bottom row: proposed approach; top contour: pressure gradient magnitude; bottom contour: temperature.

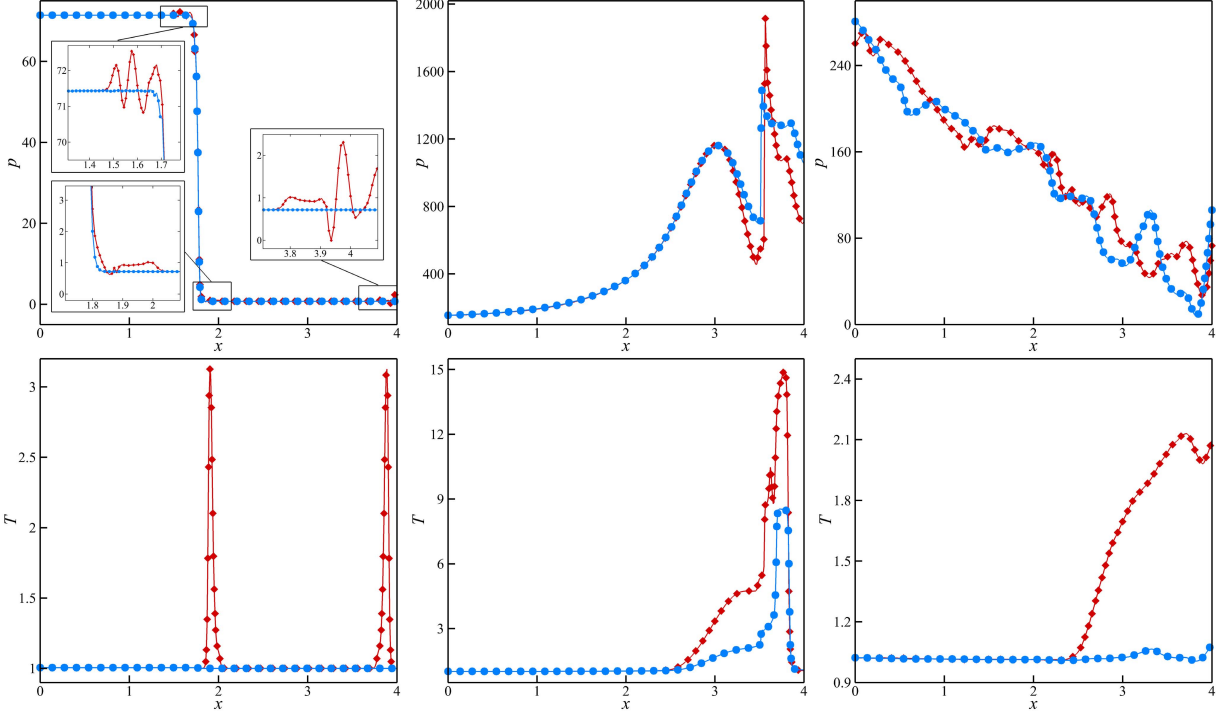


Figure 2.8: Shock-induced bubble collapse (case 1, $p_s/p_o = 100$) – Centerline properties (top row: pressure; bottom row: temperature) at times 0.04, 1.49, 2.05. Red diamonds: “pressure only” approach; blue circles: proposed approach.

generated because of the large temperature spike across the bubble interface. The most striking discrepancies lie in the temperature contours, particularly in the region just outside the bubble after collapse. The pressure gradient magnitude shows how these temperature errors propagate in the pressure field. These temperature errors strongly affect the simulations and may ultimately cause the code to fail.

To quantitatively evaluate these errors, Figures. (2.8) and (2.9) show the pressure and temperature along the centerline at different times, and Figures. (2.10) and (2.11) plot time histories of the wall pressure and temperature at point A (along the centerline and on the wall), and total enstrophy for both cases. The temperature errors initially consist of spikes along the interface of over 100% error. Much of the temperature discrepancies appear to be localized at the interface, though some regions in which the interface was previously located appear to still bear memory of these errors. Temperature errors are particularly important for case 1 ($p_s/p_o = 100$). The pressure oscillations emanating from these temperature errors exhibit the largest discrepancies after collapse in

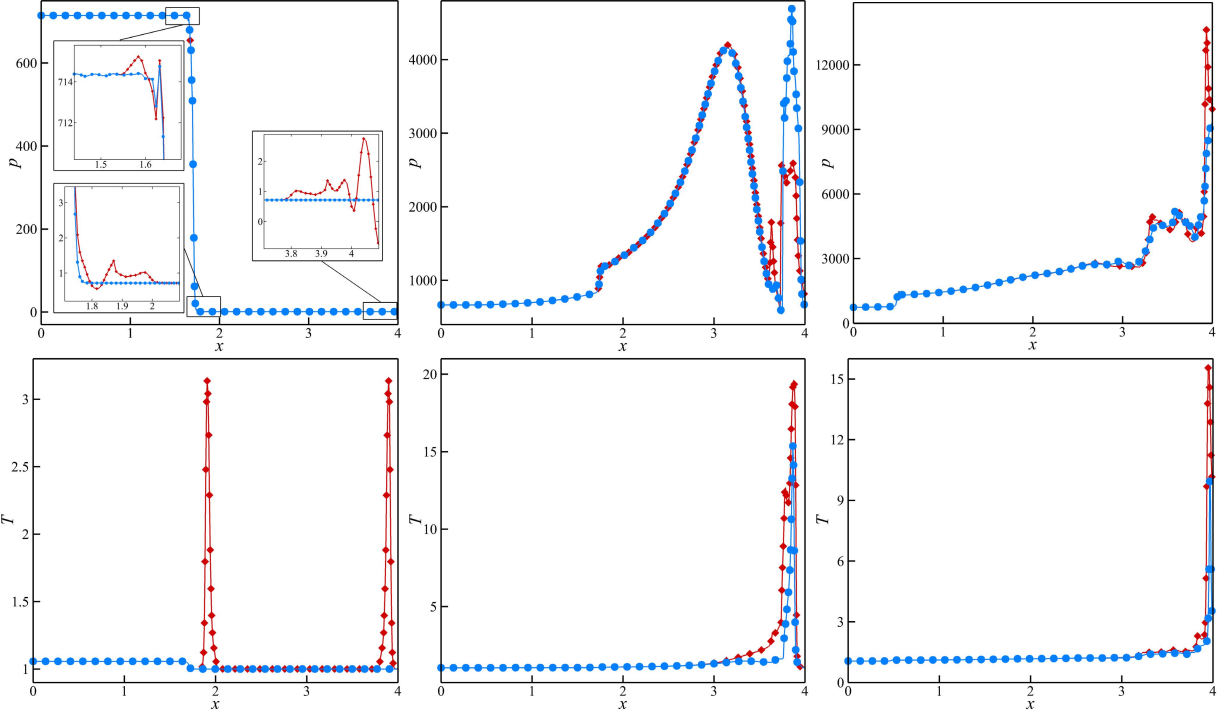


Figure 2.9: Shock-induced bubble collapse (case 2, $p_s/p_o = 1000$) – Centerline properties (top row: pressure; bottom row: temperature) at times 0.03, 0.6, 0.73. Red diamonds: “pressure only” approach; blue circles: proposed approach.

the region between the bubble and the wall, with local errors nearly 100%. Along the wall, the discrepancies in pressure are on the order of 10%, while the temperature errors are more than 100%, always overshoots: for case 1, the maximum wall pressure and temperature in the simulation for the proposed approach are 2,356 and 1.2, while the “pressure only” approaches yield 2,550 and 2.2; for case 2, the maximum wall pressure and temperature in the simulation for the proposed approach are 14,450 and 4.1, while the “pressure only” approaches yield 15,300 and 10.2. These discrepancies even affect the vorticity contents of the flow and possibly generation of small-scale features, due to baroclinic vorticity generated along the interface, due to pressure oscillations.

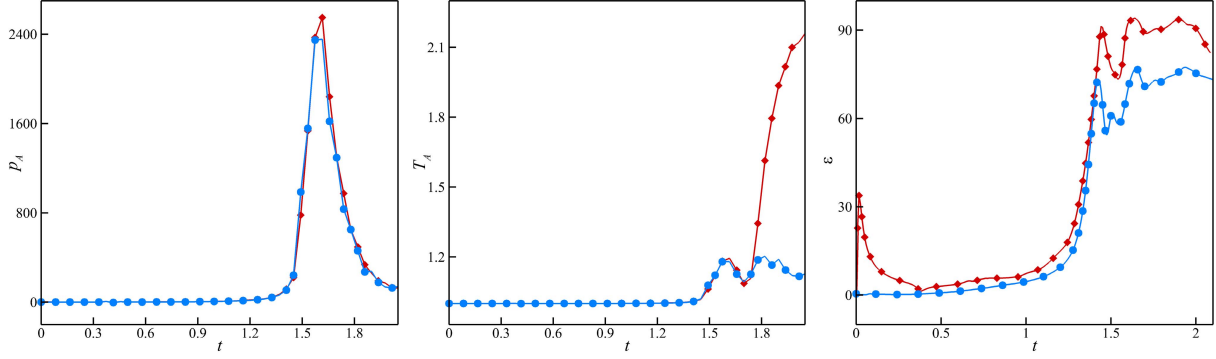


Figure 2.10: Shock-induced bubble collapse (case 1, $p_s/p_o = 100$) – Time histories of the pressure (left) and temperature (center) at point A and total enstrophy (right). Red diamonds: “pressure only” approach; blue circles: proposed approach.

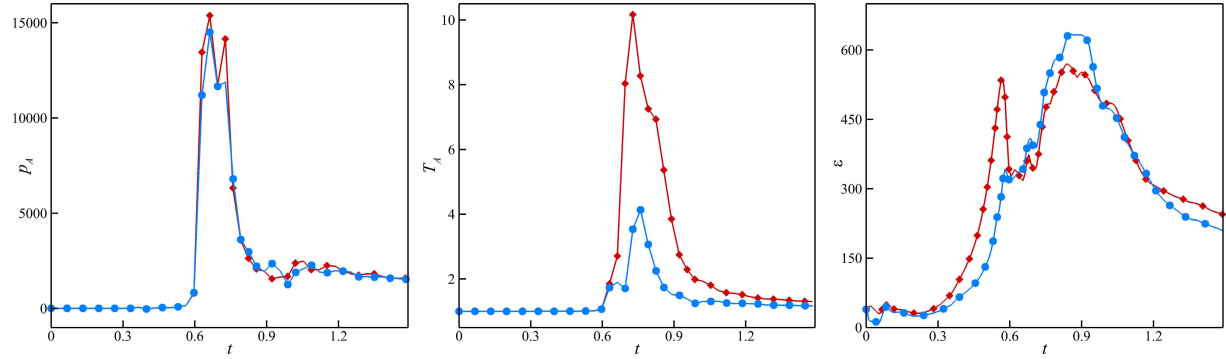


Figure 2.11: Shock-induced bubble collapse (case 2, $p_s/p_o = 1000$) – Time histories of the pressure (left) and temperature (center) at point A and total enstrophy (right). Red diamonds: “pressure only” approach; blue circles: proposed approach.

Part II:

Bubble dynamics

CHAPTER 3

Physical/numerical modeling

This chapter presents the physical and numerical modeling used to perform bubble dynamics simulations. Although the approach detailed in the previous chapter was state-of-the-art at that time, we extended it to include a more realistic equation of state and improved numerics. First, we describe the governing equations. Next, the Nobel-Abel Stiffened-Gas equation of state, representing water in liquid and vapor phases, is explained. Afterwards, we present the multiphase modeling employed to simulate inertial collapse of vapor bubbles near a rigid surface. Then, a summary of computational framework is provided. Finally, the problems of interest in this study, and the convergence analysis of current simulations are described.

3.1 Governing equations

The compressible Navier-Stokes equations for a binary vapor-liquid system govern the flows of interest:

$$\frac{\partial \rho}{\partial t} + \frac{\partial}{\partial x_j}(\rho u_j) = 0, \quad (3.1a)$$

$$\frac{\partial \rho u_i}{\partial t} + \frac{\partial}{\partial x_j}(\rho u_i u_j + p \delta_{ij}) = \frac{\partial \tau_{ij}}{\partial x_j}, \quad (3.1b)$$

$$\frac{\partial E}{\partial t} + \frac{\partial}{\partial x_j}[u_j(E + p)] = \frac{\partial}{\partial x_j}(u_i \tau_{ij} - Q_j), \quad (3.1c)$$

where ρ is the density, u_i the velocity vector, p the pressure, $E = \rho e + \rho u_i u_i / 2$ the total energy, e the internal energy and δ_{ij} the identity tensor. The viscous stress tensor τ_{ij} and heat flux Q_j are given by:

$$\tau_{ij} = \mu \left(\frac{\partial u_i}{\partial x_j} + \frac{\partial u_j}{\partial x_i} - \frac{2}{3} \frac{\partial u_k}{\partial x_k} \delta_{ij} \right) + \mu_B \frac{\partial u_k}{\partial x_k} \delta_{ij}, \quad Q_j = -\kappa \frac{\partial T}{\partial x_j}, \quad (3.2)$$

where μ is the dynamic shear viscosity ($8.3 \times 10^{-4} \text{ kgm}^{-1}\text{s}^{-1}$ for liquid water and $9.7 \times 10^{-6} \text{ kgm}^{-1}\text{s}^{-1}$ for water vapor), μ_B is the bulk viscosity ($2.6 \times 10^{-3} \text{ kgm}^{-1}\text{s}^{-1}$ for liquid water and $5.8 \times 10^{-6} \text{ kgm}^{-1}\text{s}^{-1}$ for water vapor), and κ the heat conductivity ($6.1 \times 10^{-1} \text{ Jkg}^{-1}\text{K}^{-1}$ for liquid water and $1.8 \times 10^{-2} \text{ Jkg}^{-1}\text{K}^{-1}$ for water vapor). Surface tension and mass transfer are not expected to change the collapse dynamics, since the time scales of the flow are short in comparison; therefore, these effects are neglected, as done in other previous studies (Johnsen & Colonius, 2009; Hawker & Ventikos, 2012; Tiwari *et al.*, 2015).

3.2 Equation of state

To close the system of equations, a relation between pressure, temperature and internal energy valid for water vapor and liquid water is required. In the second part of the thesis, we use the Nobel-Abel Stiffened-Gas equation of state (NASG EOS), which is a more recent, and realistic equation of state introduced by Le Métayer & Saurel (2016). This relation, which is a combination of the so-called “Noble-Abel” and “stiffened gas” equations of state, shows a better agreement with analytical and experimental saturation curves for a wider ranges of temperature, and can be used to model both water vapor and liquid water. According to Nobel-Abel Stiffened-Gas equation of state equation of state, the relationships between pressure, temperature and internal energy are given by:

$$\rho(e - q) = \frac{p}{n - 1}(1 - \rho b) + \frac{nB}{n - 1}(1 - \rho b), \quad (\text{pressure-wise}) \quad (3.3a)$$

$$= \rho cT + B(1 - \rho b). \quad (\text{temperature-wise}) \quad (3.3b)$$

Coefficients	Vapor phase	Liquid phase
n	1.47	1.19
$B (MPa)$	0	702.8
$b (kg/m^3)$	0	6.61×10^{-4}
$c (J/kgK)$	955	3610
$q (J/kg)$	2.1×10^6	-1.2×10^6

Table 3.1: Relevant constants in the Nobel-Abel Stiffened-Gas equation of state equation of state for water.

Similar to the equation of state presented in Chapter 2, the parameters n , B , b , q , and c are material-dependent properties, determined from experimental saturation curves. For liquid water and water vapor, the relevant constants take the values shown in Table 3.1. In the same way, for the case of ideal gases, $n = \gamma$, and $c = c_v$ are the specific heat ratio, and the specific heat at constant volume, respectively; B , q , and b are zero, so that the Eq. (3.3) reduces into the well-known ideal gas relation. Using the Nobel-Abel Stiffened-Gas equation of state formulation, the sound speed can be written as:

$$a^2 = \frac{n(p + B)}{\rho(1 - \rho b)}. \quad (3.4)$$

3.3 Multiphase model

Owing to ease of applicability of the volume fraction approach to different types of equation of state (presented in previous chapter), we employ this method to introduce multiple phases into the system of equations. According to this model, we need to solve two additional transport equations for volume fraction in conservative and non-conservative forms:

$$\frac{\partial(\rho^{(k)}\alpha^{(k)})}{\partial t} + \frac{\partial}{\partial x_j} \left(\rho^{(k)}\alpha^{(k)} u_j \right) = 0, \quad (3.5a)$$

$$\frac{\partial\alpha^{(k)}}{\partial t} + u_j \frac{\partial\alpha^{(k)}}{\partial x_j} = \Gamma_{kk'} \frac{\partial u_j}{\partial x_j}, \quad (3.5b)$$

where

$$\Gamma_{kk'} = \alpha^{(k)} \alpha^{(k')} \frac{\rho^{(k')}(a^{(k')})^2 - \rho^{(k)}(a^{(k)})^2}{\alpha^{(k)} \rho^{(k')}(a^{(k')})^2 + \alpha^{(k')} \rho^{(k)}(a^{(k)})^2}, \quad (3.6)$$

and $\rho^{(k)}$, $\alpha^{(k)}$ and $a^{(k)}$ are the density, volume fraction and the sound speed in phase/fluid k , respectively. Also, the effects of the source term in Eq. 3.5b, neglected in volume fraction approach in Chapter 2, are taken into account hereafter (the so-called five-equation model [Kapila et al., 2001](#)).

However, as previously discussed, a naive implementation of this model leads to generation of spurious pressure and temperature oscillations across the material discontinuities. To prevent such numerical errors, we adopt the volume fraction approach of [Beig & Johnsen \(2015a\)](#) for the parameters entering the Nobel-Abel Stiffened-Gas equation of state. Accordingly, pressure and temperature are calculated using the following relations:

$$p = \left[\rho e - \sum_k \alpha^{(k)} \left(\frac{nB}{n-1} \right)^{(k)} + \sum_k \rho^{(k)} \alpha^{(k)} \left(\frac{nbB}{n-1} \right)^{(k)} - \sum_k \rho^{(k)} \alpha^{(k)} q^{(k)} \right] / \left[\sum_k \alpha^{(k)} \left(\frac{1}{n-1} \right)^{(k)} - \sum_k \rho^{(k)} \alpha^{(k)} \left(\frac{b}{n-1} \right)^{(k)} \right], \quad (3.7)$$

$$T = \left[\rho e - \sum_k \alpha^{(k)} B^{(k)} + \sum_k \rho^{(k)} \alpha^{(k)} (bB)^{(k)} - \sum_k \rho^{(k)} \alpha^{(k)} q^{(k)} \right] / \sum_k \rho^{(k)} \alpha^{(k)} c^{(k)}, \quad (3.8)$$

where $\rho^{(k)} \alpha^{(k)}$ is computed from the conservative form, and $\alpha^{(k)}$ is calculated using the non-conservative form of the volume fraction transport equation (3.5).

3.4 Numerical framework

The numerical approach proposed by [Beig & Johnsen \(2015a\)](#), which is capable of simulating compressible multiphase flows, is employed in an in-house computational code to simulate the problems of interest. To carry out accurate simulations of these problems that effectively resolve the small scale features, high resolution is essential. Three-dimensional high-resolution simulations as well as post-processing massive output files and visualizations require many processors and large amounts of memory. High-performance computing techniques are therefore paramount

to make the simulations possible. Accordingly, a brief description of the computational framework of this study is provided below:

- Spatial discretization (advection):

To approximate advection fluxes, a solution-adaptive high-order accurate central difference/discontinuity-capturing method is proposed (Beig & Johnsen, 2015a). This method can represent both broadband flow motions and discontinuities stably, accurately and efficiently. The basic idea is that non-dissipative methods are used where the solution is smooth, while the more dissipative and computationally expensive capturing schemes are applied near discontinuous regions (Movahed & Johnsen, 2013). For this purpose, a discontinuity sensor discriminates between smooth and discontinuous (shocks, contacts and interfaces) regions (Henry de Frahan *et al.*, 2015); smooth regions are computed using an explicit fourth-order central differences scheme, and a shock- and interface-capturing approach with fifth-order Weighted Essentially Non-Oscillatory (WENO Jiang & Shu, 1996) reconstruction, and Harten-Lax-van Leer Riemann solver (HLL Harten *et al.*, 1983) is used to handle the discontinuities. This novel approach speed up the simulations significantly.

- Spatial discretization (diffusion):

Diffusive terms (stress components and heat diffusion) are discretized in non-conservative form using a fourth-order explicit central difference scheme.

- Spatial discretization (Eq. 3.5b):

To overcome the numerical difficulties associated with the source term in non-conservative transport equation for volume fraction, we first re-write the corresponding equation (Tiwari *et al.*, 2013) in the following form (see Appendix A):

$$\frac{\partial \alpha^{(k)}}{\partial t} + \frac{\partial}{\partial x_j} (\alpha^{(k)} u_j) = \left[\frac{\alpha^{(k)} \rho^{(k')} (a^{(k')})^2}{\alpha^{(k)} \rho^{(k')} (a^{(k')})^2 + \alpha^{(k')} \rho^{(k)} (a^{(k)})^2} \right] \frac{\partial u_j}{\partial x_j}. \quad (3.9)$$

Then, we employ the same upwinding approach, used to discretize the advective terms, to treat the flux term, while the right-hand side of Eq. 3.9 is computed using the fourth-order

central difference scheme. To prevent the startup errors from crashing the code due to large initial velocity gradients, we set the source term in Eq. 3.5b to zero for 1000 time steps.

- Temporal discretization:

Time marching is handled with a third-order accurate explicit strong-stability-preserving Runge-Kutta scheme [Gottlieb & Shu \(1996\)](#). The time step is adaptively set to satisfy the advection and diffusion constraints.

- Boundary conditions:

Several types of boundary conditions including non-reflecting ([Thompson, 1987](#)), time-dependent ([Thompson, 1990](#)), zero-gradient, periodic, symmetric wall, and no-slip wall are implemented in our code.

- Parallel computing:

The code uses the Message Passing Interface (MPI) to communicate data between processors and efficiently run simulations on thousands of processors at leadership computing facilities.

- I/O:

We employ parallel Hierarchical Data Format (HDF5), a unique technology suite that makes possible the management of extremely large and complex data collections. The code provides one-, two-, and three-dimensional output files that can be used to represent and analyze the flow physics.

- Post-processing and visualization:

We use ParaView in parallel to visualize and process large amounts of data from the simulations.

- Code specifics:

The code is written in C++ and only requires MPI and HDF libraries. A novelty that our current computational code benefits from is the self repairing mechanism. In the case of potential simulation crash, this algorithm will be automatically activated and if the crash

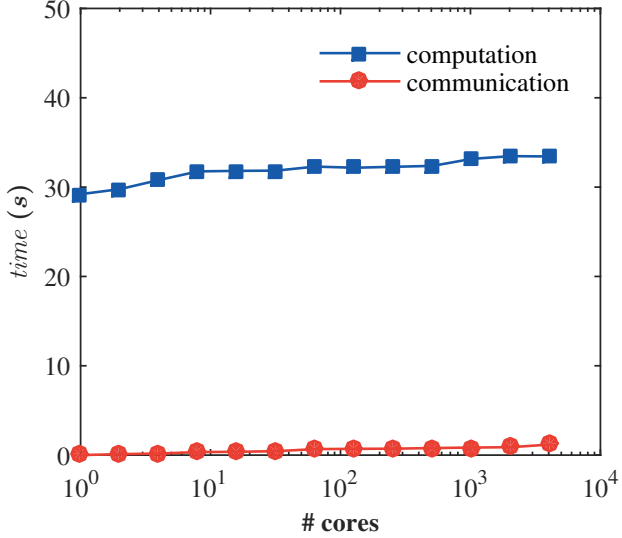


Figure 3.1: Weak scaling of the computational code on a periodic box problem with 32^3 points per core on Stampede.

is caused by a numerical instability, the code will repair the issue and restart from the last restart file. This process happens in a single job running, so it prevents the computational allocation to be wasted because of a code crash, and help us to use the allocation as efficient as possible.

We have performed weak and strong scaling analysis on different supercomputers, and it is shown that the code runs efficiently on thousands of processors. Here, the scaling results on the Stampede machine at Texas Advanced Computing Center (TACC) are presented, where the shock-bubble interaction problem was used as the test case.

For weak scaling, Figure 3.1 shows the time for 100 time step on a triple periodic box problem with 32^3 grid points per core, showing that the code runs efficiently on Stampede. The full time step and the communication times are recorded; the computation time is obtained by deducing these two values from each other. The most obvious result is that the code scales well: the weak scaling efficiency is above 85% for Stampede. The results show good efficiency, given the 4096-fold increase in the number of cores compared to the single-core run.

The strong scaling results performed on a grid of 512^3 are also reported in Figure 3.2. The parallel efficiency stays above 80% up to 4096 cores, i.e., a 4096-fold increase in the number of

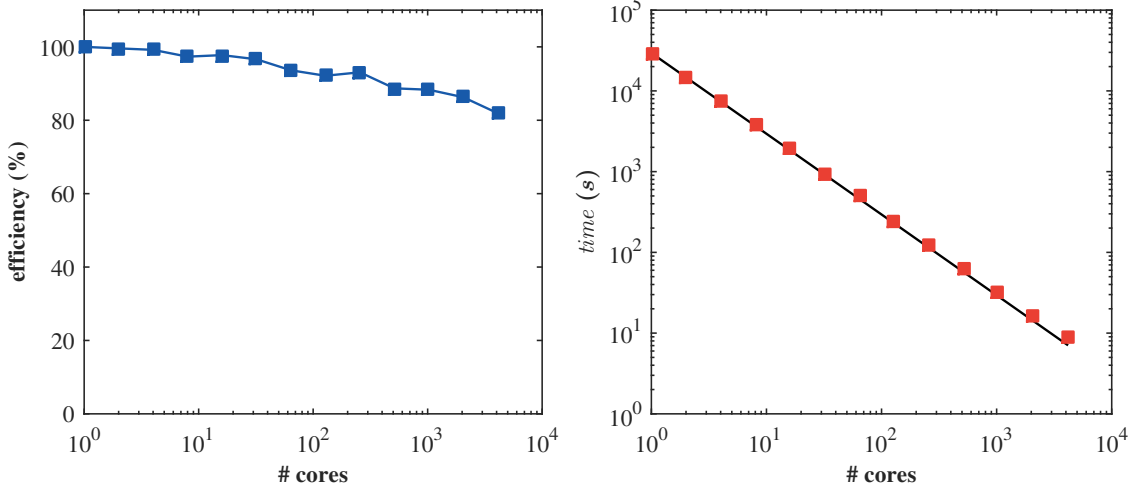


Figure 3.2: Strong scaling of the computational code on periodic box problem with 256^3 grid points on Stampede, efficiency of the code versus number of cores (left), and run time versus number of cores (right).

cores compared to the single-core run on Stampede. Note that very few points (only 32,768 grid points per core) exist at the final data point, which is exceedingly coarse.

3.5 Problem description

In this study, we investigate three main problems, the Rayleigh collapse ([Johnsen & Colonius, 2009](#)) of (a) an isolated vapor bubble in free field, (b) a single vapor bubble near a rigid boundary, and (c) a pair of vapor bubbles near a rigid surface. The Rayleigh collapse is driven by the difference between the pressure of the ambient liquid and that of the bubble at its maximum radius. This problem is of particular interest in the field of hydrodynamic cavitation given its ubiquity in many applications. In the present work, we simulate the collapse process starting at the bubble's maximum radius. The bubble consists of non-condensable water vapor, and the surrounding liquid is water. In fact, the water vapor is treated like a gas with water vapor properties that is represented by Nobel-Abel Stiffened-Gas equation of state. The baseline initial radius, R_o , is 100 μm , the initial bubble temperature, T_o , is 300 K, and the initial pressure inside the bubble, p_o , is 3.55 kPa, the corresponding vapor pressure at T_o . A brief description of the target problems is as follows:

3.5.1 Rayleigh collapse of an isolated vapor bubble in a free field

This problem is the most classic cavitation problem, which has been extensively investigated in a variety of numerical, analytical, and experimental studies in the past century, yet remained a central research topic in the field of cavitation. In this problem, an initially spherical vapor bubble, surrounded by liquid water in a free field, starts to collapse at its maximum radius. The surrounding pressure, p_∞ , is initially uniform around the bubble and is set to 5 MPa. Owing to the symmetry of the problem in three dimensions, we only simulate one eighth of the domain, where we use symmetric boundary condition along the planes with bubble at the corner, and non-reflecting boundary condition elsewhere. A uniform Cartesian grid with the resolution of 192 cells per initial bubble radius (approximately 0.5 billion cells for this problem) is used to simulate the flow. For all cases, we smooth the interfaces initially over three grid cells to prevent the grid dependent instabilities.

3.5.2 Rayleigh collapse of a single vapor bubble near a rigid boundary

In this case, a bubble with initial radius R_o is located at distance H_o from the wall. Figure 3.3 illustrates the problem setup for the non-spherical Rayleigh collapse of a vapor bubble near a rigid wall. The pressure of the surrounding, p_∞ , is set to 2, 5, and 10 MPa, which are values relevant to many high-pressure cavitation applications (Franc *et al.*, 2011), thus enabling us to investigate the effects of different driving pressures on the collapse dynamics. Due to the symmetry of the problem, we only simulate a quarter of the domain, with symmetric boundary conditions along the relevant planes. The wall is adiabatic and perfectly reflecting with no slip, and non-reflecting boundary conditions used along the remaining boundaries (Thompson, 1987). The parameter $\delta_o = H_o/R_o$, the normalized initial location of the bubble centroid with respect to the wall, defines the geometrical configuration of the problem; $\delta_o \geq 1$ represents initially spherical bubbles that are detached from the wall, while $\delta_o < 1$ describes bubbles initially attached to the wall. In the case of attached bubbles, the vapor is in contact with the wall surface. In practice, it is unclear whether a thin liquid film would cover the wall, and if so how thin it is. For simplicity, there

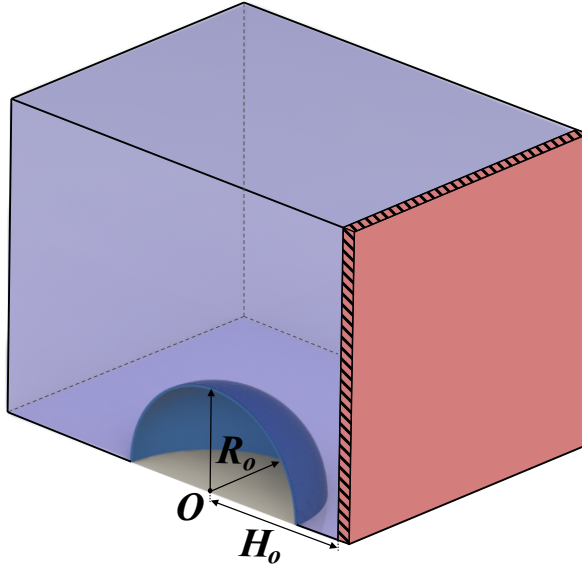


Figure 3.3: Schematic of the problem setup for Rayleigh collapse of a single vapor bubble near a rigid boundary.

is no liquid film in between the bubble and the wall; also for $\delta_o < 1$, the initial radius is set such that the bubble volume is the same as the detached cases, so that the initial collapse energy, $E_o = (p_\infty - p_o)V_o$, is the same for all cases. It is known that the sphericity of the bubble dynamics is affected by the presence of the wall. Therefore, to investigate the effects of the initial bubble stand-off on the collapse dynamics, the range of $0.5 \leq \delta_o \leq 5.0$ is considered. According to the preliminary observations, the initial stand-off distances greater than 5.0 show minor effects on the non-sphericity of the collapse. Similar to the previous case, a uniform Cartesian grid with 192 cells per initial bubble radius (approximately 1 billion cells in this case) is used to resolve the small scale features of the flow.

3.5.3 Rayleigh collapse of a vapor bubble pair near a rigid surface

In this problem, two bubbles with identical initial volume collapse in the vicinity of a rigid surface. The schematic of the problem setup is shown in Figure 3.4. The bubble, located at distance H_o from the wall, is referred to as the “primary bubble”. The non-dimensional parameter $\delta_o = H_o/R_o$ defines the initial proximity of the primary bubble to the wall. The “secondary bubble” is located at

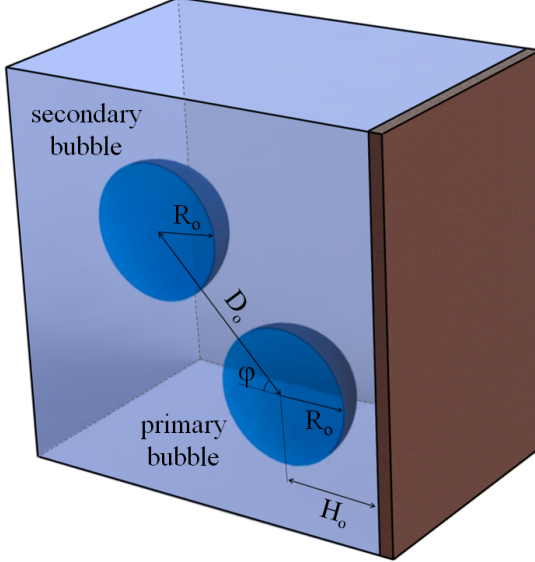


Figure 3.4: Schematic of the problem setup for Rayleigh collapse of a vapor bubble pair near a rigid surface.

distance D_o from the primary bubble, such that the non-dimensional parameter $\gamma_o = D_o/R_o$ sets the distance between the two bubbles, and the connecting line makes an angle ϕ with the horizontal. Thus, δ_o , γ_o , and ϕ are the geometrical variables, determining the bubbles' configuration at the beginning of the collapse. In this case, the surrounding pressure, p_∞ , is set to 5 MPa; as explained above, this value is relevant to many high-pressure cavitation applications. The problem has a plane of symmetry (the middle plane), so we simulate only half of the domain, with symmetric boundary condition along the corresponding plane. Similar to the previous cases, non-reflecting boundary conditions are applied along the remaining boundaries, except for the no-slip, adiabatic wall. To study the effects of the geometrical variables on bubble dynamics, the following spans are considered: $1.1 \leq \delta_o \leq 3.0$, $1.1 \leq \gamma_o \leq 3.0$, and $0^\circ \leq \phi \leq 90^\circ$. In this problem, the total number of computational cells varies between 1 to 2 billion, depending on the geometrical configuration of the bubbles; however, the resolution is set such that we have the same value of 192 cells per initial bubble radius for all cases.

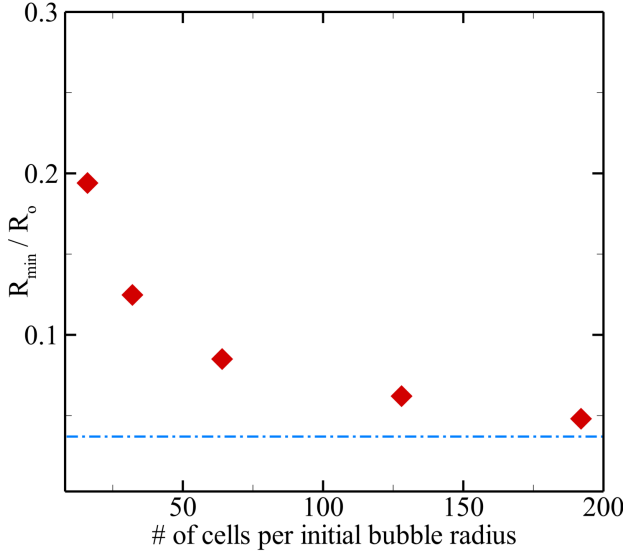


Figure 3.5: Convergence analysis of R_{min}/R_o for different number of cells per initial bubble radius. Blue dashed line: Keller-Miksis value.

3.5.4 Grid dependence

To assess the grid-dependence of the results, we simulate the spherical collapse of an isolated vapor bubble in a free field. Fig. 3.5 shows the convergence of the normalized minimum radius R_{min}/R_o for different number of cells per initial bubble radius. We further compare the numerical results with the minimum radius obtained from a Keller-Miksis calculation. The Keller-Miksis is an established model that has been extensively validated against various experiments in the literature ([Kröninger et al., 2010](#)). Although full convergence is not achieved, the resolution used for our simulations of non-spherical collapse is expected to be sufficient to resolve the detailed dynamics of the flow because non-spherical collapse does not lead to such a small volume. Thus, we expect the grid resolution to be sufficient to carry out a parametric study.

CHAPTER 4

Non-spherical collapse of a single bubble near a rigid wall

4.1 Abstract

To better understand damage mechanisms, this article examines the detailed dynamics of a single vapor bubble collapsing near a rigid boundary. Highly resolved three-dimensional numerical simulations are carried out to investigate non-spherical behavior of the bubbles, jet formation, and shock propagation throughout the collapse. A shock- and interface-capturing approach is used to accurately and efficiently solve the compressible Navier-Stokes equations for a multiphase system. The problem is set up as follows: a bubble, in pressure equilibrium with its surroundings, is located a distance δ_o from a rigid wall. The surrounding pressure is then instantaneously increased, thus driving the bubble to collapse. We alter the bubble configuration in a systematic fashion to study a wide spectrum of collapse morphology, from perfectly spherical to highly non-spherical, for different driving pressures. We further explain the re-entrant liquid jet formation, quantify the non-sphericity of the collapse, and discuss energy concentration and collapse intensity based on the non-sphericity parameter. Different shock waves emitted during the collapse, e.g. water-hammer shock and implosion shock, are characterized, the directionality of radially propagating shock waves is studied, and the subsequent pressure loadings along the wall are determined.

4.2 Spherical collapse

We first consider the collapse of an isolated vapor bubble in an infinite water as a baseline for comparison to the non-spherical case. Figure 4.1 shows six frames of the collapse process, with contours of pressure and density gradient magnitude, at different times. The initially spherical bubble collapses due to the pressure difference between the bubble and the surrounding liquid (Figure 4.1a). The surrounding pressure is $p_\infty = 5 \text{ MPa}$, and t_c is the theoretical collapse time calculated using the Rayleigh formula $t_c = 0.915R_o \sqrt{\rho_l/\Delta p}$, where $\Delta p = (p_\infty - p_o)$. This instantaneous pressure difference across the bubble interface gives rise to a Riemann problem leading to the propagation of a shock radially inward within the bubble, and a reflected rarefaction wave propagating radially outward within the liquid, which dramatically reduces the pressure around the bubble (Figure 4.1b). As a result, the bubble interface converging towards the centroid, which subsequently raises the liquid pressure surrounding the bubble, and leads to a violent compression of the bubble (Figures 4.1c & 4.1d). This implosion of the bubble and concentration of energy towards its centre generates a high pressure and temperature region when the bubble reaches its minimum volume (Figure 4.1e). Due to the high gas pressure, the bubble rebounds, thus releasing a compression wave that eventually steepens into a shock wave propagating outward in the liquid (Figure 4.1f).

In Figure 4.2, the normalized averaged bubble radius, $R/R_o = (V/V_o)^{1/3}$, and the pressure and temperature at the centre of the bubble are plotted in time, compared with the Keller-Miksis solution. The agreement with the Keller-Miksis solution is excellent, thus increasing our confidence in the accuracy of our numerical results. The Keller-Miksis is an established model that has been extensively validated against various experiments in the literature (Kröninger *et al.*, 2010). The results show the maximum bubble pressure of 18 GPa, and temperature of approximately 40,000 K at minimum radius. This short ($\sim 10 \text{ ns}$), high gas temperature may result in visible light emission from the collapsing bubble, or sonoluminescence (Barber & Putterman, 1991; Brenner *et al.*, 2002; Flannigan & Suslick, 2005, 2010; Duplat & Villermaux, 2015). The different driving pressure is

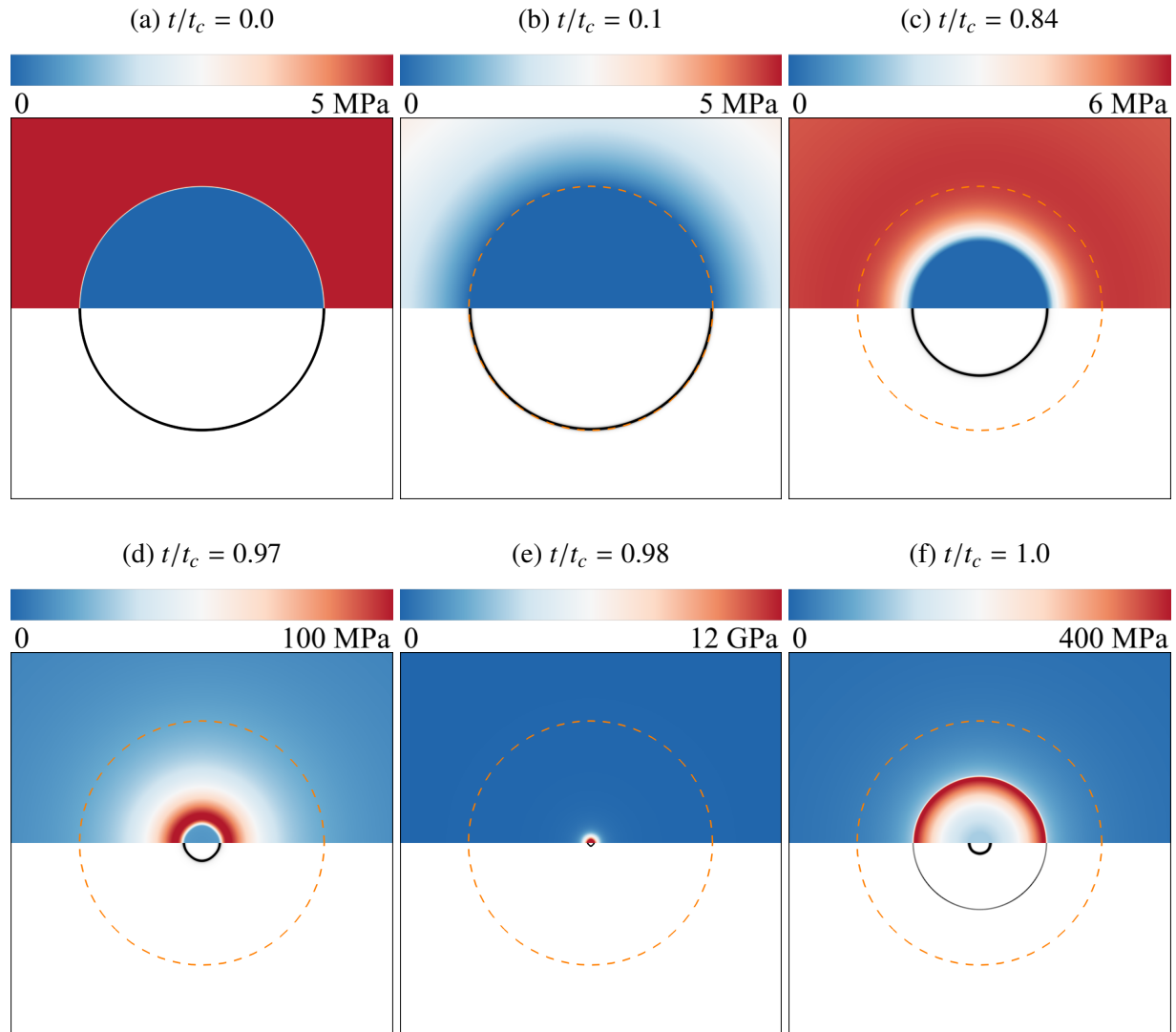


Figure 4.1: Collapse of an isolated bubble in an infinite medium, with $p_\infty = 5 \text{ MPa}$. Top: pressure contours; bottom: density gradient magnitude contours along the centreplane; dashed line: initial configuration of the bubble. Note: the pressure color bar is adjusted to emphasize the spatial distribution.

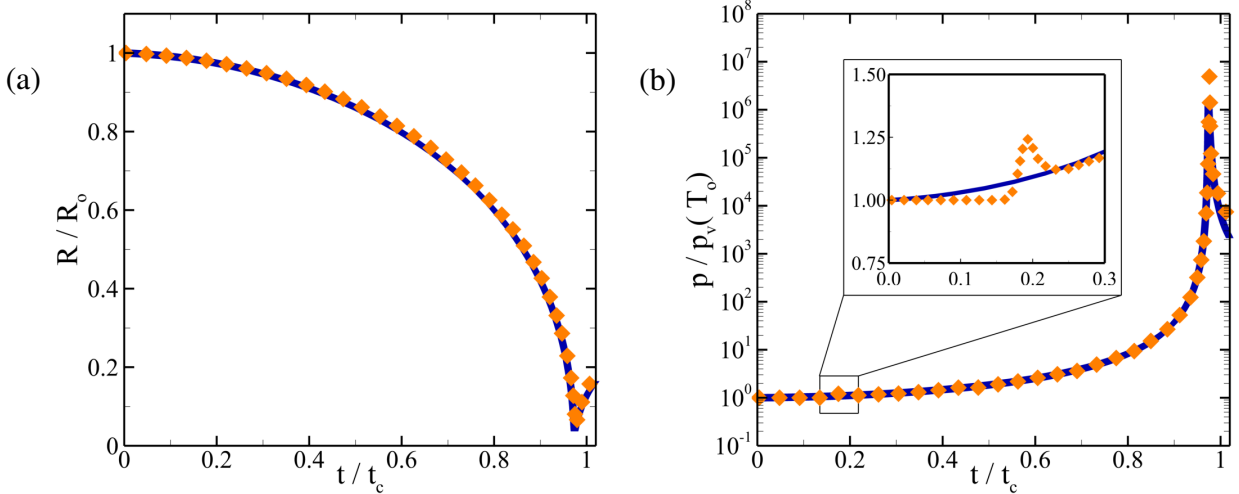


Figure 4.2: Time history of bubble radius (left) and pressure at the bubble centre (right). Blue solid line: Keller-Miksis solution; orange diamonds: numerical simulation.

one of the causes to explain the discrepancy between this temperature and the values reported by Flannigan & Suslick (2010). Also, non-equilibrium effects that can potentially influence the high temperatures at collapse are ignored in our simulations. A slightly larger rise of pressure at the collapse is observed in our simulations, compared to the Keller-Miksis solution. This difference is caused by the convergence of the initially transmitted shock inside the bubble. This process, which cannot be captured with a homobaric model such as Keller-Miksis, further increases the pressure and temperature at the bubble centre. This is better explained in the inset of Figure 4.2. The homobaric Keller-Miksis model predicts a continuous pressure increase as the collapse starts, yet the simulations show that the pressure at the bubble centre is unity until the transmitted shock converges at the centre. Then, the pressure decreases due to the divergence of the reflected blast, and starts to grow. However, since the transmitted shock bounces back and forth between the bubble wall and the centre, additional pressure spikes are observed every time the shock converges, until the collapse.

As observed in Figures 4.1a to 4.1b, the liquid pressure around the bubble initially decreases due to the propagation of the rarefaction wave, but eventually increases and even surpasses the pressure at infinity. The surrounding pressure is observed to continually rises up to 500 MPa right before the collapse. This phenomenon has been discussed in previous studies (Benjamin & Ellis,

1966; Franc & Michel, 2006; Johnsen & Colonius, 2009) and may be connected to jet formation in non-spherical collapse. We consider the one-dimensional momentum equation for a liquid in spherical coordinates:

$$\frac{\partial u}{\partial t} + u \frac{\partial u}{\partial r} = \frac{-1}{\rho_l} \frac{\partial p}{\partial r}, \quad (4.1)$$

in which $p(r, t)$ is the liquid pressure, ρ_l is the liquid density, assumed here to be constant, and $u(r, t)$ is the velocity component in the r direction, which owing to its divergence-free nature is given by $u(r, t) = \dot{R}(R^2/r^2)$, where $R(t)$ and $\dot{R}(t)$ are the bubble radius and bubble interface velocity, respectively. Integrating Eq. 4.1 with respect to r from an arbitrary point to infinity yields:

$$\frac{p(r, t) - p_\infty}{\rho} = (\ddot{R}R + 2\dot{R}^2) \frac{R}{r} - \frac{1}{2} \dot{R}^2 \frac{R^4}{r^4}. \quad (4.2)$$

At the bubble interface ($r = R$), assuming uniform pressure inside the bubble:

$$p_b = p(R, t) = p_v + p_{G_o} \left(\frac{R_o}{R} \right)^{3\gamma}, \quad (4.3)$$

where γ is the polytropic constant and p_{G_o} is the initial partial pressure of the gas. Eq. 4.1 evaluated at $r = R$ leads to the well-known Rayleigh-Plesset equation, neglecting surface tension and viscous effects:

$$\rho \left(\ddot{R}R + \frac{3}{2}\dot{R}^2 \right) = p_v - p_\infty + p_{G_o} \left(\frac{R_o}{R} \right)^{3\gamma}. \quad (4.4)$$

Integrating Eq. 4.4 in time results in:

$$\dot{R}^2 = \frac{2}{3} \frac{p_{G_o}}{\rho_l} \left[\frac{p_\infty - p_v}{p_{G_o}} \left(\frac{R_o^3}{R^3} - 1 \right) - \frac{1}{\gamma - 1} \left(\left(\frac{R_o}{R} \right)^{3\gamma} - \left(\frac{R_o}{R} \right)^3 \right) \right], \quad (4.5)$$

and

$$\dot{R} = \frac{p_{G_o}}{\rho_l R} \left[\frac{\gamma}{\gamma - 1} \left(\frac{R_o}{R} \right)^{3\gamma} - \left(\frac{p_\infty - p_v}{p_{G_o}} + \frac{1}{\gamma - 1} \right) \left(\frac{R_o}{R} \right)^3 \right]. \quad (4.6)$$

Additionally, by substituting the left-hand side of Eq. 4.4 into Eq. 4.2, and after appropriate ma-

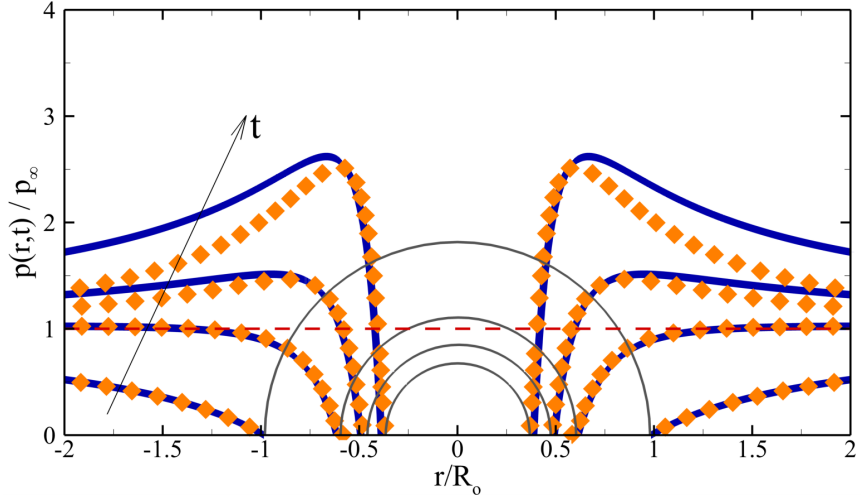


Figure 4.3: Liquid pressure versus distance at different instances ($R/R_o = 0.98, 0.61, 0.48, 0.37$). Blue solid line: Eq. 4.7; orange diamonds: numerical simulation; gray concentric circles: bubble configuration.

nipulations we obtain:

$$p(r, t) = p_\infty - \underbrace{\frac{1}{2}\rho_l u^2}_{(a)} - \underbrace{(p_\infty - p_b)\frac{R}{r}}_{(b)} + \underbrace{\left(\frac{1}{2}\rho_l \dot{R}^2\right)\frac{R}{r}}_{(c)}, \quad (4.7)$$

which is equivalent to the Bernoulli equation for unsteady potential flow:

$$p(r, t) = p_\infty - \rho_l \frac{\partial \phi}{\partial t} - \frac{1}{2}\rho_l u^2, \quad (4.8)$$

where $\phi(r, t) = -\dot{R}R^2/r$ is the velocity potential.

In Eq. 4.7, term (a) corresponds to the local dynamic pressure, term (b) shows the effects of the bubble pressure, and term (c) represents dynamic pressure of the liquid's added mass as the bubble volume changes. Term (a) always reduces the local, static pressure due to an increase in the local velocity. On the other hand, term (c) always increases the pressure. Term (b) is positive most of the time, and thus reduces the pressure; in the last stages of collapse, this term increases rapidly. The competition between these different terms regulates the liquid pressure distribution. Figure 4.3 shows the pressure as a function of distance at different times. As the bubble collapses, the volume

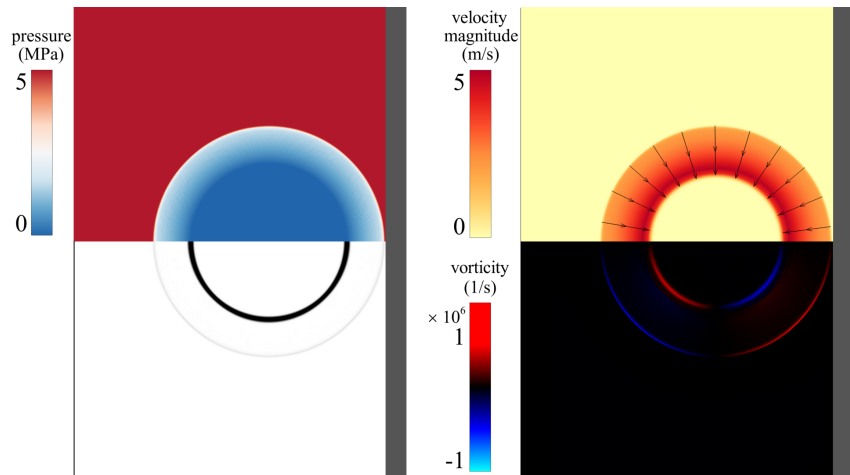
decreases, the interface velocity increases, and the three terms in Eq. 4.7 start to grow, yet with different rates. Initially, terms (a) and (b) are dominant, such that the liquid pressure decreases monotonically from infinity to the bubble interface. Later in time, when the bubble radius reaches a critical value $R_{cr} \approx 0.63R_o$ for a vapor bubble (Franc & Michel, 2006), term (c) dominates, and a pressure maximum is observed, which originates from the potential (incompressible) hydrodynamics, between the bubble interface and infinity. As the collapse progresses, the pressure maximum increases and moves closer to the bubble interface. The non-monotonic behavior of liquid pressure surrounding the bubble is also captured in high-speed shadowgraph visualization in the experiment of Supponen *et al.* (2017). We note that, for a given pressure drop, the local pressure in Eq. 4.7 can be written solely in terms of the position r and the bubble radius $R(t)$, along with its time derivatives. It thus follows that the local pressure maximum near the instant of collapse is not a cause but rather a consequence of the accelerating bubble interface (Johnsen & Colonius, 2009). Our simulations results in Figure 4.3 show a good agreement with the potential solution in Eq. 4.7 at early times, when the Mach number is low. Our results start to deviate from the potential solution in the last stages of collapse, when compressibility effects are no longer negligible. In particular, we observe steeper pressure profiles in our simulations.

4.3 Non-spherical bubble dynamics

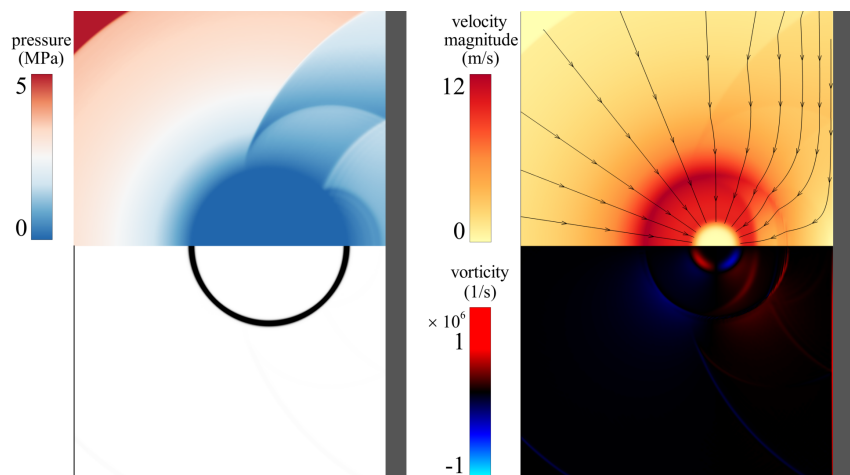
We now turn to the non-spherical bubble dynamics occurring in a collapse near a rigid surface, which is described by two dimensionless parameters: δ_o and p_∞/p_o . While a number of experimental and computational studies of this problem have been conducted in the past, the resolution of our simulations and our post-processing capabilities have enabled us to probe previously unattainable phenomena. We consider bubbles whose normalized initial stand-off distance is between 0.5 and 5.0, as well as driving pressures of 2, 5 and 10 MPa.

Figure (4.4) shows pressure, numerical schlieren, velocity magnitude (with streamlines) and vorticity contours for the collapse of a single bubble, initially located at $\delta_o = 1.5$ of a rigid wall.

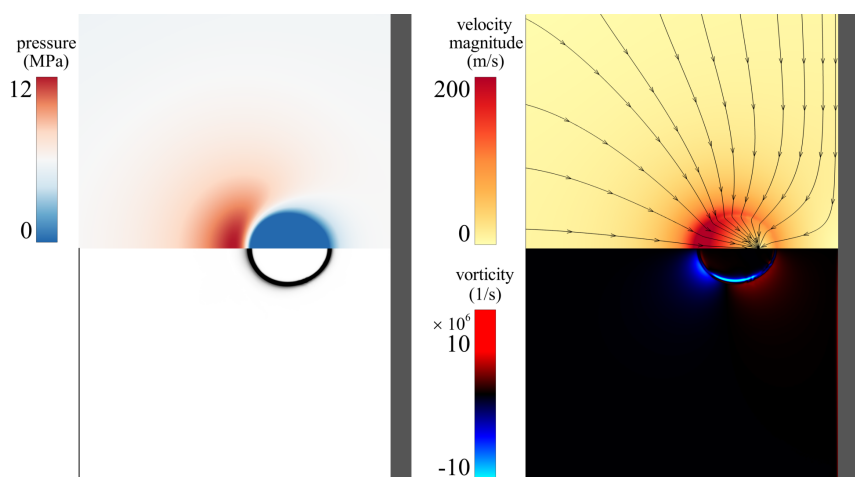
(a) $t/t_c = 0.03$



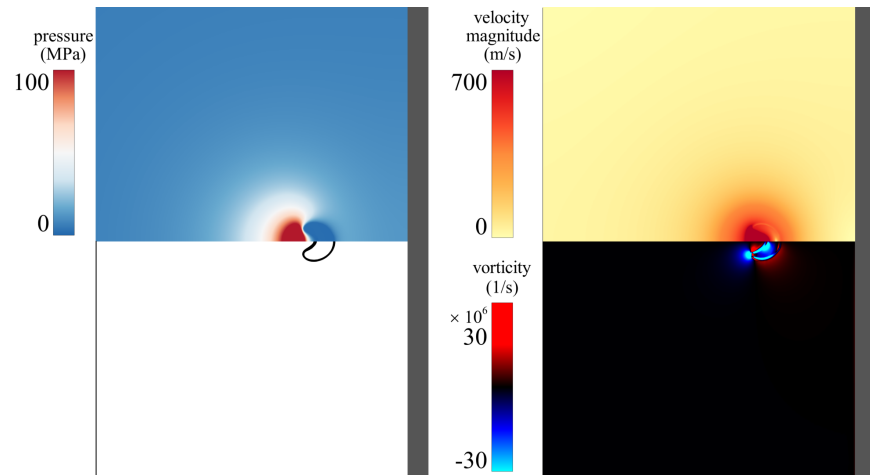
(b) $t/t_c = 0.12$



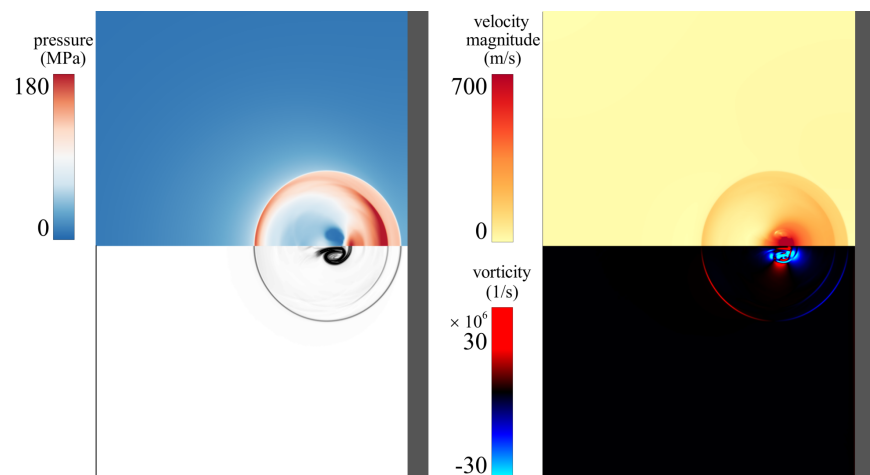
(c) $t/t_c = 0.98$



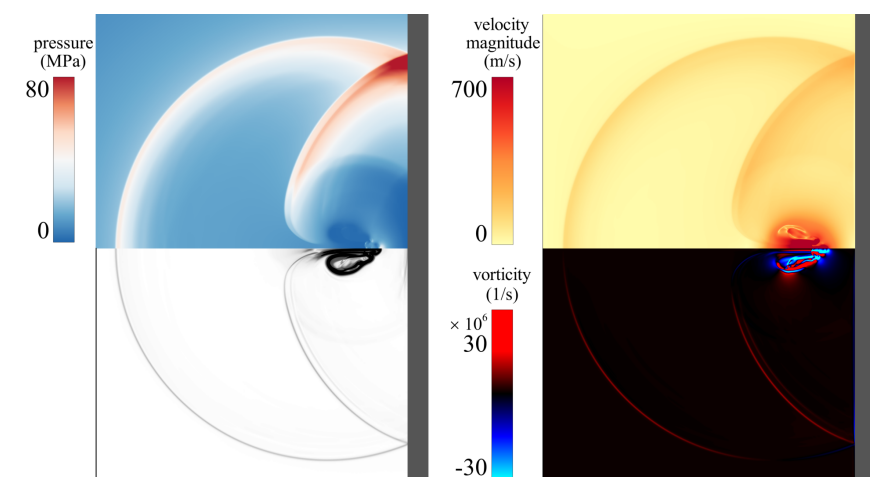
(d) $t/t_c = 1.06$



(e) $t/t_c = 1.12$



(f) $t/t_c = 1.20$



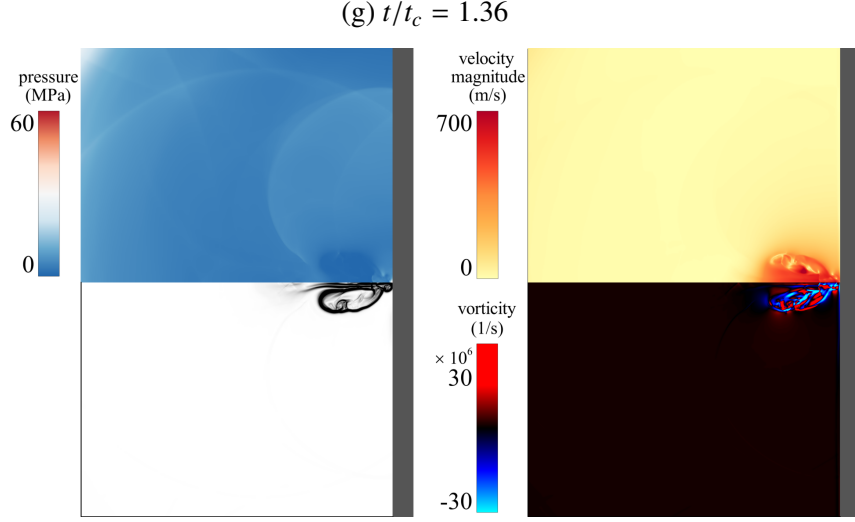


Figure 4.4: Non-spherical collapse of a single bubble near a rigid boundary with $p_\infty = 5$ MPa and $\delta_o = 1.5$. Top-left: pressure; bottom-left: numerical schlieren; top-right: velocity magnitude (with streamlines for the first three frames); bottom-right: vorticity. Note: the pressure color bar is adjusted to emphasize the spatial distribution.

As for the spherical case, a radial rarefaction wave propagates outward, while a transmitted shock wave converges towards the bubble center, as a result of Riemann problem driven by the discontinuous initial pressure distribution across the bubble interface (Figure 4.4a). However, the rarefaction wave impinges upon the neighboring wall and reflects back towards the bubble at time $t/t_c = 0.06$, thus communicating to the bubble the presence of the wall. Upon this interaction, the wave reflects back toward the wall as a compression wave, while a rarefaction is transmitted into the bubble. These reflections between the bubble interface and the rigid wall go on, thus forming the zigzag pattern of shock/rarefaction waves in the intermediate region (Figure 4.4b). Since these waves propagate radially, they affect the bubble non-uniformly, such that the bubble side closest to the wall is the most affected, while the distal side is the least affected. The non-uniform pressure distribution along the interface gives rise to a non-uniform local acceleration of the bubble interface (Figure 4.4c). The streamlines in Figures 4.4a to 4.4c, further illustrate how the velocity field evolves after the interactions between pressure waves and the bubble. In Figure 4.4c, the pressure in the liquid near the bubble exceeds the pressure at infinity. As explained in section 4.3, this phenomenon is a consequence of the accelerating bubble interface in a converging geometry.

A re-entrant, high-velocity liquid jet forms toward the wall and penetrates the bubble. High velocity/pressure region is observed behind the jet, as well as a region of high vorticity (Figure 4.4d). This high-velocity jet hits the opposite side of the bubble, thus leading to the formation of a water-hammer shock. A second shock is emitted when the bubble reaches its minimum volume, after the water hammer shock generation (Figure 4.4e). The time difference between these two shocks depends on the initial stand-off distance from the wall. The shock wave then hits the neighboring wall, reflects back onto the convoluted bubble, and eventually drives a secondary collapse (Figure 4.4f). The bubble then takes the form of a vortex ring convecting towards the rigid boundary. As it reaches the wall, the vortex ring drives a stagnation flow, which increases the wall pressure locally (Figure 4.4g). One can also distinguish the shock from the collapse of the vortex ring in the pressure contour of Figure 4.4g.

4.3.1 Jet formation

At this time, the detailed mechanism of the jet formation is a controversial question. The common viewpoint (Vogel *et al.*, 1989; Supponen *et al.*, 2016) postulates that the high pressure region (discernible in Figures 4.4c and 4.4d) behind the bubble pokes the upstream wall of the bubble and causing the jet to form. However, as observed in section 4.2, potential flow theory indicates that the converging flow produced by a spherically collapsing bubble gives rise to a pressure maximum between infinity and the bubble wall; as the bubble collapse beyond a critical size, the maximum pressure increases moves closer to the bubble wall. Although the analysis does not strictly hold for non-spherical collapse, one could consider this flow to consist of the superposition of a mean converging, spherical flow with a small perturbation (the jet) which moves at a slightly higher velocity. For this reason, one would expect the pressure just behind the jet to be higher than in the spherical case corresponding to the collapse of the opposite side. In fact, numerous of studies based on the potential flow theory also predict jet formation in the case of a single bubble collapsing near a rigid surface (Plesset & Chapman, 1971; Blake & Gibson, 1987). In their approach, the basic idea is to use the initial conditions (bubble pressure, bubble radius, bubble location with respect

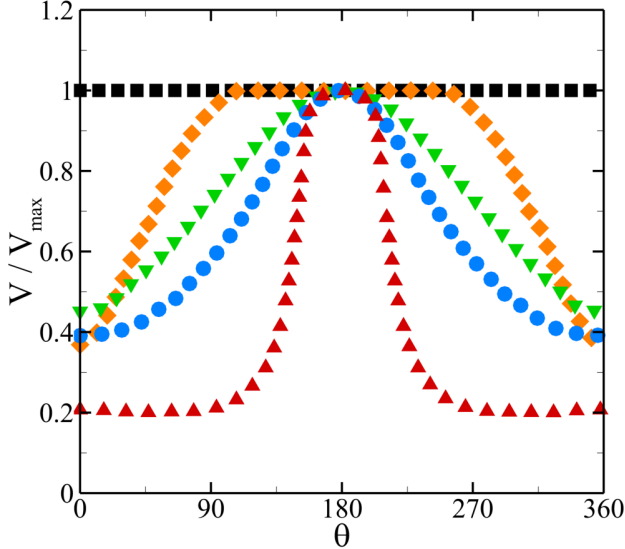


Figure 4.5: Normalized velocity magnitude of the bubble interface as a function of angle at different times $t/t_c = 0.03$ (black squares, $V_{max} = 4.4$ m/s), $t/t_c = 0.12$ (orange diamonds, $V_{max} = 10.5$ m/s), $t/t_c = 0.9$ (green gradients, $V_{max} = 133$ m/s), $t/t_c = 0.98$ (bubble circles, $V_{max} = 236$ m/s), $t/t_c = 1.06$ (red triangles, $V_{max} = 1047$ m/s); $\theta = 0$ corresponds to the bubble side furthest from the wall.

to the wall, and interface velocity at $t = 0$), as well as the boundary conditions at the wall (no velocity gradient normal to the wall) and at infinity (stationary flow at p_∞) to numerically solve for the velocity potential on interface of the bubble for a time step, which is later used to calculate the interfacial velocity. This velocity is then applied to update the velocity potential, as well as the bubble shape for next time step (Plesset & Chapman, 1971):

$$\mathbf{X}_j(t + \Delta t) = \mathbf{X}_j(t) + \mathbf{u}_j \Delta t, \quad (4.9a)$$

$$\phi_j(t + \Delta t) = \phi_j(t) + \left[(p_\infty - p_o)/\rho_l + \frac{1}{2} |\mathbf{u}_j|^2 \right] \Delta t, \quad (4.9b)$$

$$\mathbf{u} = \nabla \phi, \quad (4.9c)$$

where \mathbf{X}_j , \mathbf{u}_j , and ϕ_j are the position vector, velocity vector, and velocity potential of Lagrangian points along the bubble interface, respectively. For this elliptic problem for the velocity field, the solution (and thus the bubble shape) only depends on the initial and boundary conditions, not on the details of the flow in the interior domain.

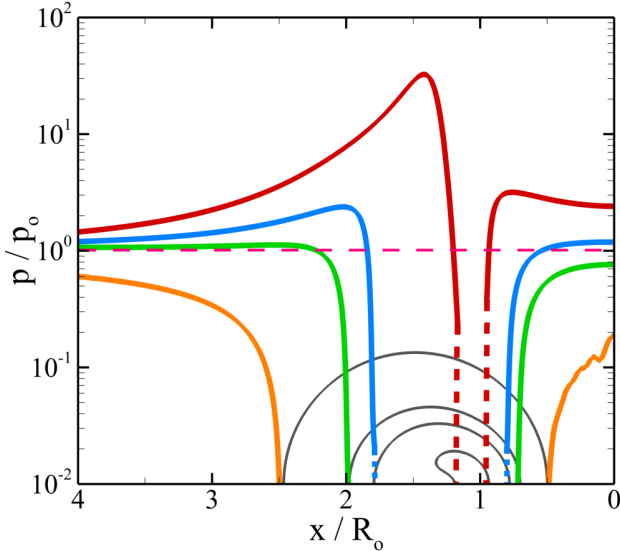


Figure 4.6: Normalized pressure distribution along the centerline at different instances. Orange: $t/t_c = 0.12$; green: $t/t_c = 0.9$; blue: $t/t_c = 0.98$; red: $t/t_c = 1.06$; gray lines: bubble configuration.

Accordingly, Figure 4.5 plots the velocity magnitude along the bubble wall normalized by the maximum velocity at that time. At early times ($t/t_c = 0.03$ corresponding to Figure 4.4a), the collapse is spherical, so the velocity is uniform along the bubble interface. Later on at $t/t_c = 0.12$ (Figure 4.4b), the interactions between reflected rarefaction/shock waves and the bubble break the symmetry of the collapse, which results in a non-uniform velocity distribution along the the bubble interface, with lowest speed a $\theta = 0$, i.e., nearest to the wall. Locations along the bubble interface with $90 \leq \theta \leq 270$ are still converging as if the collapse were spherical, with interface velocity equal to unity. Eventually, the velocity becomes entirely non-uniform, and the collapse is fully asymmetric with the maximum speed at the jet location and the minimum speed at the opposite side. As a result, the liquid pressure surrounding the bubble non-uniformly. The pressure distribution behind the jet along the centerline is plotted in Figure 4.6. Although the collapse is non-spherical, this plot is very similar to Figure 4.3.

4.3.2 Bubble morphology and collapse non-sphericity

As discussed in section 4.3, the proximity of a rigid boundary reduces the energy focusing, and gives rise to non-sphericity of the collapse. To illustrate this behavior, Figure 4.7 compares our

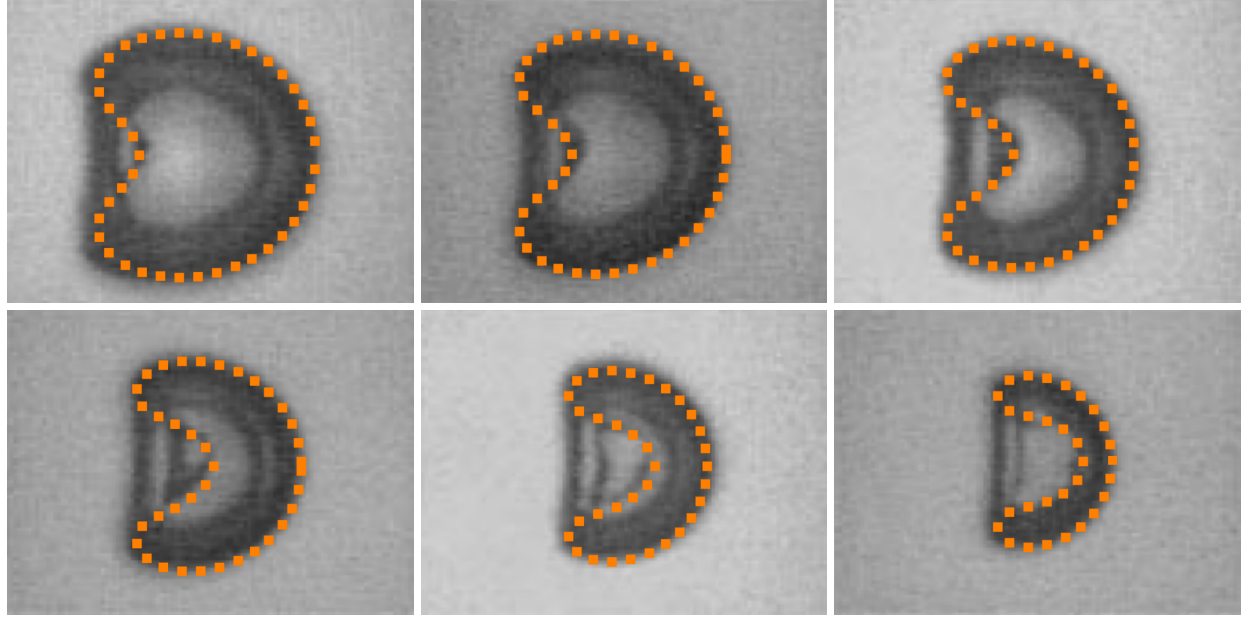


Figure 4.7: Bubble shape and jet formation, with $\delta_o = 1.6$ and $p_\infty = 0.1$ MPa in the experiment of Philipp & Lauterborn (1998), and $\delta_o = 1.5$ and $p_\infty = 5$ MPa in the simulations (orange squares). The normalized interframe time is $\Delta t = 1/t_c$.

numerical simulation against experiment performed by Philipp & Lauterborn (1998). Although the driving pressures are slightly different, the agreement between the experiments and simulations is very good after synchronizing in time based on the collapse time. However, it is known that the evolution of the bubble shape during the collapse depends on the initial bubble stand-off distance (Vogel *et al.*, 1989; Philipp & Lauterborn, 1998; Supponen *et al.*, 2016). In Figure 4.8, we show how the bubble shape deforms during collapse until jet impact, for different initial stand-off distances; a bubble that is fully attached to the wall ($\delta_o = 0.5$), a bubble that is barely touching the wall surface ($\delta_o = 0.9$), a bubble that is initially spherical and detached, but close to the wall ($\delta_o = 1.25$), and finally a bubble that is initially spherical and far from the wall ($\delta_o = 4.0$). The initial bubble volume is the same for all cases, which means that the radius of the equivalent sphere (shown by dashed orange line in Figure 4.8) is larger than R_o . Non-spherical collapse and formation of the re-entrant jet is observed for all cases. However, it can be seen that the collapse is more non-spherical and the jet starts to form earlier for $\delta_o = 0.9$ and 1.25, while in the case of $\delta_o = 0.5$ and 4.0 the jet can be identified only at the last stages of the collapse. This, in addition to the

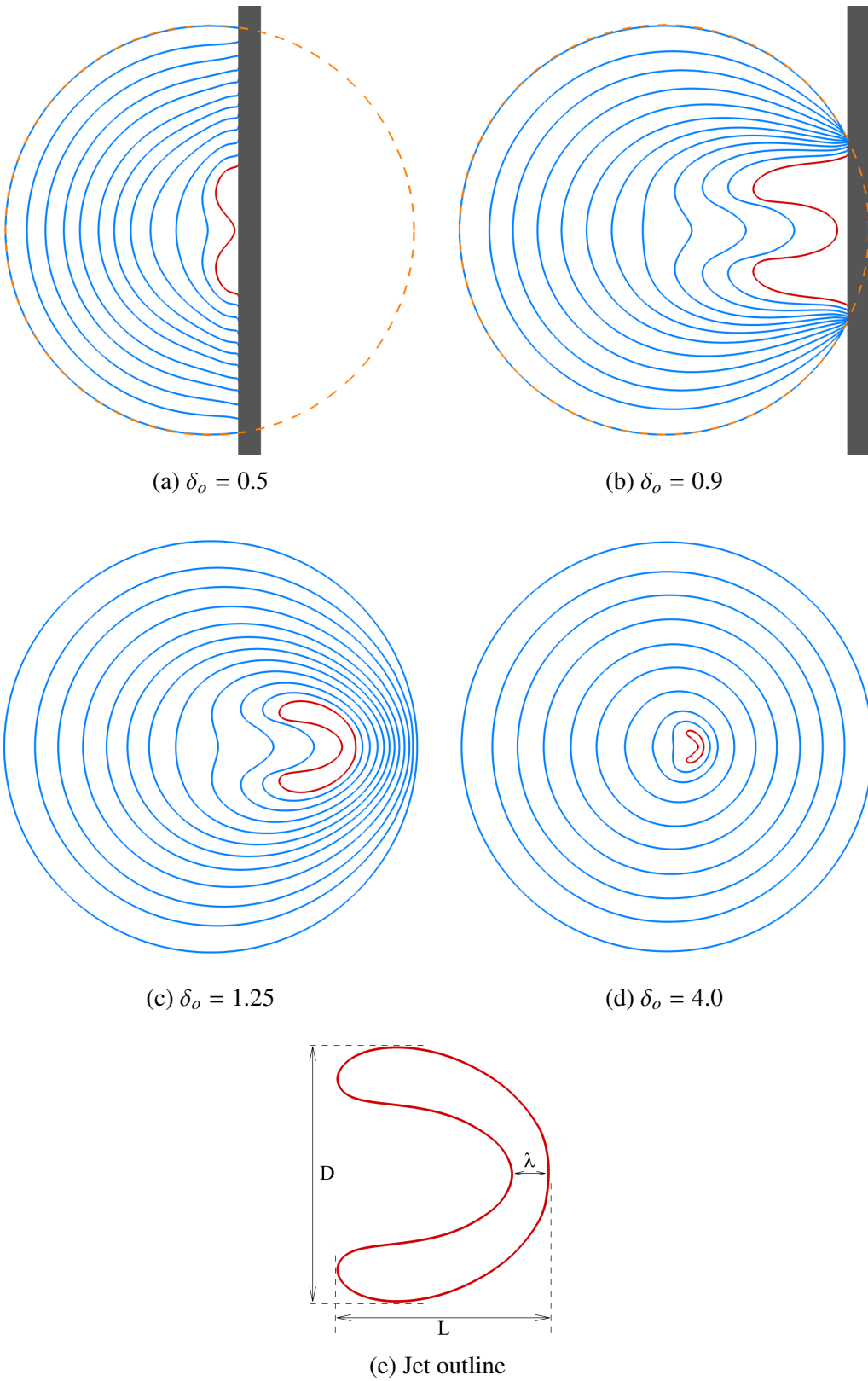


Figure 4.8: The evolution of the bubble shape throughout the collapse for different δ_o and $p_\infty = 5$ MPa (a) to (d); the jet layout and dimensions (e). The line corresponds to ($\alpha = 0.5$)

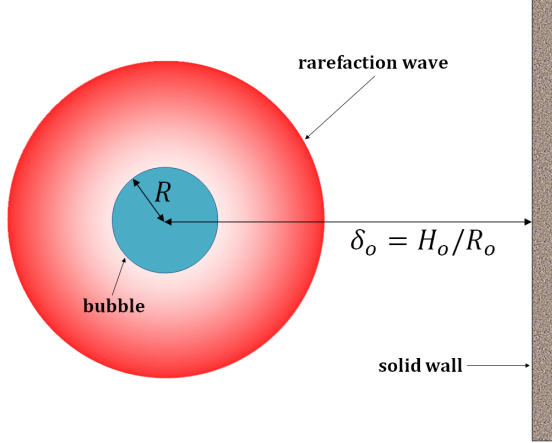


Figure 4.9: Schematic of the bubble collapse.

microscopic jet size, make the visualization of the jet near the instant of collapse a challenge in experiments, especially for large values of δ_o (Supponen *et al.*, 2016). Because we neglect capillary effects in this study, the dynamics of contact line for attached bubbles is not perfectly represented.

In our attempts to quantitatively describe the non-sphericity of the bubble collapse, we first seek to determine the values of δ for which the collapse is non-spherical. We observed in section 4.3 that the presence of the wall (and thus loss of symmetry) is communicated to the bubble by the initially released rarefaction wave traveling from the bubble interface to the wall and back to the bubble (Figure 4.9). For the driving pressures of interest, this wave's propagation speed is very close to the ambient speed of sound. Defining the distance between the bubble interface and the wall $d_1 = H_o - R_o$ and the distance between the wall and the bubble interface at collapse $d_2 = H_o - R_c$, it follows that

$$\frac{d_1 + d_2}{a_l} \leq t_c \quad \Rightarrow \quad 2\delta_{cr} - \left(1 + \frac{R_c}{R_o}\right) \leq \frac{t_c a_l}{R_o}, \quad (4.10)$$

where δ_{cr} is the non-dimensional initial bubble stand-off distance at which the first collapse becomes fully spherical. According to Rayleigh-Plesset analysis, we also have:

$$t_c = 0.915 R_o \sqrt{\frac{\rho_l}{p_\infty - p_v}}, \quad \frac{R_c}{R_o} = \left[\frac{1}{(\gamma - 1)} \frac{p_v}{p_\infty - p_v} \right]^{\frac{1}{3(\gamma-1)}}, \quad (4.11)$$

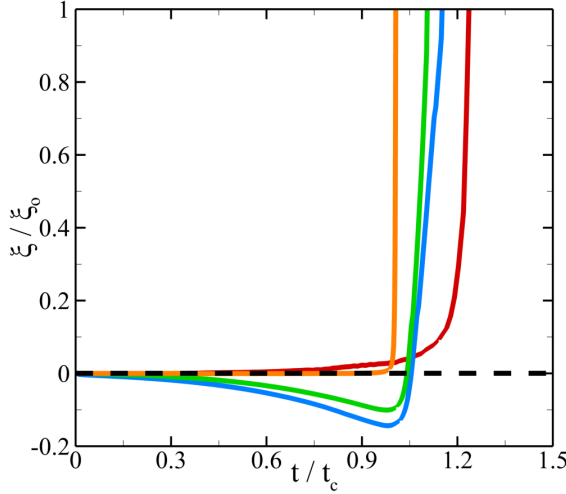


Figure 4.10: Non-sphericity as a function of time; red: $\delta_o = 0.5$; blue: $\delta_o = 0.9$; green: $\delta_o = 1.25$; orange: $\delta_o = 4.0$; black dashed line: spherical collapse.

where p_v is vapor pressure, ρ_l is the density of water and γ is the specific heats ratio. By substituting Eq. 4.11 into Eq. 4.10 we find the following relation for δ_{cr} :

$$\delta_{cr} \geq 0.5 + 0.46 \sqrt{\frac{\rho_l a_l^2}{p_\infty - p_v}} + 0.5 \left[\frac{p_v}{(\gamma - 1)(p_\infty - p_v)} \right]^{\frac{1}{3(\gamma-1)}}. \quad (4.12)$$

Given the surrounding pressure, p_∞ , and the pressure inside the bubble, p_v , one can estimate the critical stand-off distance at which the bubble starts to collapse spherically; for $p_\infty = 5$ MPa, $\delta_{cr} \approx 10.5$. This implies that the non-sphericity has a maximum in the intermediate region $\delta_o < \delta_{cr}$. Although there is no natural quantitative measure of non-sphericity, such a quantity could help explain the bubble's behavior during the collapse process. Examining Figure 4.8e where λ is the jet thickness, L is the bubble length, and D is the toroidal bubble diameter, we define a measure of non-sphericity $\xi = 1 - \pi\lambda/\mathcal{P}$, where \mathcal{P} is the perimeter of the toroidal bubble in the centerplane. For spherical collapse ξ is zero; we also note that $\lambda = L$ before jet formation. Another useful parameter is $\eta = L/D$ which defines the aspect ratio of the jet. For detached bubbles, the collapse starts spherically, so $\xi_o = 0$. In contrast, the attached cases contain bubbles with the initial form of a spherical cap, so $\xi_o \neq 0$; therefore, to exclude the effects of initial non-sphericity for these cases, we use ξ_o to normalize the reported value of non-sphericity from numerical simulations.

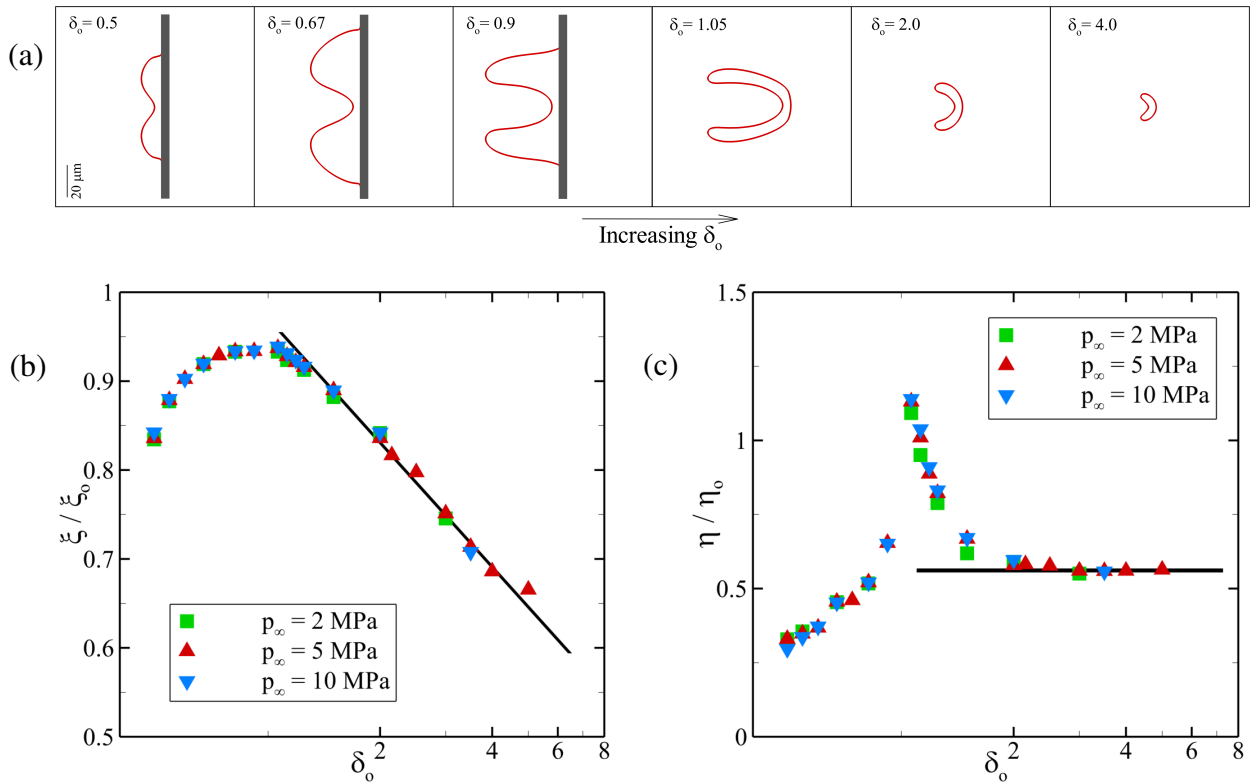


Figure 4.11: Collapse non-sphericity for varying initial stand-off distances. Morphology before the impact (top); non-sphericity (bottom left), and jet aspect ratio (bottom right).

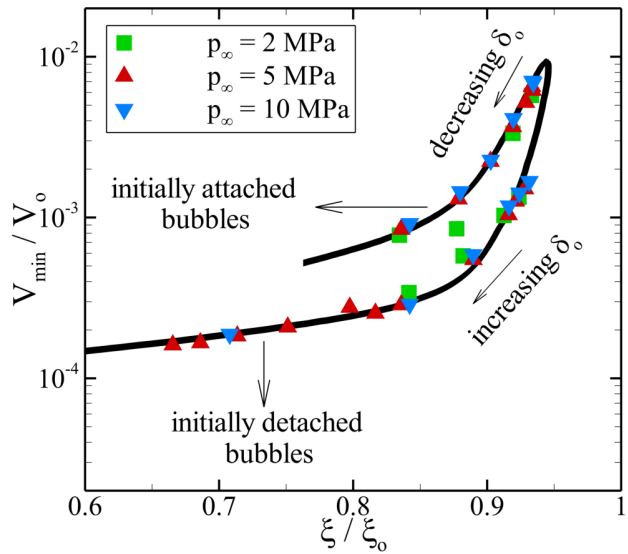


Figure 4.12: Normalized minimum volume (collapse intensity) as a function of non-sphericity for different driving pressure.

Figure 4.10 shows the bubble non-sphericity as a function of time until the jet impact ($\xi = 1$) for the cases shown in Figure 4.8. It can be seen that for $\delta_o = 0.5$ and 4.0 the value of non-sphericity stays close to the zero for a relatively long time throughout the collapse; this implies that the collapse, up to the very last stages, remains mainly spherical. For δ_o close to 1 , the non-sphericity initially goes negative before the impact, meaning that the bubble initially becomes egg-shaped before the jet develops (Figure 4.8c). This figure also illustrates that the jet impact time (when $\xi = 1$) decreases with increasing initial stand-off, consistent with previous studies (Philipp & Lauterborn, 1998; Supponen *et al.*, 2016). The non-spherical behavior of the collapse is strongly depends on the initial stand-off. To quantitatively assess this effect and compare the non-spherical behavior of different cases, we measure the non-sphericity when the jet reaches a certain thickness right before the impact ($\lambda/R_o = 0.05$). Subsequently, Figure 4.11 plots the non-sphericity and jet aspect ratio as a function of δ_o . We find that non-sphericity increases initially as the stand-off is increased from 0.5 to 1 , implying that the collapse becomes more non-spherical. The maximum non-sphericity is observed at $\delta_o = 1$, and linearly decreases afterwards, as the bubble starts farther from the wall. This value becomes zero at δ_{cr} , where the bubble does not feel the presence of the wall anymore and starts to collapse spherically. Furthermore, the jet aspect ratio starts from the minimum value of $\eta/\eta_o \approx 0.3$ with relatively low non-sphericity and a short jet compared to the deformed bubble diameter; $\eta/\eta_o \approx 1.15$ is achieved at maximum non-sphericity, denoting a long jet; for bubbles far away from the wall, the aspect ratio converges to the value of $\eta/\eta_o \approx 0.55$. In summary, for small δ_o , the jet is fat and short; as δ_o is increased, the jet becomes thinner and longer, reaching a maximum length at $\eta/\eta_o = 1$. For greater values of δ_o , the jet becomes less pronounced and the collapse more spherical. These results explain why experimental observations of non-spherical collapse can be made in a more straightforward fashion for bubbles initially close to the wall.

A spherical collapse concentrates energy into a small volume at the center of the bubble, thus creating high pressures and temperatures. The proximity of a neighboring rigid boundary breaks the symmetry of the collapse, and hinders the energy concentration. Spherical collapses produce

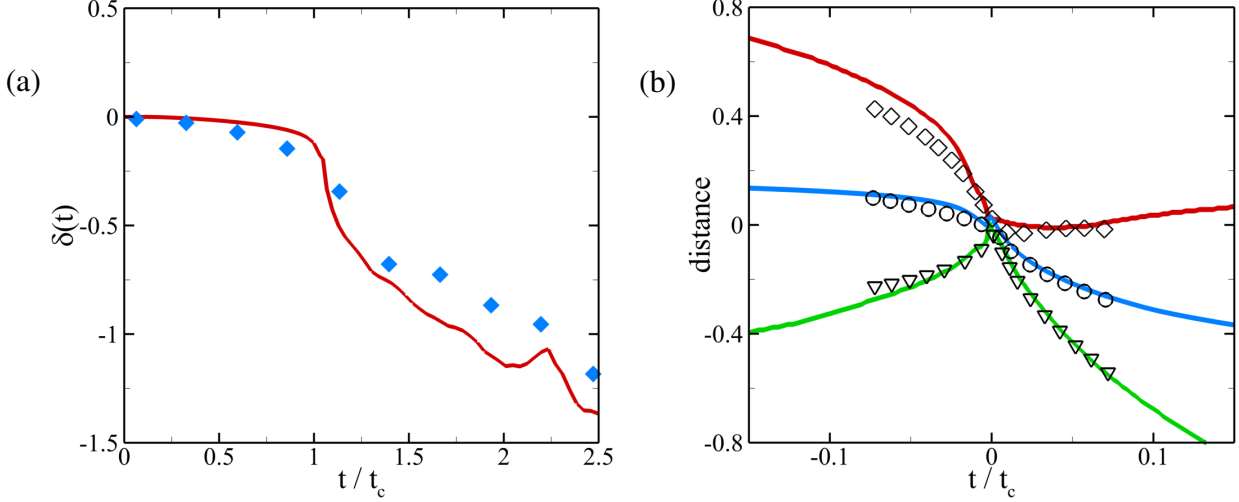


Figure 4.13: Left: bubble centroid location as a function of time for $\delta_o = 2.15$; red solid line: simulation; blue diamonds: experiment by [Vogel et al. \(1989\)](#). Right: bubble upper wall (red), bubble lower wall (green), and bubble centroid (blue) as a function of time for $\delta_o = 2.5$; solid lines: simulation, empty symbols: experiment by [Vogel et al. \(1989\)](#)

the highest pressures and temperatures, and most energetic shocks ([Vogel et al., 1989](#); [Supponen et al., 2017](#)), while the energy defocussing and the increase in the kinetic energy of non-converging motions in non-spherical cases lead to a less intense collapse, with lower pressures and temperature. The point of convergence moves away from the bubble centroid towards the wall (in the jet direction) as observed in Figure 4.4c. Considering the normalized minimum volume of the bubble, V_{min}/V_o , to exemplify the collapse intensity (the lower the volume ratio, the stronger the collapse), Figure 4.12 demonstrates how non-sphericity affects the collapse intensity. The non-uniform velocity field due to the presence of the neighboring wall results into a non-zero momentum of the fluid, first quantified by [Blake & Gibson \(1987\)](#) using the Kelvin impulse analysis ([Benjamin & Ellis, 1966](#)) in an incompressible, irrotational flow. This behavior leads to the migration of the bubble towards the wall, observed in numerous studies. In the case of spherical collapse, the Kelvin impulse is zero, and subsequently the bubble migration does not take place. In figure 4.13, we compare the motion of the bubble tracked in our simulations to the experimental results of [Vogel et al. \(1989\)](#), which shows a good agreement. Bubble migration is another clearly observable quantity representative of non-sphericity and energy defocussing. The amount of bubble displacement until the collapse ($\Delta x/R_o$), and more specifically the bubble centroid location at collapse

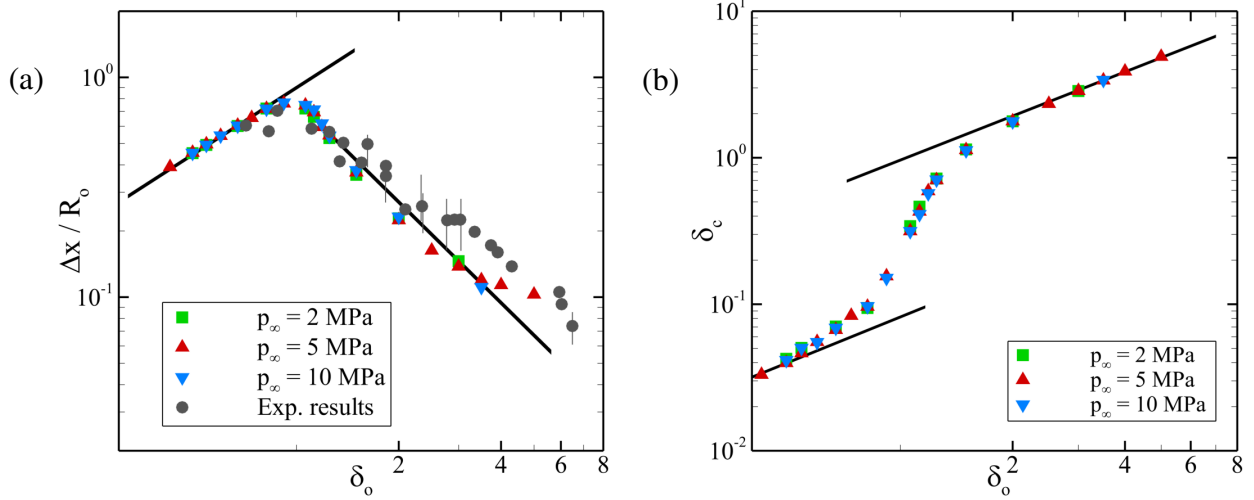


Figure 4.14: Bubble displacement (left), and centroid location at collapse as a function of initial stand-off for different driving pressures; gray diamonds represents the experiments by [Supponen et al. \(2016\)](#).

$(\delta_c = \delta_o - \Delta x/R_o)$ are of importance when quantifying impact load on the wall surface, as discussed in section 4.4. Figure 4.14 shows the bubble displacement, as well as the centroid location at collapse as a function of initial bubble stand-off distance; we further compare the displacement values from our simulations to the experimental results for the collapse of a single bubble near rigid/free surfaces performed by [Supponen et al. \(2016\)](#). [Beig et al. \(2018\)](#) discuss how $\Delta x/R_o$ and δ_c scales with initial bubble stand-off and show that for initially attached bubble both $\Delta x/R_o$ and δ_c scales as δ_o , while for the detached bubbles starting far from the wall ($\delta_o \gg 1$) the displacement scales as $\delta_o^{-4/3}$ and $\delta_c \approx \delta_o$; these scalings are shown in the black solid lines in Figure 4.14.

4.3.3 Jet velocity

Since the water hammer shock produced by the jet impact upon the distal side depends on the jet speed, we examine here the maximum jet speed. It is shown that, except for attached bubbles, the lower wall of the bubble accelerates away from the wall (left plot in figure 4.13). In this section, we study the effects of the initial stand-off distance (non-sphericity), and driving pressure on the velocity of the jet (V_{jet}), and the lower bubble wall (V_{distal}). Following [Supponen et al. \(2016\)](#), we use the characteristic speed $\sqrt{\Delta p/\rho_l}$ defined by [Plessel & Chapman \(1971\)](#) to non-dimensionalize

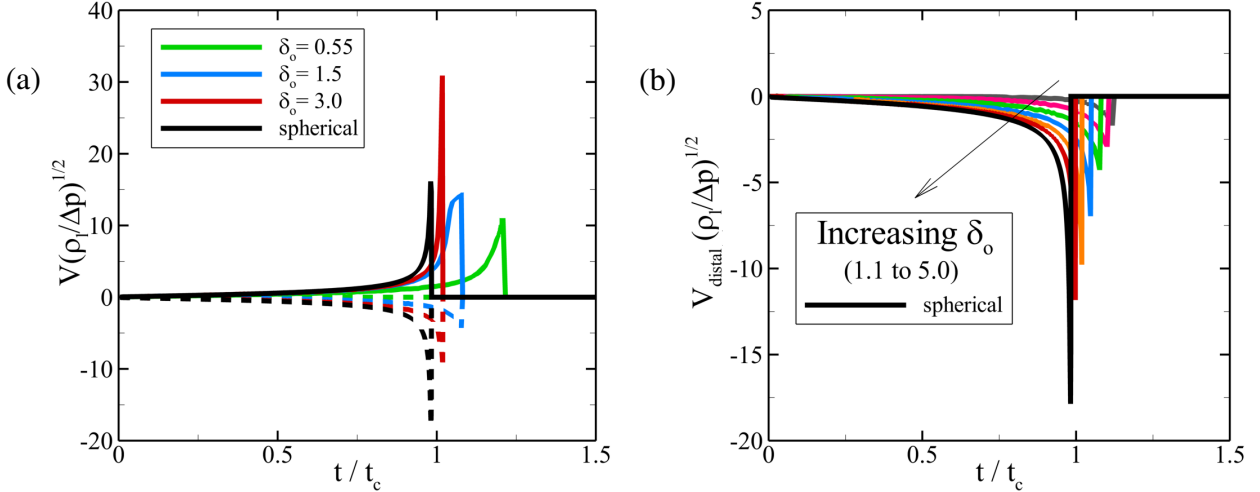


Figure 4.15: (a) Time evolution of the jet (solid lines) and distal (dashed lines) velocity for three different stand-off distances at $p_\infty = 5$ MPa. (b) The effects of initial bubble stand-off on distal velocity for $p_\infty = 5$ MPa.

the relevant velocities.

Figure 4.15a plots V_{jet} and V_{distal} as function time for three different values of δ_o : an initially attached bubble ($\delta_o = 0.55$), a detached bubble but relatively close to the wall ($\delta_o = 1.5$), and a detached bubble far away from the wall ($\delta_o = 3.0$). The velocities are shown up until the impact time and are compared to the spherical case, where the velocities are reported until the bubble rebound. According to the results, the maximum jet velocity increases from 750 m/s to 2500 m/s as δ goes from 0.55 to 3.0; the maximum interface velocity in the case of spherical collapse is 1300 m/s. At the same time, the velocity of the distal side (closest to the wall) increases as the bubble starts initially farther from the wall, eventually tending to a spherical collapse; for attached bubbles, the velocity of the distal side is zero.

We plot maximum jet velocity as function of initial stand-off distance in Figure 4.16a; normalizing by the characteristic speed $\sqrt{\Delta p/\rho_l}$ collapses the data for different driving pressures. Supponen *et al.* (2016) show that when the bubble is initially far from the wall, the maximum jet velocity scales as δ_o^2 , which is indicated by the back solid line in the figure. To assess the effects of non-sphericity on jet velocity, we plot the non-dimensional V_{jet} as a function of non-sphericity in Figure 4.16b. The results show that the jet velocity linearly decreases with increasing

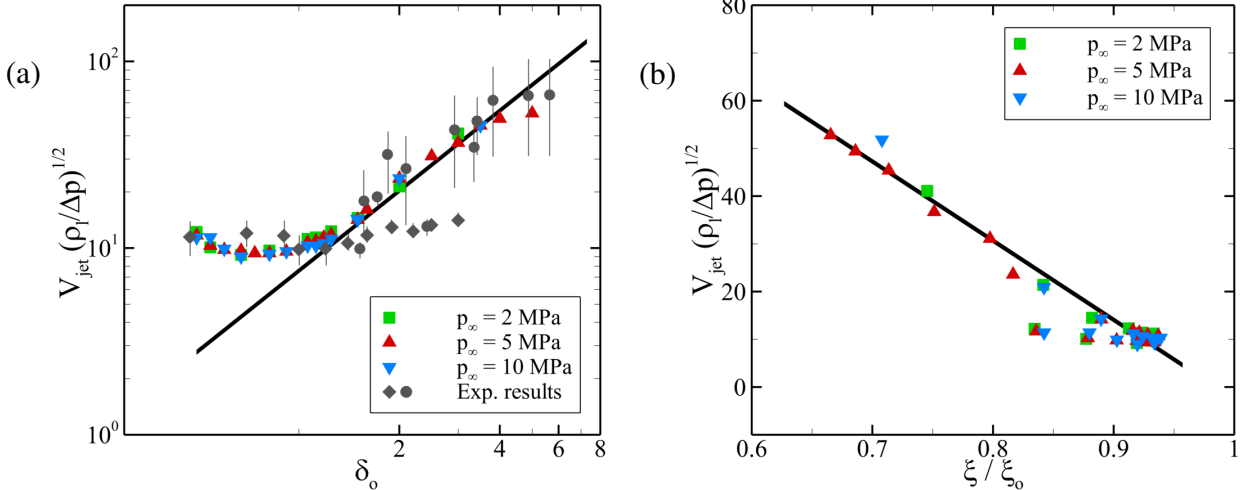


Figure 4.16: (a) Maximum jet velocity vs. initial bubble stand off for different driving pressures; gray diamonds: experiments of Philipp & Lauterborn (1998) and Brujan *et al.* (2002); gray circles: experiments of Supponen *et al.* (2016). (b) Maximum jet velocity as a function of non-sphericity for different driving pressures.

non-sphericity. We further compare the maximum jet velocity from numerical simulations against selected data from experiments (Figure 4.16a). The simulations agree with the recent experiments of Supponen *et al.* (2016) near rigid/free surfaces (gray circles, with anisotropy parameter less than 0.1), which benefit from improved technology compared to older experiments. Although the agreement with the experiments of Philipp & Lauterborn (1998) and Brujan *et al.* (2002) near a rigid surface (gray diamonds) are acceptable for $\delta_o < 2$, significant discrepancies are observed for $\delta_o > 2$; in fact the agreement is good only in the region with high non-sphericity, where the jet is the most visible (described in § 4.3.2), while the region where the jet is short-lived and small in size leads to the deviations between the simulations and experiments. Some possible causes for these discrepancies include insufficient temporal and spatial resolution of high-speed imaging, as well as a lacking transparency of the bubble interface in the images.

4.4 Jet impact, bubble collapse, and shock propagation due to non-spherical bubble collapse

One of the most important outcomes of bubbles inertially and repeatedly collapsing near a solid object is the damage they produce. There has been debate as to which of two damage-inducing mechanisms is dominant: direct impact of the jet onto the surface, or impingement of the shock produced by the bubble reaching its minimum volume (Tomita & Shima, 1986). While both events are likely to occur and be important, we offer here a strategy to distinguish between the two. In our simulations, we can measure the time difference between the jet impact, responsible for the water-hammer shock, and the instant the bubble reaches its minimum volume, thus leading to shock formation from the rebound ($\Delta t_{imp} = t_{collapse} - t_{impact}$); this value is further normalized by the collapse time, and is compared to experimental data of Supponen *et al.* (2016) and Philipp & Lauterborn (1998) in Figure 4.17. Overall good agreement with the experimental results is achieved. One observation is that dependence of the normalized time difference on the initial stand-off distance is similar to that of the non-sphericity; a maximum is achieved at an initial stand-off close to unity where the highest non-sphericity is observed, and both increasing and decreasing the stand-off distance lead to lower values for the normalized time difference. It can be seen that the reported value of the parameter $\Delta t_{imp}/t_{collapse}$ is always greater than zero, meaning that for all cases, the jet impact happens prior to the collapse. This time lag between the two events results in the formation of different shocks with different morphologies, discussed below.

A qualitative depiction of these two mechanisms is shown in Figure 4.18, where the bubble is initially located at $\delta_o = 2.5$. Once the jet hits the distal side and pierces the bubble, it creates the water-hammer shock at the point of jet impact (frame 1). This shock which eventually interacts with the bubble and subsequently drives the collapse of the torus off the centerline. The bubble thus reaches its the minimum volume, rebounds, and forms a second shock wave that propagates radially and intersects along the centerline, thereby creating a high pressure region (frame 2). This second shock wave immediately follows the water-hammer shock with a relatively higher speed

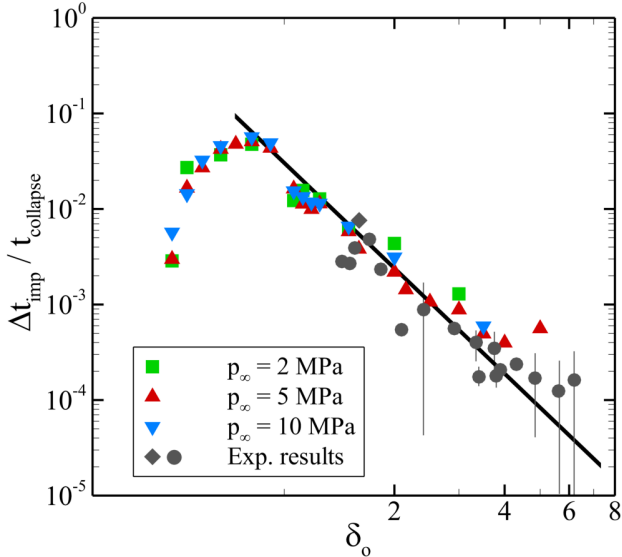


Figure 4.17: Normalized time difference between the jet impact and collapse as a function of initial stand-off distance for different driving pressure; gray diamonds: experiments of Philipp & Lauterborn (1998); gray circles: experiments of Supponen *et al.* (2016).

(frame 3) and eventually merges with it to form a single radially propagating shock wave (frame 4). The timing strongly depends on the initial stand-off distance. For bubbles initially far from the wall ($\delta_o \gtrsim 2.0$), the two shock waves merge into a single wave before impinging upon the wall; in fact, for $\delta_o \geq 4.0$, the two events are nearly indistinguishable. For bubble initially closer to the wall ($\delta_o \lesssim 2.0$), the shock wave generation sequence is more complicated.

To further explain this process, Figure 4.19 shows contours of pressure and density gradient magnitude for three different initial bubble stand-off distances throughout the collapse. According to Figure 4.19a, for the bubble attached to the wall ($\delta_o = 0.8$), the jet piercing the bubble hits the solid surface directly, which raises the pressure along the wall, and leads to the formation of the water-hammer shock. This shock wave later interacts with the convoluted interface of the toroidal bubble and drives a second jet within the bubble ring attached to the wall. The second jet accelerates towards the torus, outer wall, hits the distal side, and ultimately splits the toroidal bubble into two. This results in a second less energetic water-hammer shock. The bubble eventually collapses, emits a shock wave, and raises the pressure and temperature along the wall (Beig *et al.*, 2018). The interactions between the first and second water-hammer shocks, the toroidal bubble,

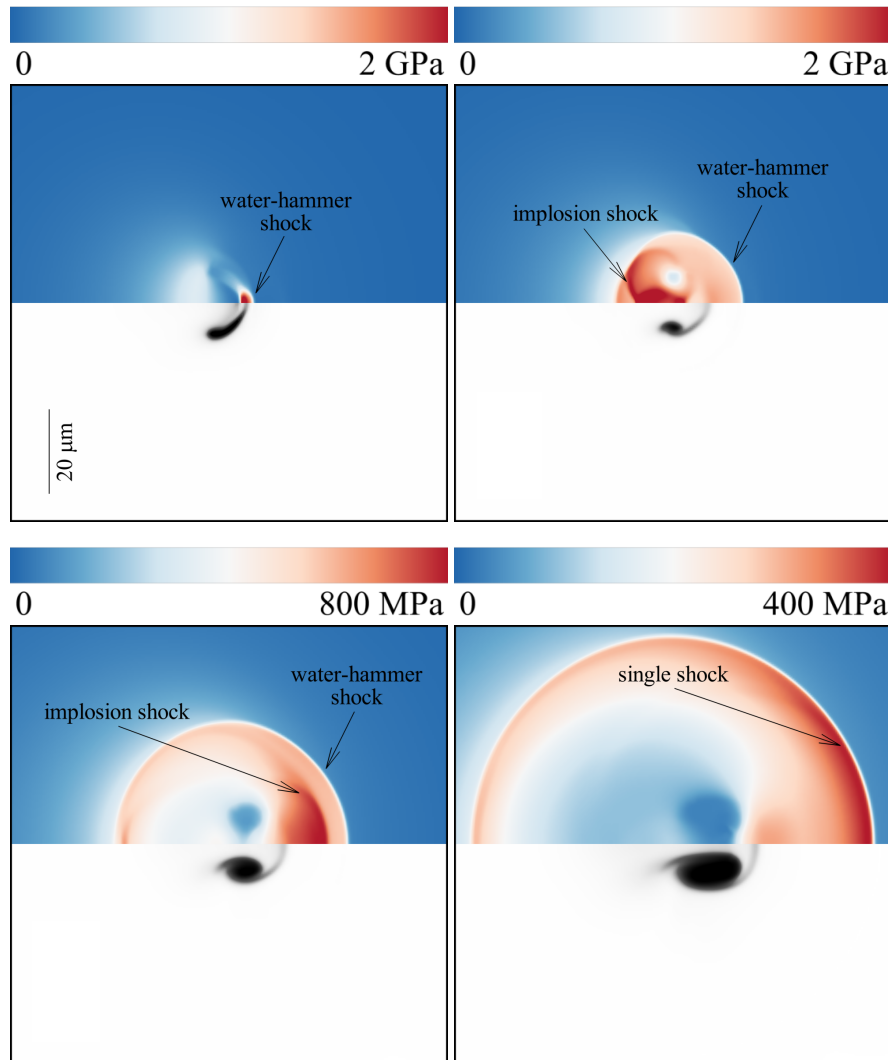


Figure 4.18: Formation of different shock waves during the collapse of a single bubble near a rigid surface, with $\delta_o = 2.5$ and $p_\infty = 5 \text{ MPa}$. top: pressure contours; bottom: contours of volume fraction.

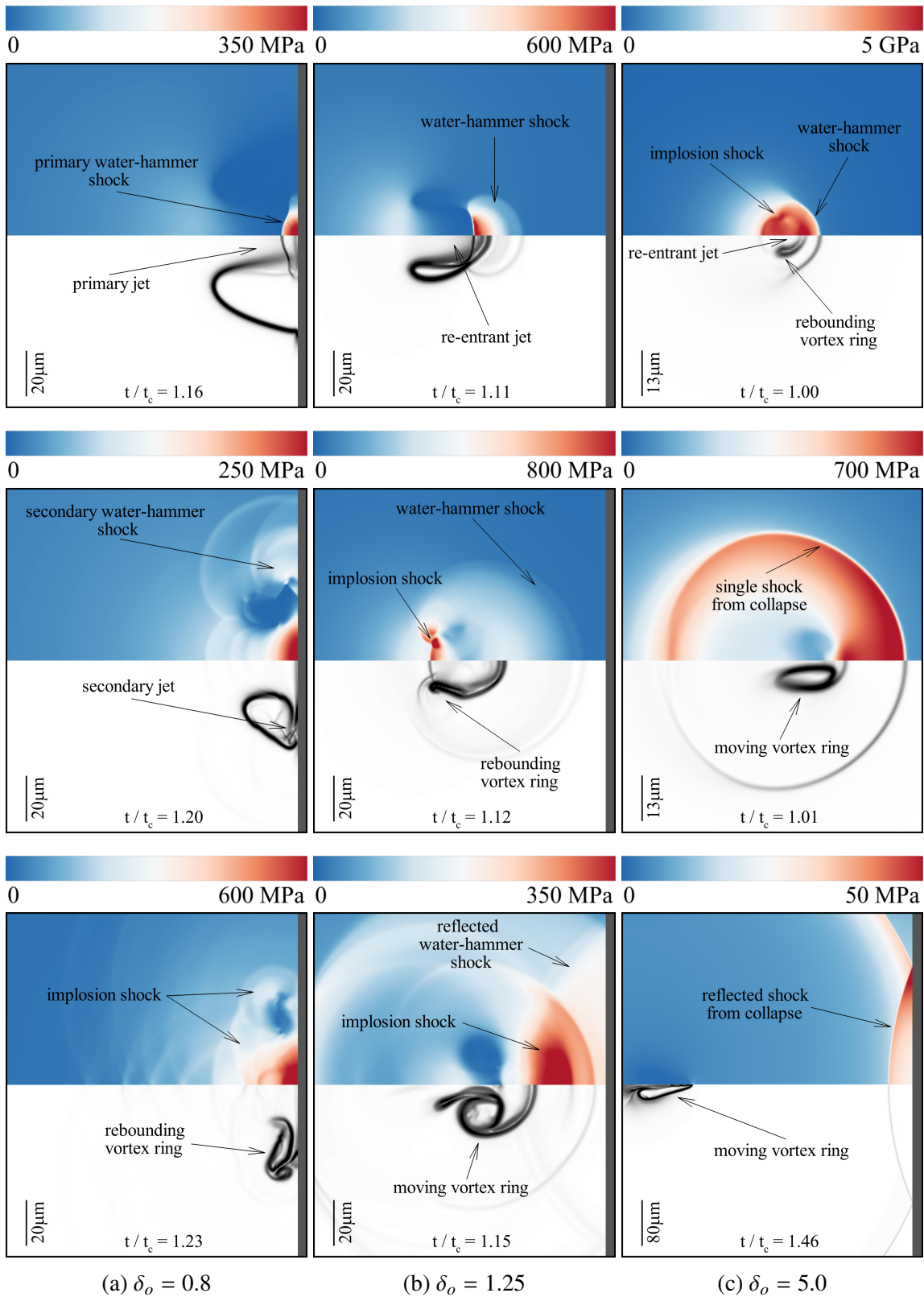


Figure 4.19: Jet impact and shock propagation for different initial bubble stand-off distances, with $p_\infty = 5 \text{ MPa}$.

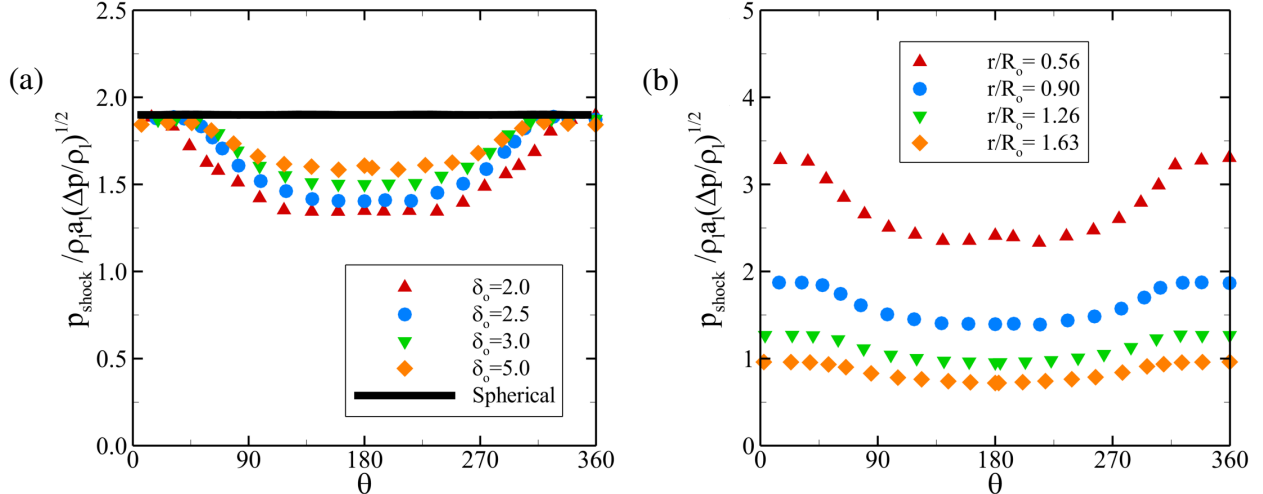


Figure 4.20: (a) Shock pressure as a function of angle at $r/R_o = 0.9$ for different initial bubble stand-off with $p_\infty = 5$ MPa; r defines the distance from the shock origin (b) Shock pressure as a function of angle at $\delta_o = 2.5$ for different radial distances from the shock origin with $p_\infty = 5$ MPa.

the implosion shock, and the rigid boundary not only constitute complex wave patterns, but also create a high pressure region along the wall. For detached bubbles relatively close to the wall (e.g., $\delta_o = 1.25$), the shock produced by the water hammer clearly impinges upon the wall before that implosion shock. As a result, the wall pressure exhibits two peaks, corresponding to shock impingement from both of these events. The pressures at the instant of the collapse are significantly higher than previous cases, which is due to the fact that collapse is more spherical at this initial stand-off distance, which leads to a more intense collapse (discussed in § 4.3.2). Although the collapse becomes stronger and happens earlier in time, the shock wave hits the wall surface the latest; it needs to travel a longer distance to reach the boundary.

The numerical simulations show that for $\delta_o \geq 2.0$ the merging of the two shocks occurs before the shocks impinge upon the rigid wall. In order to investigate the radially propagating shocks, figure 4.20a plots the pressure as a function of angle along the shock for different values of initial stand-off distance, and further compare the results to the spherical collapse; the measurement is performed once the shock wave travels a specific distance from its origin ($r/R_o = 0.9$). Overall, the averaged pressure for non-spherical collapses is lower than that of the spherical case. For non-spherical cases, the pressure is maximum at the tip of the shock, aligned with the jet impact

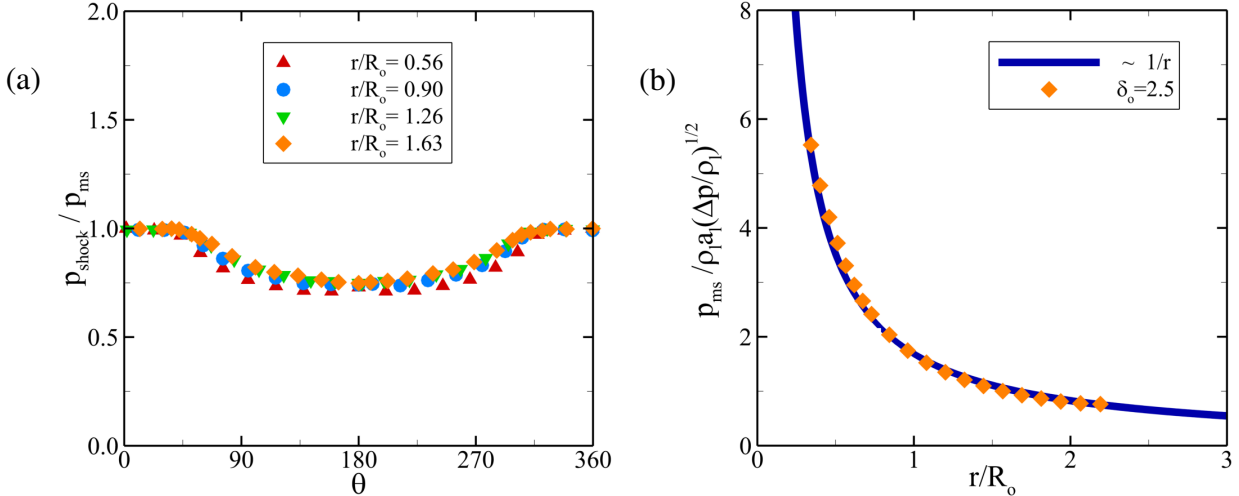


Figure 4.21: (a) Normalized shock pressure as a function of angle at $\delta_o = 2.5$ for different radial distances from the shock origin with $p_\infty = 5$ MPa. (b) Maximum shock pressure vs. radial distances from the shock origin at $\delta_o = 2.5$ and $p_\infty = 5$ MPa.

direction ($\theta = 0^\circ$ and 360°). Although the maximum shock pressure seems to be similar for all cases, the pressure decreases to a minimum value as the angle goes from 0° to 180° . The pressure profiles share a similar trend, with the extent of the reduced pressure off-axis depending on the initial stand-off distance; larger proximities to the wall (or more non-sphericity) result into smaller minimum pressure, and as the collapse starts farther away from the wall, and the profile gets closer to the spherical case. Figure 4.20a quantifies the asymmetry of the pressure distribution along the shock wave as the initial stand-off distance is increased (i.e. the collapse is more spherical). We also plot the pressure distribution along the radial shock wave at different distances from the shock origin for $\delta_o = 2.5$ in figure 4.20b. The pressure trend is similar at different r/R_o , yet as expected, its value decreases as the shock propagates radially outward. If we normalize the pressure by the maximum shock pressure at each distance (p_{ms}), the pressure at different distances from the origin collapse onto a single profile (Figure 4.21a), thus illustrating the self-similarity of the flow. Furthermore, the shock pressure decays as a function of distance as $1/r$. It can be concluded that the directionality matters when measuring the shock pressure, such that the highest pressure is experienced along the centerline on the bubble side closest to the wall, and the lowest pressure in the opposite direction.

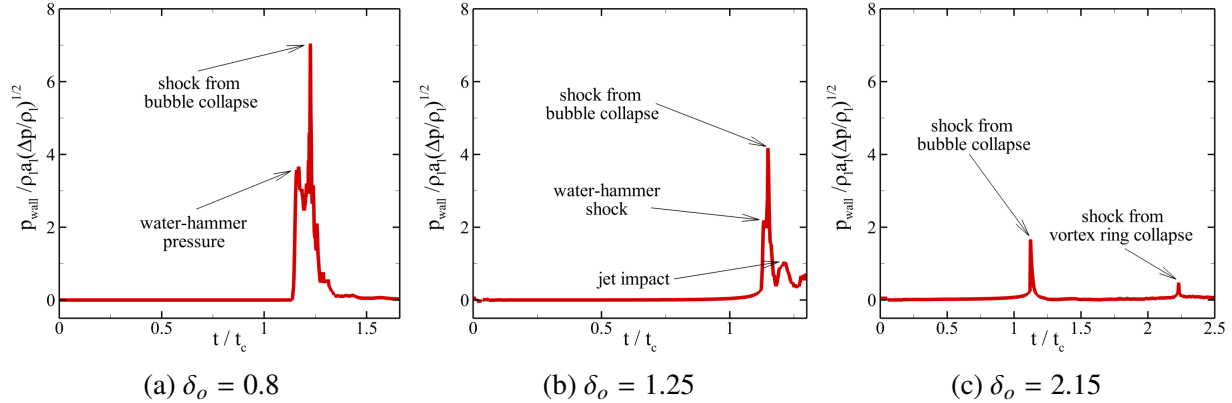


Figure 4.22: Time history of wall pressure along the centerline for different initial stand-off distances with $p_\infty = 5 \text{ MPa}$.

4.5 Wall pressures achieved by non-spherical bubble collapse

The foundation of Franc's four-step description of cavitation erosion (Franc *et al.*, 2011) lies in accurate characterization of impact loads produced by bubble collapse, whether from shock waves or jet impact. The maximum pressure on the wall p_{mw} , caused by inertial collapse of individual bubbles, is a quantity that has been studied in the literature both numerically (Johnsen & Colonius, 2009) and experimentally (Tomita & Shima, 1986).

Our goal is to determine wall pressure is affected by the mechanisms identified in the preceding section. Figure 4.22 shows the time history of the wall pressure along the centerline for three different proximity to the wall. For the attached bubbles ($\delta_o = 0.8$), the jet impacts directly onto the wall, thus creating a region of high pressure due to the water hammer. Thereafter, the toroidal bubble collapses and generates a shock wave which raises the wall pressure even further. For detached bubbles initially located close to the wall ($\delta_o = 1.25$), Figure 4.22b shows that the first pressure peak is caused by the water-hammer shock due to the impact of the re-entrant jet upon the opposite side of the bubble, followed by a larger rise caused by the shock wave produced at minimum volume. After impacting the distal side, the liquid jet drastically decelerates, yet still produces a noticeable pressure increase as it impinges upon the wall. For bubbles starting far enough from the wall ($\delta_o = 2.15$), the merging of the shocks happens prior to impact, and thus a

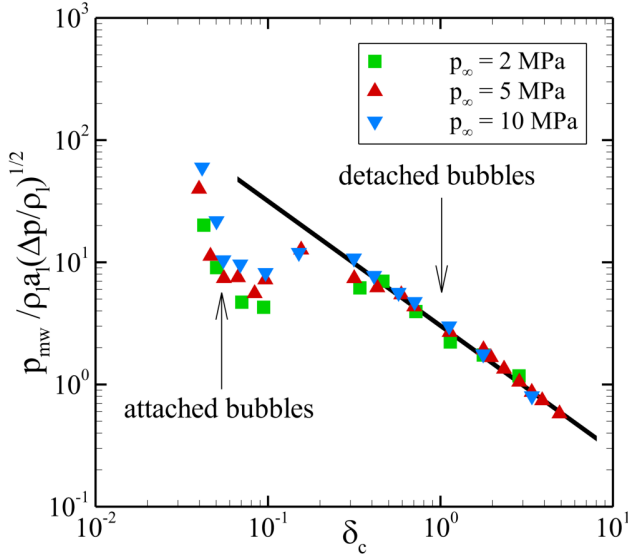


Figure 4.23: Maximum pressure along the wall as a function of collapse location for different driving pressures.

single peak is observed in the wall pressure. By the time the liquid jet reaches the wall surface, it has sufficiently decelerated that the pressure rise due to the jet impact is not significant. However, well after the bubble collapse, we observe a secondary pressure peak caused by the collapse of the vortex ring; the subsequent pressure rise is substantially lower than the first peak (i.e. five times smaller in this case).

In order to estimate the potential damage due to the impact loadings from the collapse, Figure 4.23 plots the maximum pressure along the wall as a function of collapse location, δ_c , for different driving pressures; if nondimensionalized accordingly, the results collapse onto a single curve. Consistent with experimental observations, our numerical simulations also support the fact that the highest pressure amplitudes at the solid surface are caused by attached bubbles (Tomita & Shima, 1986; Vogel *et al.*, 1989; Philipp & Lauterborn, 1998). It is also shown that for detached bubbles, the maximum pressure decays as $1/\delta_c$ (Johnsen & Colonius, 2009). Furthermore, Figure 4.24 defines the normalized radius of the affected area (r^*/R_o) over which the pressure measured on the wall surface exceeds the criterion of $p/(\rho_l a_l^2 \Delta p)^{1/2} > 1$ as a function of initial stand-off distance, for different driving pressures. For attached bubbles, increasing the initial stand-off reduces the affected area, while for detached bubbles it shows a non-monotonic behavior, where the

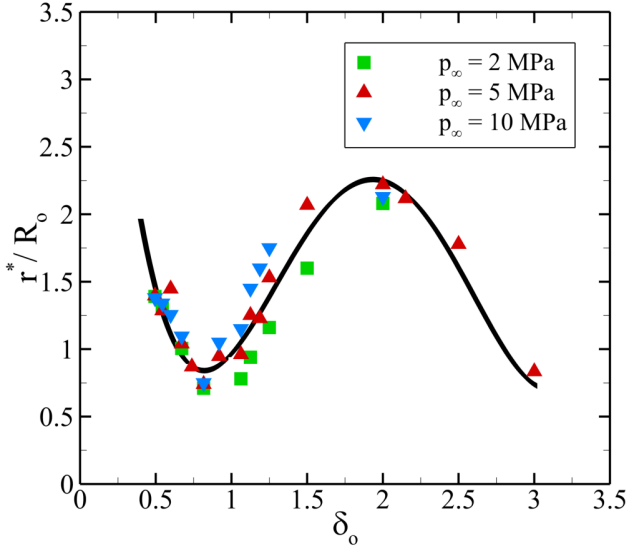


Figure 4.24: The normalized radius of the affected area where the pressure exceeds the criteria of $p/(\rho_l a_l^2 \Delta p)^{1/2} > 1$, as a function of initial stand-off distance for different driving pressures; black solid line: curve fit

affected area is increased with increasing stand-off distance, reaches a maximum at $r^*/R_o \approx 2$, and then decreases. For stand-off distances greater than 3.0, the maximum pressure measured on the wall goes below the criterion as the shock pressure decreases as $1/r$. Considering the scaling for the collapse location in section 4.3.2, one can conclude that attached bubbles are the most likely to produce cavitation-induced damage. In the case of detached bubbles, even though decreasing the initial stand-off distance makes the collapse less intense and produces lower pressures and less energetic shocks, the pressures measured on the wall and the affected area are larger than that of some attached bubbles.

CHAPTER 5

Temperatures produced by collapsing a vapor bubble near a rigid wall

This chapter is adapted from Beig *et al.* (2018).

5.1 Abstract

The dynamics of bubbles inertially collapsing in water near solids have been the object of numerous studies in the context of cavitation erosion. While non-spherical bubble collapse, re-entrant jet dynamics and emitted shock waves have received significant interest, little is known about the temperatures thereby produced and their possible connection to damage. In this chapter, we use highly resolved numerical simulations of a single vapor bubble collapsing near a rigid surface to measure the temperatures produced in the fluid and solid, and to identify the responsible mechanisms. In particular, we find that elevated temperatures along the wall can be produced by one of two mechanisms, depending on the initial stand-off distance of the bubble from the wall and the driving pressure: for bubbles initially far from the wall, the shock generated by the bubble collapse is the source of the high temperature, while bubbles starting initially closer migrate toward the wall and eventually come in contact with it. A scaling is developed to describe the maximum fluid temperature along the wall as a function of the initial stand-off distance and driving pressure. To predict the temperature of the solid, we develop a semi-analytical heat transfer model, which indicates that elevated temperatures achieved during collapse could play a role in cavitation damage to

soft, heat-sensitive materials.

5.2 Introduction

Cavitation and the damage it causes are important outcomes in applications ranging from naval hydrodynamics to medicine and energy sciences. Cavitation bubbles can grow from sub-micron sizes to millimeters, and subsequently collapse in an inertial fashion, thereby generating strong shock waves (Rayleigh, 1917; Flannigan *et al.*, 2006; Lauterborn & Kurz, 2010). A spherical implosion concentrates energy into a small volume, and is even known to emit light in sonoluminescence (Barber & Putterman, 1991) where temperatures between 7,000 – 40,000 K are reported depending on the experimental setup and operating conditions (Brenner *et al.*, 2002; Duplat & Villermaux, 2015). Flannigan & Suslick (2010) measured gas temperatures going from 7,000 K to 16,000 K when increasing the driving pressure from 2.7 to 3.8 bars. Supponen *et al.* (2017) reported peak pressures of 12 GPa for collapse under atmospheric pressure. However, in the vicinity of a neighboring boundary, bubble collapse becomes asymmetric, as evidenced by a re-entrant jet of liquid penetrating the bubble (Naudé & Ellis, 1961; Benjamin & Ellis, 1966; Plesset & Chapman, 1971), which reaches hundreds of meters per second (Philipp & Lauterborn, 1998; Brujan *et al.*, 2002). The jet directionality depends on the type of boundary: a rigid wall induces a jet directed toward the wall, while the jet moves in the direction opposite to a free surface (Blake & Gibson, 1987; Supponen *et al.*, 2016). Regardless of the jet direction, this asymmetry hinders energy concentration such that lower temperatures are achieved. Nevertheless, the impact of the re-entrant jet upon the distal side of the bubble or directly onto a neighboring solid generates a water-hammer shock, and thus high pressures (Tomita & Shima, 1986). The proximity of the bubble to the solid is a key parameter when quantifying the pressure loads on the object: the closer the bubble to the wall, the higher the pressures along the surface (Johnsen & Colonius, 2009).

Studies of inertially collapsing bubbles in the context of cavitation erosion has primarily focused on impact loads produced by the re-entrant jet or shock waves emitted at collapse on hard,

metallic solids. Over extended operation periods, repeated bubble collapse pits the solid, eventually leading to failure and mass loss (Kim *et al.*, 2014). While heating due to stably oscillating bubbles has been investigated in ultrasonics (Legay *et al.*, 2011), the temperatures produced by inertial collapse have not received significant attention as they are assumed second-order effects compared to impact loads (Beig & Johnsen, 2015b). However, recent experiments (Deplancke *et al.*, 2015) suggest that softer materials like Ultra High Molecular Weight Polyethylene (UHMWPE) may fail in a manner different from hard, metallic objects. In particular, local damage characteristic of heating and melting is observed for UHMWPE subjected to a cavitating flow, despite the excellent wear resistance of such materials. At this time, measurement of instantaneous temperatures produced in such complex flows is challenging due to the limited spatio-temporal resolution and dynamic range of temperature-measuring devices such as thermocouples. Unless the temperature of a bubble collapsing near a solid object can be determined, the connection between cavitation and heat-induced damage will be difficult to quantify.

Since a comprehensive study of the real problem requires a full representation of bubble clouds and soft material response to such loading, we first attempt to understand the basic mechanics and heat transfer at the single-bubble level. Our objective is to predict temperatures produced by the collapse of a single bubble near a solid surface using numerical simulations, and to identify the responsible mechanisms. This basic understanding will guide subsequent studies on bubble clouds and solid-fluid coupling occurring in real flows along soft materials, which lie beyond the present scope.

5.3 Fluid temperatures produced by a collapsing bubble

Initially, we consider the collapse of a bubble in a free field, in which case the collapse is spherical as a reference. Figure 5.1 shows the time-evolution of the normalized averaged bubble radius, $R/R_o = (V/V_o)^{1/3}$, where V is the volume, and of temperature at the bubble center obtained from our simulations; time is scaled by the Rayleigh collapse time, $t_c = 0.915R_o \sqrt{\rho_w/\Delta p}$, where ρ_w is the

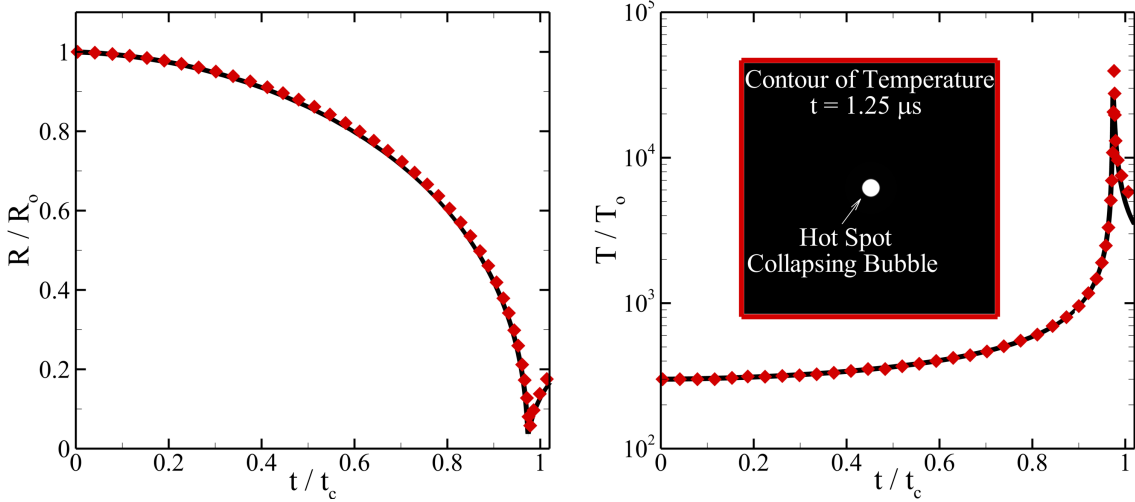


Figure 5.1: Time history of bubble radius and temperature in a spherical collapse of an isolated bubble in water ($p_\infty = 5$ MPa). Black solid line: Keller-Miksis solution; red diamonds: numerical simulation.

liquid density and $\Delta p = (p_\infty - p_o)$, with $p_\infty = 5$ MPa. We compare our results against the solution to a Keller-Miksis (KM) model with full thermal effects inside and outside the bubble (Barajas & Johnsen, 2017). The agreement between the two solutions is good. The bubble collapses due to the higher pressure in the surroundings, reaches high velocities just before collapse, and subsequently rebounds. The temperature in the simulations is slightly larger than that from the KM solution because of the convergence of the initially released shock wave inside the bubble due to the initial conditions (Johnsen & Colonius, 2009). For this spherical collapse, temperatures on the order of 40,000 K would be achieved. Possible causes for the discrepancy between this temperature and those reported by Flannigan & Suslick (2010) are the different driving pressure and potential non-equilibrium effects ignored in our simulations.

We further examine the dynamics of a vapor bubble collapsing near a rigid surface, described in section 3.5.2, for $\delta_o = 1.25$ and $p_\infty = 5$ MPa to qualitatively understand the temperatures produced in the fluid. Figure 5.2 displays volumetric renderings and slices along the centerplane just before and after collapse, and well after collapse. Frame 1 shows that, by breaking the problem symmetry, the presence of the solid surface gives rise to the formation of a liquid re-entrant jet directed toward the wall (Plesset & Chapman, 1971). As illustrated in Figure 5.3, the bubble

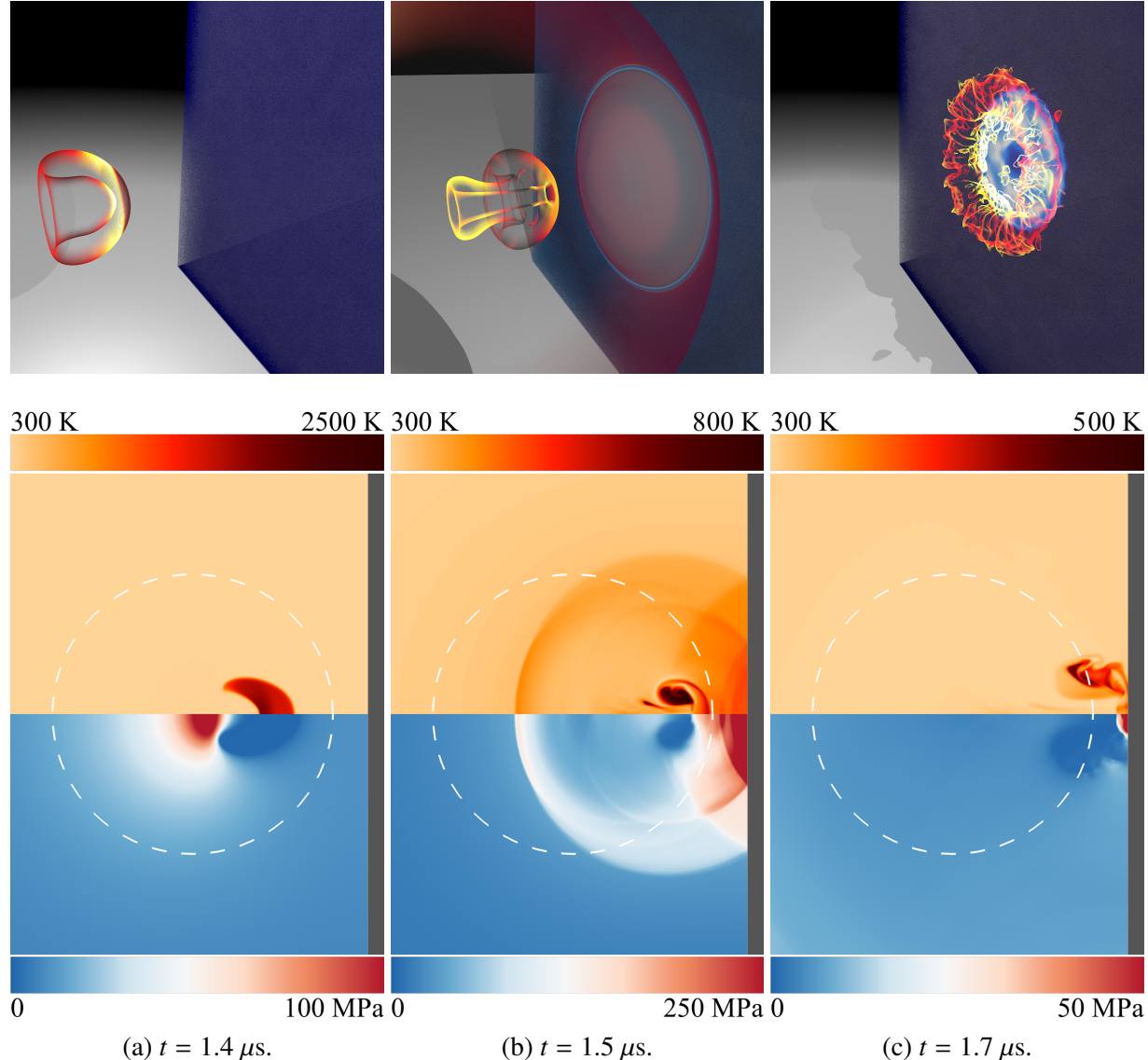


Figure 5.2: Rayleigh collapse near a rigid wall ($\delta_o = 1.25$, $p_\infty = 5 \text{ MPa}$). Top: 3D contours of the bubble's shape colored by temperature. Bottom: 2D slices of temperature (top) and pressure (bottom); white dashed line: initial bubble interface.

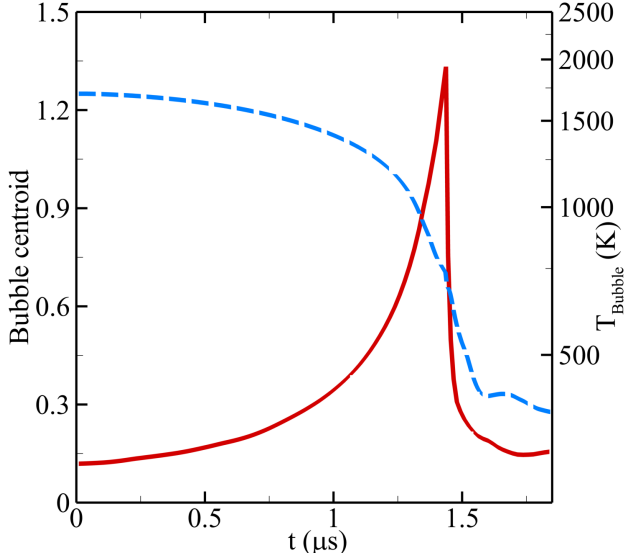


Figure 5.3: Time-evolution of the average bubble temperature (solid red) and centroid distance from the wall (dashed blue) for $\delta_o = 1.25$ and $p_\infty = 5$ MPa.

centroid migrates toward the wall (Vogel *et al.*, 1989) and the spatially averaged bubble temperature increases during the collapse, eventually reaching approximately 2,000 K; locally, inside the bubble, the temperature can be even larger owing to the temperature gradients due to the shock waves trapped inside the bubble (Johnsen & Colonius, 2009). Compared to the spherical case, non-spherical collapse is less intense, characterized by lower temperatures despite the same collapse energy $E = \Delta p V_o$ (Vogel *et al.*, 1989). The non-sphericity of collapse, manifested by jet formation, reduces energy focusing and increases the kinetic energy of the non-converging motions (e.g. jet). Greater proximity to the wall gives rise to a more non-spherical collapse; consequently a larger minimum volume and thus lower temperature are achieved as the initial stand-off distance is reduced. This behavior is further illustrated in Figure 5.4, showing the maximum spatially averaged temperature achieved over the simulation for different initial stand-off distances. Based on the time it takes for waves to propagate from the bubble to the wall and back during the collapse, the critical stand-off at which the collapse is essentially spherical is $\delta_{cr} \approx 10.5$ for $p_\infty = 5$ MPa. Assuming that the maximum bubble temperature goes as the corresponding adiabatic temperature at minimum volume, then $T_{bubble} = T_o(V_o/V_{min})^{\gamma-1}$. From Supponen *et al.* (2016), the volume ratio scales as δ_o^4 if the bubble is initially far from the wall. Thus, we conclude that $T_{bubble} \propto \delta_o^{4(\gamma-1)}$

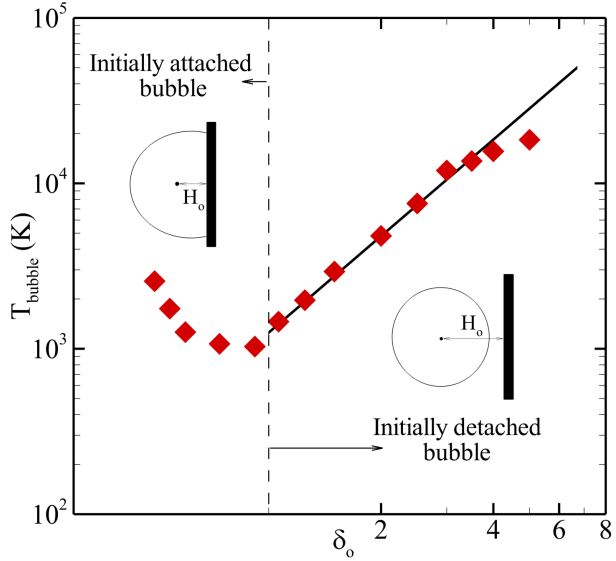


Figure 5.4: Maximum average bubble temperature vs. initial stand-off distance ($p_\infty = 5$ MPa).

(black line in Figure 5.4). For bubbles initially attached to the wall, the temperature increases with decreasing δ_o because the collapse is more intense; this will be discussed below. After reaching a velocity up to 800 m/s, the re-entrant jet hits the distal side of the bubble, thereby generating an outward-propagating, water-hammer shock wave that subsequently reflects off the wall, as illustrated in frame 2 (Figure 5.2). This reflected shock impinges upon the bubble, which by that time has taken the form of a vortex ring (Vogel *et al.*, 1989; Philipp & Lauterborn, 1998). The pressure peak produced by the shock reflection off the wall is expected to be accompanied by a temperature rise. The bubble convects toward the wall and eventually comes in contact with it in frame 3 (Figure 5.2), thus possibly producing high temperatures at the wall. After the collapse, the bubble temperature decreases drastically, eventually reaching an equilibrium value less than 320 K, which results in a high cooling rate ($\sim 10^{10}$ K/s, Brenner *et al.*, 2002).

To quantitatively identify the physics, we examine the fluid temperature along the wall. Based on the bubble dynamics, we expect two mechanisms to give rise to fluid temperature along the wall: the shock produced at collapse, and contact between the bubble and the wall. To better understand this interplay, the maximum temperature of the computational cells in contact with the wall is recorded from the simulations and plotted in Figure 5.5 as a function of the initial stand-off distance for $p_\infty = 5$ MPa. As a comparison, the temperature corresponding to the pressure

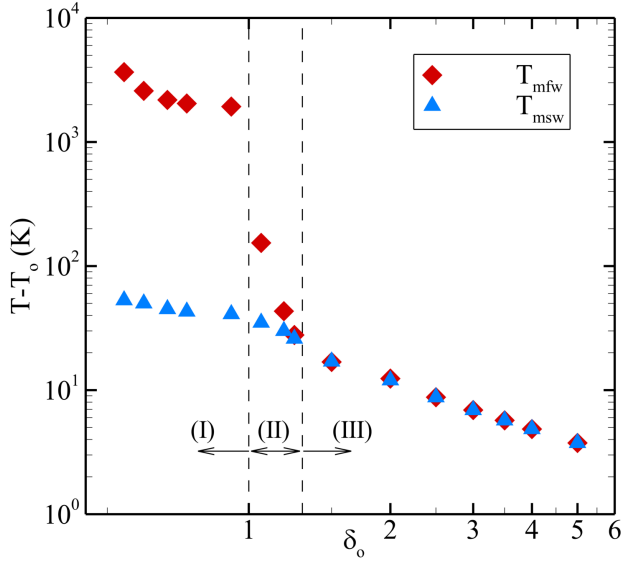


Figure 5.5: Maximum fluid temperature rise along the wall vs. initial stand-off distance ($p_\infty = 5$ MPa). Red diamonds: simulations results; blue triangles: temperature inferred from the equation of state for the reflected shock pressure.

of the shock produced by the collapse at the instant of reflection upon the wall and calculated from the equation of state is included. In addition, Figure 5.6 shows the difference between the time of minimum volume and that when maximum fluid temperature along the wall is measured ($\Delta t = t_{collapse} - t_{T_{mfw}}$), normalized by $t_{collapse}$. Overall, the fluid temperature along the wall increases as the initial stand-off distance is reduced: bubbles closer to the wall produce higher temperatures, as expected. Furthermore, the data fall in three distinct regions. For bubbles starting far enough away from the wall ($\delta_o \gtrsim 1.25$, region III), the peak fluid temperature at the wall agrees with that corresponding to the shock pressure via the equation of state, demonstrating that for these initial stand-off distances the temperature rise is due to the impingement of the shock produced at collapse upon the wall. For $p_\infty = 5$ MPa, this temperature rise reaches up to 30 K. Although the bubble may eventually come in contact with the wall, its temperature after expansion is lower than that due to the shock. The time difference is the time it takes for the shock to propagate between the collapse location and the wall. Since the location at collapse δ_c increases linearly with δ_o in that regime, as explained below, and since the shock propagation speed is close to constant, Δt decreases linearly with decreasing δ_o .

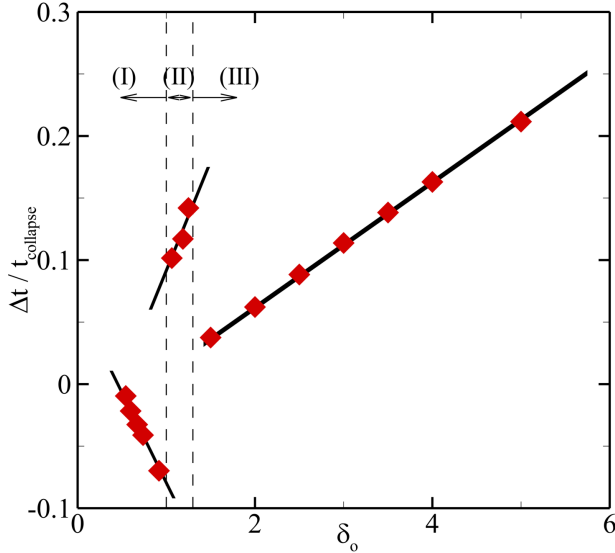


Figure 5.6: Normalized time difference between minimum volume and maximum fluid temperature rise along the wall vs. initial stand-off distance ($p_\infty = 5 \text{ MPa}$).

For those bubbles initially closer to the wall ($\delta_o \lesssim 1.25$), the peak temperature is far greater than that corresponding to the shock pressure. These high temperatures are caused by the bubble coming in contact with the wall. Two regimes are observed. For $1 < \delta_o \lesssim 1.25$ (region II), the bubble is initially detached from the wall, migrates toward the wall during collapse and, during its rebound, comes in contact with the wall. At this time, the bubble volume is sufficiently small that the bubble temperature is greater than that produced by the shock wave. As δ_o is decreased from 1.25 to 1, the volume at the time of contact is smaller. Consequently, higher temperatures are observed. Furthermore, the bubble expands at a rate slower than the speed of propagation of the shock emitted at collapse, such that Δt in region II is larger than in region III. Contact of the hot bubble with the wall is illustrated in Figure 5.7, showing temperature and volume fraction for $\delta_o = 1.05$. The maximum fluid temperature is recorded at a distance approximately 0.25 above the centerline, where liquid volume fraction is close to zero (< 0.02). For $\delta_o \leq 1$ (region I), the bubble is initially in contact with the wall. In this case, jet impact upon the wall drives a second jet into the attached bubble, splitting it in two. The attached bubble is hottest when the shock produced by the first jet compresses it a second time; for these cases, the minimum volume is produced after the impact of the second jet onto the distal side, thus giving rise to negative values of Δt . For the

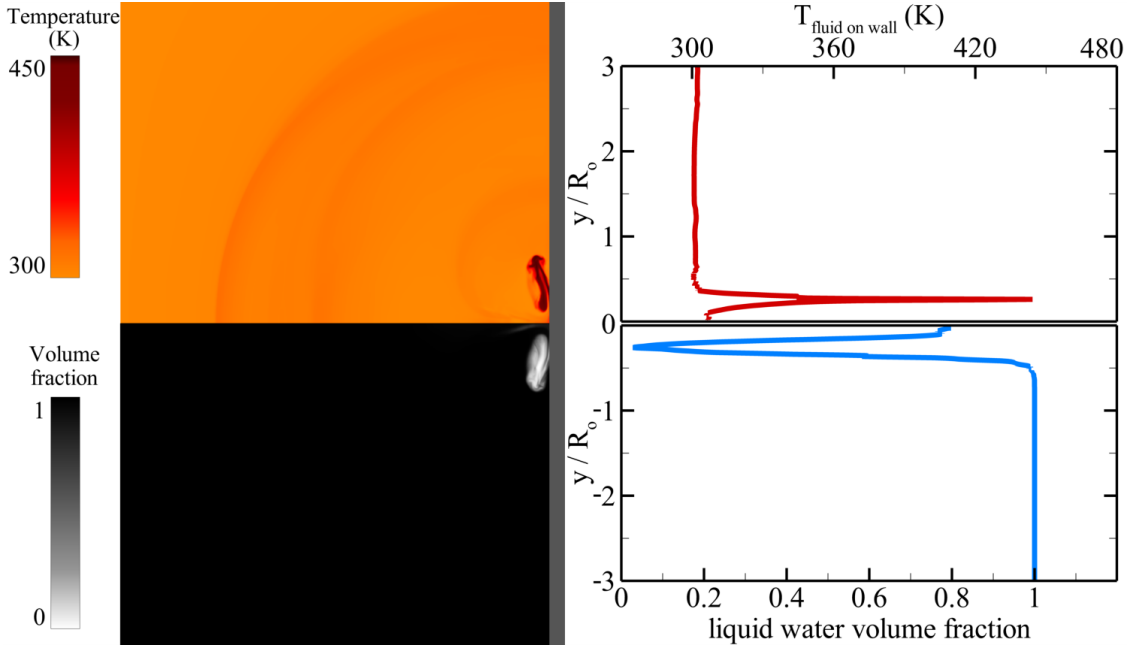


Figure 5.7: Temperature contours (top left) and line (top right) along the wall, and liquid volume fraction contours (bottom left) and line (bottom right) along the wall at the time of maximum fluid temperature along the wall ($p_\infty = 5 \text{ MPa}$, $\delta_o = 1.05$).

smallest values of δ_o , these events occur almost simultaneously.

Given the importance of the location of the bubble at collapse to producing elevated fluid temperatures along the wall, we consider the extent of bubble migration toward the wall during collapse. Figure 5.8 shows the collapse location vs. the initial stand-off distance, both scaled by initial radius, for $p_\infty = 2, 5$ and 10 MPa . The data for these different driving pressure collapse onto a single curve between two limits (large and small δ_o) with linear dependence. Assuming the bubble displacement until the collapse is $\Delta x/R_o$, then $\delta_c = \delta_o - \Delta x/R_o$. For $\delta_o \gg 1$, the displacement scales as $\delta_o^{-4/3}$ (Supponen *et al.*, 2016), such that $\delta_c \approx \delta_o$. This result is consistent with the fact that, for $\delta_o \rightarrow \infty$ (or > 10.5 for $p_\infty = 5 \text{ MPa}$), the bubble does not feel the presence of the wall, thus collapsing spherically with no migration. For initially attached bubbles, the collapse occurs so close to the wall that the mean bubble centroid cannot truly migrate. Thus, δ_c is negligible compared to the bubble displacement. This implies that $\delta_o \sim \Delta x/R_o$, such that $\delta_c \propto \delta_o$. In between, we observe that the presence of the wall “attracts” initially detached bubbles, while attached bubbles are confined by the wall.

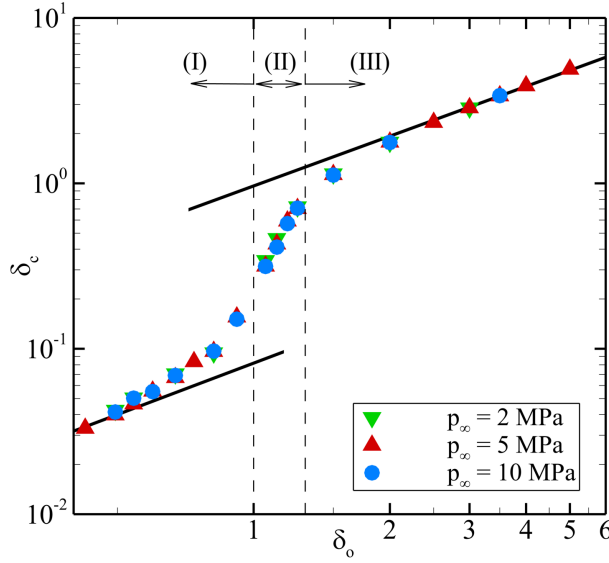


Figure 5.8: Scaling of the collapse location vs. δ_o for different driving pressures, for bubbles initially (I) attached (high temperature due to wall contact), (II) detached (high temperature due to wall contact), and (III) detached (high temperature due to collapse shock).

Now that we understand how to describe bubble migration, we can develop a theory for the maximum fluid temperatures, T_{mfw} , produced by bubble collapse along a rigid wall. We expect that T_{mfw} is not only a function of the driving pressure, but also depends on the bubble's location at the collapse, which itself depends on the initial stand-off distance, i.e. $T_{mfw} = f(\Delta p, \delta_c, \delta_o)$. Introducing a characteristic temperature corresponding to the water-hammer pressure p_{wh} produced at collapse, $\tilde{T} \propto p_{wh}/\rho_w c_v$, connects the dynamics to the re-entrant jet and driving pressure since $p_{wh} \propto \rho_w a_w u_{jet}$, where a_w is the liquid sound speed and $u_{jet} \propto \sqrt{\Delta p/\rho_w}$ (?). From these observations, $\tilde{T} \propto (a_w \sqrt{\Delta p/\rho_w})/c_v$, where c_v is the specific heat at constant volume. Non-dimensionalizing the temperature rise along the wall, $\Delta T = T_{mfw} - T_o$, by the characteristic temperature, \tilde{T} , and incorporating the effects of bubble migration toward the wall, the non-dimensional number $\tau = (\Delta T/\tilde{T})(\delta_o/\delta_c)$ can be constructed, to represent the fluid temperature rise along the wall surface. Figure 5.9 plots this quantity against the initial stand-off distance. In all three regions, the data sets collapse. In region (I), $\tau \sim \delta_o^{-2}$. These bubbles significantly raise the fluid temperature on the wall, leading to non-negligible heat transfer into the neighboring wall, and potentially thermal damage. In region (III), the shock is responsible for the elevated temperature, and

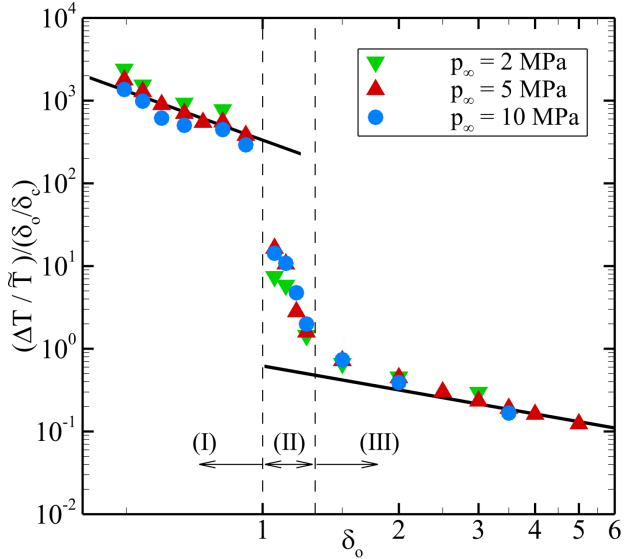


Figure 5.9: Scaling of the maximum fluid temperature rise along the wall vs. δ_o for different driving pressure, for bubbles initially (I) attached (high temperature due to wall contact), (II) detached (high temperature due to wall contact), and (III) detached (high temperature due to collapse shock).

$\tau \sim \delta_o^{-1}$, the same scaling as that of the shock pressure (Johnsen & Colonius, 2009). These results provide insights into the role of high temperatures in cavitation-induced erosion. The collapse of the data indicates that regardless of the mechanism responsible for the high temperature (shock vs. wall contact), the collapse energy $E = \Delta p V_o$ and initial stand-off distance solely dictate the dynamics and energy balance. However, predicting the resulting solid temperature requires one more step, explained in the next section.

5.4 Temperature in the Solid

To predict the solid temperature, the heat transfer problem between the fluid and the solid must be solved. A fully coupled numerical solution to the hydrodynamics would require a prohibitively fine resolution to capture the thermal boundary layer along the wall. To resolve this issue, we develop an analytical heat transfer model based on our simulations data to determine the temperature in the thermal boundary layers at the end of each simulation's time step. The coupling is one-way, with no feedback into the numerical simulations. We solve the following one-dimensional heat diffusion

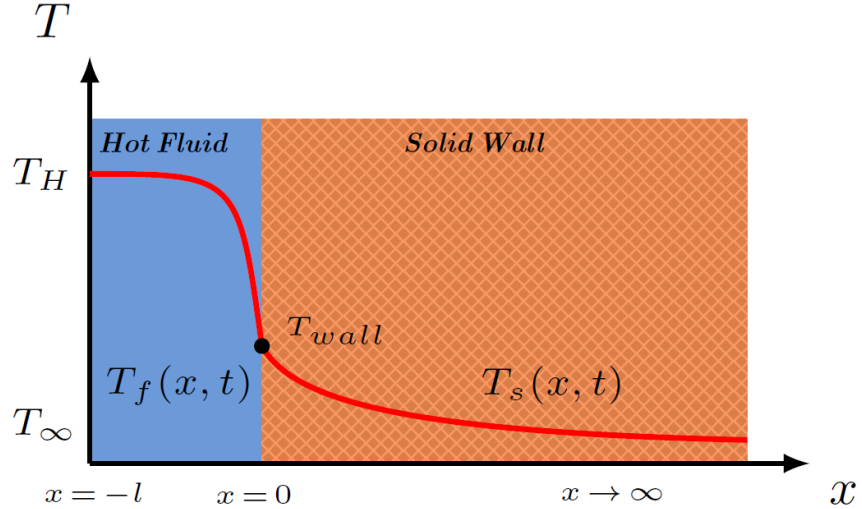


Figure 5.10: Schematic of the thermal boundary layer between the hot fluid and the wall.

equation normal to the wall in a composite and semi-infinite medium, illustrated in Figure (5.10):

$$\frac{\partial T_j}{\partial t} = \lambda_j \frac{\partial^2 T_j}{\partial x^2}, \quad (5.1)$$

where λ is the thermal diffusivity and $j \equiv \{f, s\}$ defines fluid and solid. We solve this equation over the course of a time step corresponding to the numerical simulation, with far-field boundary conditions given by the temperature from the fluid simulation in the cell adjacent to the wall, $T_f(-l, t) = T_H(t)$, and $T_s(x \rightarrow \infty, t) = T_\infty$ in the solid. In addition, both the temperatures and the heat fluxes are equal at the fluid-solid interface, i.e., $T_f(0, t) = T_s(0, t)$ and $k_f \partial_x T_f = k_s \partial_x T_s$. Since T_H comes from our numerical simulations, it varies with time. Thus, the appropriate initial conditions (at the beginning of every computational time step t_i) are that $T_f(x < 0, t_i) = T_H$ and $T_s(x \geq 0, 0) = T_\infty$. In the solid, we approximate the solution at the end of the previous time step by $T_s(x, t_i) = T_\infty + ae^{-bx}$, which is used as the initial condition for the following time step, where a and b are discrete functions of time. At the very first time-step $a = b = 0$, so we can solve the

diffusion equations initially:

$$T_f(x, t) = T_H + \frac{T_H - T_\infty}{1 + \sigma} \left\{ \sum_{n=0}^{\infty} \beta^n \left[\operatorname{erfc} \left(\frac{2(n+1)l + x}{2\sqrt{\alpha_f t}} \right) - \operatorname{erfc} \left(\frac{2nl - x}{2\sqrt{\alpha_f t}} \right) \right] \right\}, \quad (5.2)$$

$$T_s(x, t) = T_\infty + \frac{(T_H - T_\infty)\sigma}{1 + \sigma} \left[\operatorname{erfc} \left(\frac{\gamma x}{2\sqrt{\alpha_f t}} \right) + (\beta + 1) \sum_{n=1}^{\infty} \beta^{n-1} \operatorname{erfc} \left(\frac{2nl + \gamma x}{2\sqrt{\alpha_f t}} \right) \right], \quad (5.3)$$

where $\gamma = \sqrt{\lambda_f/\lambda_s}$, $\sigma = (k_f/k_s)\sqrt{\lambda_f/\lambda_s}$, $\beta = (1 - \sigma)/(1 + \sigma)$.

Thereafter, a and b are found by fitting the exponential function to the temperature in the solid at the end of the time step. The resulting solutions can be written in closed form:

$$\begin{aligned} T_f(x, t) &= T_H - \frac{T_H - T_\infty}{1 + \sigma} \left\{ \sum_{n=0}^{\infty} \beta^n \left[\operatorname{erfc} \left(\frac{2nl - x}{2\sqrt{\lambda_f t}} \right) - \operatorname{erfc} \left(\frac{2(n+1)l + x}{2\sqrt{\lambda_f t}} \right) \right] \right\} \\ &\quad + \frac{a}{1 + \sigma} \left\{ \sum_{n=0}^{\infty} \beta^n e^{h(2nl-x)+h^2\lambda_f t} \left[\operatorname{erfc} \left(\frac{2nl - x}{2\sqrt{\lambda_f t}} + h\sqrt{\lambda_f t} \right) \right. \right. \\ &\quad \left. \left. - e^{2h(x+l)} \operatorname{erfc} \left(\frac{2(n+1)l + x}{2\sqrt{\lambda_f t}} + h\sqrt{\lambda_f t} \right) \right] \right\}, \end{aligned} \quad (5.4)$$

$$\begin{aligned} T_s(x, t) &= T_\infty + \frac{(T_H - T_\infty)\sigma}{1 + \sigma} \left[\operatorname{erfc} \left(\frac{\gamma x}{2\sqrt{\lambda_f t}} \right) + (\beta + 1) \sum_{n=1}^{\infty} \beta^{n-1} \operatorname{erfc} \left(\frac{2nl + \gamma x}{2\sqrt{\lambda_f t}} \right) \right] \\ &\quad - \frac{a\sigma}{1 + \sigma} \left[e^{h\gamma x+h^2\lambda_f t} \operatorname{erfc} \left(\frac{\gamma x}{2\sqrt{\lambda_f t}} + h\sqrt{\lambda_f t} \right) \right. \\ &\quad \left. + (\beta + 1) \sum_{n=1}^{\infty} \beta^{n-1} e^{h(2nl+\gamma x)+h^2\lambda_f t} \operatorname{erfc} \left(\frac{2nl + \gamma x}{2\sqrt{\lambda_f t}} + h\sqrt{\lambda_f t} \right) \right] \\ &\quad + \frac{1}{2}ae^{-bx+\eta t} \left[e^{2bx} \operatorname{erfc} \left(\frac{\gamma x}{2\sqrt{\lambda_f t}} + \sqrt{\eta t} \right) + \operatorname{erfc} \left(\frac{-\gamma x}{2\sqrt{\lambda_f t}} + \sqrt{\eta t} \right) \right], \end{aligned} \quad (5.5)$$

where $\eta = \lambda_s b^2$, and $h = b/\gamma$. This solution applies to any computational cells along the wall, thus providing an approximate solution for the temperature in the boundary layers and inside the solid in the direction normal to the wall.

The resulting expressions for temperature distribution in the solid and the fluid indicate a strong dependence on the thermal properties of the solid (thermal conductivity and diffusivity of the material). In Figure 5.11, we display the dependence of the temperature rise of the wall

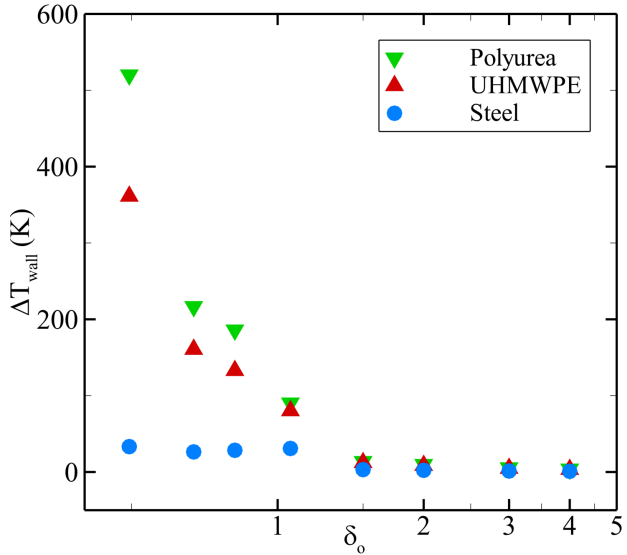


Figure 5.11: Temperature rise of the wall surface for different materials vs. initial stand-off distance, with $p_\infty = 5$ MPa.

surface on the initial stand-off distance for polyurea, Ultra High Molecular Weight Polyethylene (UHMWPE), and steel, commonly used materials in naval hydrodynamics, as a means to assess the temperature effects on cavitation erosion. As expected, only those stand-off distances for which the bubble comes in contact with the wall during collapse generate significant temperature increases. Because of the low thermal diffusivity of polyurea and UHMWPE, the surface temperature can reach values above the melting point of those materials (480 – 620 K for polyurea, ~ 400 K for UHMWPE); on the other hand, the high thermal diffusivity of steel produces only a 30 K rise. The boundary layer thickness at the end of the simulation changes accordingly ($0.5\mu\text{m}$ in polyurea vs. $2\mu\text{m}$ in steel). The high temperatures occur over approximately 100ns in a region of radius $\sim 30\mu\text{m}$. Although the heat transferred to the solid via a single such collapse is small, it is plausible that the repeated collapse of many bubbles in a flow with high cavitation aggressiveness (Kim *et al.*, 2014) gives rise to sufficient heat transfer for melting to occur, especially in soft, heat-sensitive materials.

CHAPTER 6

Inertial collapse of bubble pairs near a rigid wall

6.1 Abstract

Cavitation occurs in a variety of applications ranging from naval structures to biomedical ultrasound. One important consequence is structural damage to neighboring surfaces following repeated inertial collapse of vapor bubbles. Although the mechanical loading produced by the collapse of a single bubble has been widely investigated, less is known about how the presence of a second bubble affects the loading. In such a problem, the bubble-bubble interactions modify the dynamics, e.g., by increasing the non-sphericity of the bubbles and amplifying/hindering the collapse intensity depending on the flow parameters. Here, we quantify the effects of bubble-bubble interactions on the bubble dynamics, as well as the pressures produced by the collapse of a pair of vapor bubbles near a rigid surface. We perform high-resolution simulations of this problem by solving the three-dimensional compressible Navier-Stokes equations for gas/liquid flows. The results are used to investigate the non-spherical bubble dynamics and characterize the pressure fields based on the relevant parameters entering the problem: stand-off distance from the wall surface, the angle, and the distance between the two bubbles.

6.2 Introduction

Studying single bubble dynamics is specifically valuable to explore the physics of the collapse process, and identify the damage mechanisms. However, in most applications, the damaging effects

are caused by the collapse of bubble clouds containing a large number of bubbles. Experimental observations reveal that the collapse of cavitation bubble clouds may emit intense pressures, and induce substantial structural damage (Kubota *et al.*, 1989; Ceccio & Brennen, 1991; Brujan *et al.*, 2012). Hansson *et al.* (1982) investigated the collapse of a hemispherical bubble cloud close to a rigid wall and illustrated that the collapse takes place in an inward fashion. The subsequent inward-propagating shock wave concentrates the collapse energy in the cloud center, leading to the generation of high pressure regions during the collapse of a bubble cloud (Reisman *et al.*, 1998). When a dense bubble cloud collapses near a rigid boundary, the combination of the interactions between the bubble cloud and the neighboring wall, and the interactions among the collapsing bubbles gives rise to bubble asymmetry, and the formation of re-entrant jets (Bremond *et al.*, 2006; Tiwari *et al.*, 2015). In such flows, bubble-bubble interactions must be accounted for to predict impact load, and subsequent cavitation erosion by affecting the overall dynamics.

Owing to the complexity of these nonlinear flows, theoretical approaches are challenging. On the other hand, diagnosing these flows experimentally is not trivial, because of the wide range of spatial and temporal scales, difficult optical access, and lack of accuracy in measuring devices. Numerically resolving the full bubble cloud dynamics is not feasible at the present time. Therefore, these obstacles have triggered the development of simplified homogeneous-mixture models that are typically based on spherical bubble dynamics in incompressible and inviscid liquids (Van Wijngaarden, 1968; Zhang & Prosperetti, 1994; Seo *et al.*, 2010; Ando *et al.*, n.d.; Fuster & Colonius, 2011). These models neglect the non-spherical effects of the collapse and tend to overestimate the produced pressures at the collapse; in a numerical study, Tiwari *et al.* (2015) simulated the collapse of a hemispherical cluster containing 50 bubbles, and measured peak pressures for a variety of configurations over an order of magnitude lower than the values predicted by reduced cloud models.

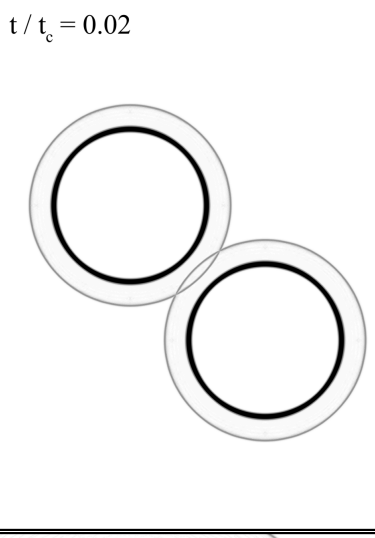
To characterize bubble-bubble interactions and quantify their effects on the collapse nonsphericity and the resulting pressures, we carry out highly-resolved three-dimensional simulations of bubble pairs collapsing near rigid surfaces. Based on our detailed understanding of single-

bubble dynamics (Chapter 4), we perform a parametric study and quantify the bubble morphologies and collapse non-sphericity, examine the radially propagating shocks, and report the pressures measured along the wall surface. By investigating interactions among the bubbles and the boundary, and their effects on bubble dynamics, this study will provide knowledge necessary to develop reduced cloud models that takes the non-spherical effects of the collapse into account, and can be used to perform more realistic simulations.

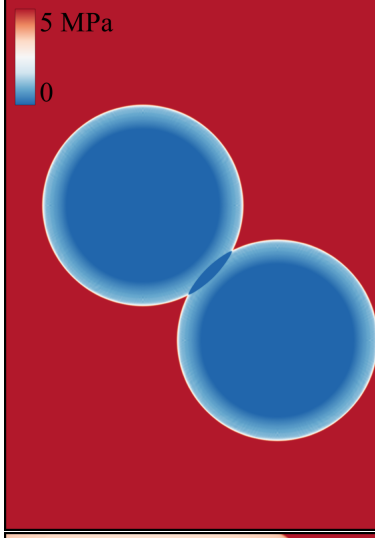
6.3 Qualitative dynamics

In this section, we investigate the dynamics of a vapor bubble pair collapsing near a rigid surface for a variety of geometrical configurations; the problem setup and the relevant parameter space are explained in section 3.5.3. Figure 6.1 shows the contours of density gradient magnitude, pressure, and vorticity at different instances during the collapse, where $\delta_o = 1.5$, $\gamma_o = 2.5$, and $\phi = 45^\circ$. As the collapse starts, the bubbles release radially propagating rarefaction waves, which later interact with each other and the rigid wall ($t/t_c = 0.02$). When the rarefaction impinges upon the bubble interface, a rarefaction is transmitted into the bubble, while a compression wave is reflected back due to the impedance mismatch. These continual interactions result in a zigzag wave pattern in the domain, which further accelerates the bubbles' interface non-uniformly ($t/t_c = 0.11$). As discussed in Chapter 4, the non-uniform acceleration of the bubble interface hinders energy focusing and leads to an asymmetrical collapse ($t/t_c = 0.93$). Similar to single bubble collapse, the pressure in the liquid near the bubbles rises to values beyond p_∞ . In Chapter 4, the formation of the liquid jet within the single bubble collapsing near a rigid wall is discussed in detail. We explained that the presence of the rigid boundary breaks the collapse symmetry and leads to the formation of a liquid jet towards the wall. A re-entrant jet is also observed in the collapse of bubble pairs in a free field, if occurring in-phase, and with bubbles relatively similar in size; in such a case, the jets accelerate towards each other (Tomita *et al.*, 1990; Han *et al.*, 2015). In the bubble pair collapse, the jet forms within the secondary bubble first ($t/t_c = 1.12$). In our problem, unlike single bubble collapse near

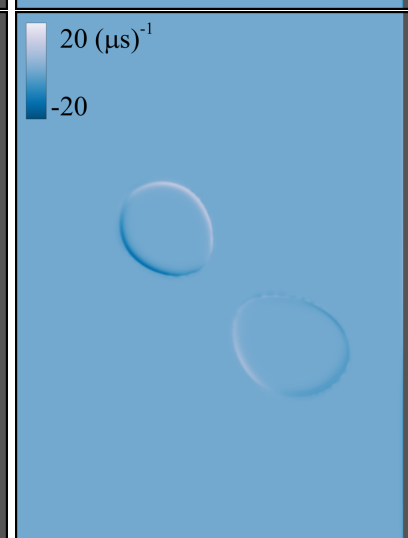
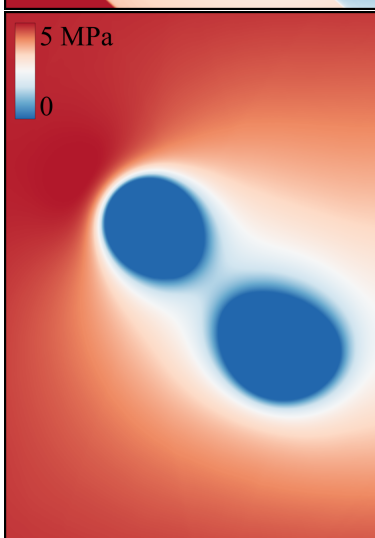
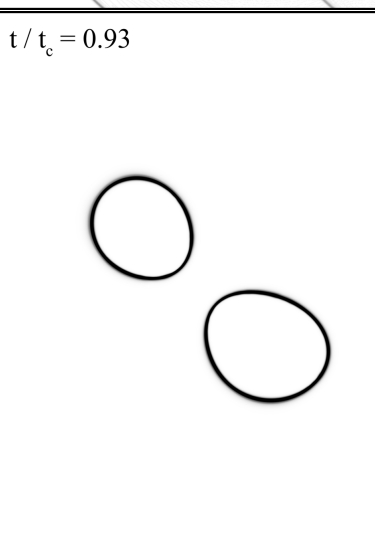
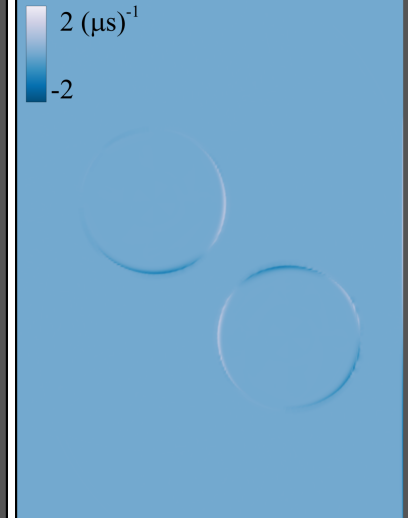
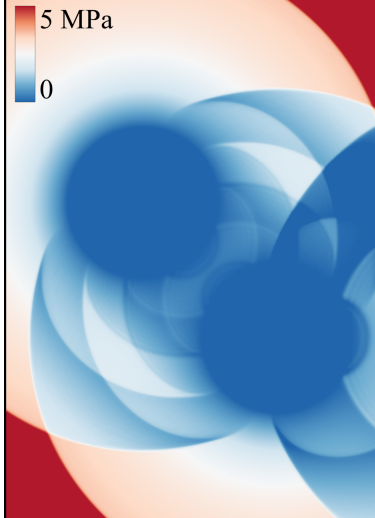
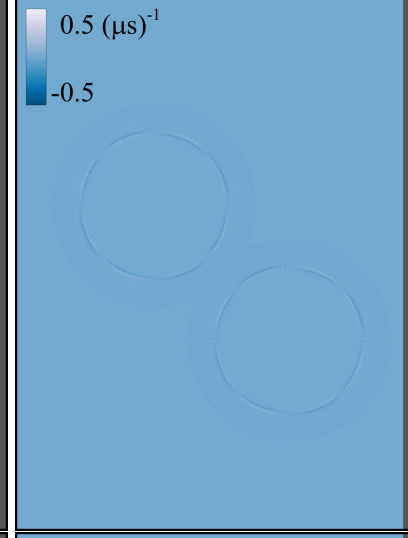
(a) density gradient magnitude

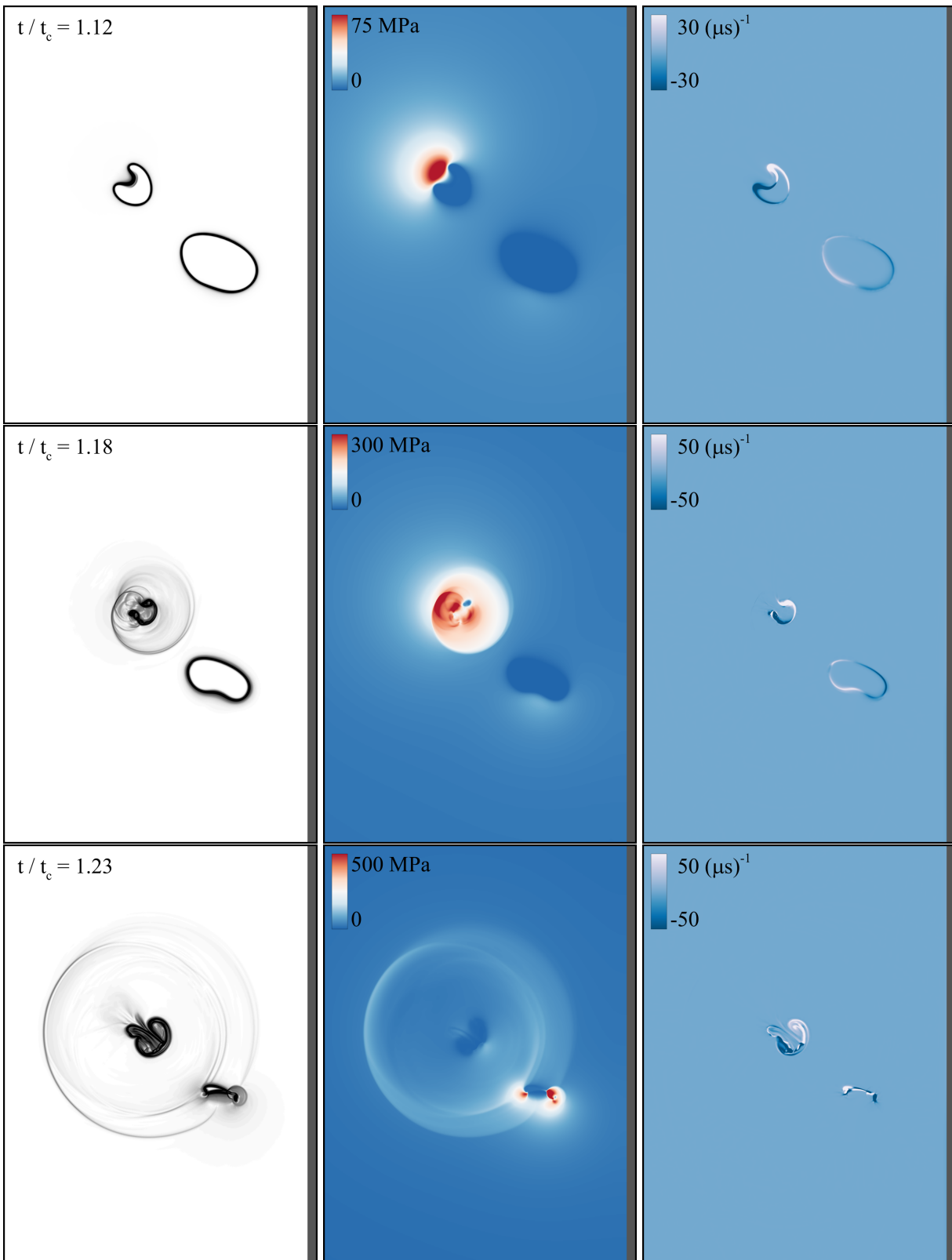


(b) pressure



(c) vorticity





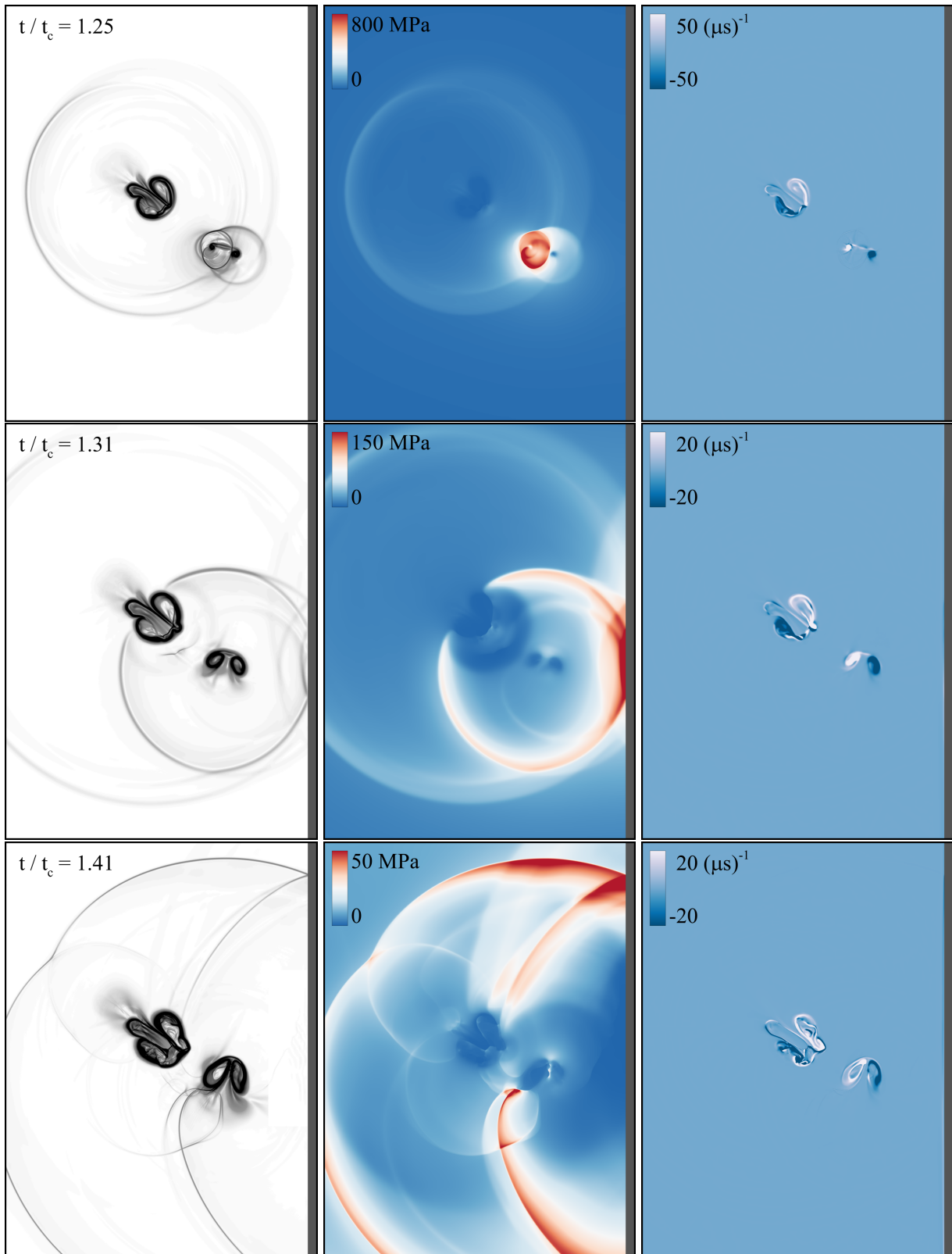


Figure 6.1: Collapse of a bubble pair near a rigid surface ($\delta_o = 1.5$, $\gamma_o = 2.5$, $\phi = 45^\circ$, $p_\infty = 5$ MPa); left: density gradient magnitude, middle: pressure, and right: vorticity contours.

a rigid wall or the collapse of bubble pairs in a free field, the jet is directed neither towards the wall nor the other bubble, but in-between. Upon the impact of the re-entrant jet onto the distal side of the secondary bubble, a water-hammer shock is generated, which, combined with the shock wave from the bubble implosion, creates a high-pressure region ($t/t_c = 1.18$). The bubble then takes the form of a vortex ring migrating in the direction of the jet angle. The secondary bubble has already collapsed at this stage, and the primary bubble is far behind the collapse; the re-entrant jet is observed to form within the primary bubble, tilted slightly away from the wall and towards the secondary bubble. Ultimately, the jet hits the distal side of the primary bubble, and creates a water-hammer shock ($t/t_c = 1.23$). At this time, the shock from the collapse of the secondary bubble has reached the primary bubble and compresses it even more, resulting in a stronger collapse of the primary bubble, and thus producing high pressure regions ($t/t_c = 1.25$). Upon the impact of the shock emitted from the collapse of the secondary bubble, followed by the shock from the primary bubble collapse, high pressures are measured along the wall ($t/t_c = 1.31$). The shock waves reflect back and eventually interact with the vortex rings again ($t/t_c = 1.41$). Although the major events during the collapse (e.g., jet formation, shock propagation, and vortex ring migration) are similar in single-bubble and twin-bubble problems, adding an extra bubble to the flow creates a far more complicated dynamics.

6.4 Jet formation

The collapse of a bubble pair near a rigid surface combines two problems in which re-entrant jets form: collapse of a bubble next to another bubble and collapse of a bubble near a wall. Our numerical simulations show that the jets are formed within both primary and secondary bubbles, though with distorted shapes and geometry-dependent angles. One objective is to estimate the jet angle and the subsequent bubble migration angle based on the initial geometry of the system. For illustration purposes, Figure 6.2 shows the mechanisms inducing the jet formation for each bubble (b). In Figure 6.2b, the dashed line is the symmetry line in the middle of the two bubbles,

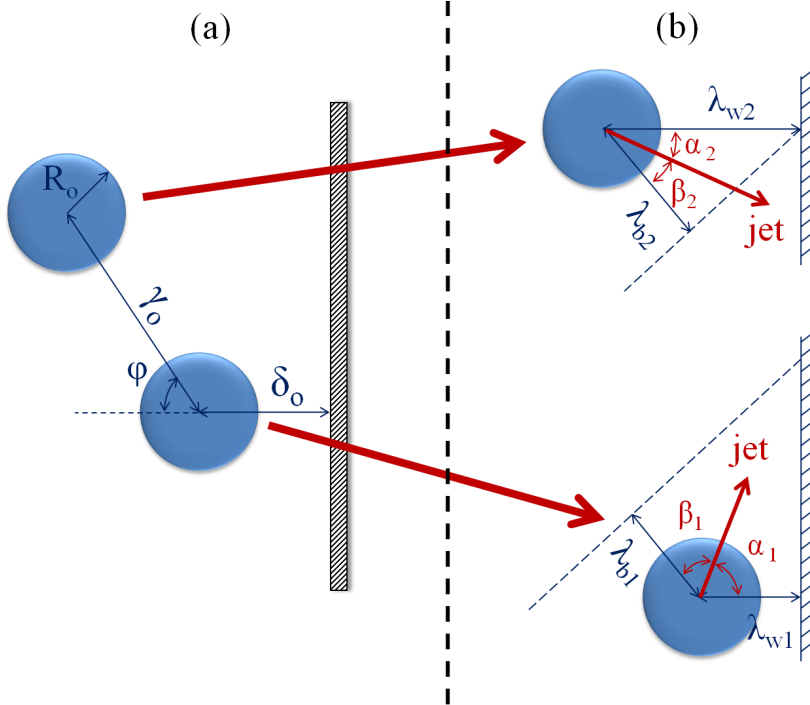


Figure 6.2: Schematic of mechanisms inducing the jet formation in the collapse of bubble pairs near a rigid wall (not to scale).

representing the presence of the other bubble, while the solid-hashed line depicts the rigid wall; α_i is the angle between the jet and the horizontal (jet, and migration angle), β_i is the angle that jet makes with the perpendicular line to the symmetry line, and λ_{bi} , and λ_{wi} are the normalized distances from the initial bubble centroid to the symmetry line and the rigid wall, respectively. We hypothesize that both mechanisms tend to attract the jet and, subsequently, the vortex ring towards themselves, and thus there is a competition between the two; this means that the jet direction is prescribed by the dominant mechanism. Based on this argument, we simply define the strength of each mechanism based on the proximity of the bubble to the relevant source i.e., if the bubble is closer to the wall, the jet direction is likely to be towards the wall, and vice versa. Accordingly, we can write:

$$\frac{\alpha_1}{\beta_1} = \frac{\lambda_{b1}}{\lambda_{w1}} = \frac{\delta_o}{0.5\gamma_o}, \quad (\text{primary bubble}) \quad (6.1a)$$

$$\frac{\alpha_2}{\beta_2} = \frac{\lambda_{b2}}{\lambda_{w2}} = \frac{\delta_o + \gamma_o \cos \phi}{0.5\gamma_o}. \quad (\text{secondary bubble}) \quad (6.1b)$$

From geometry we know:

$$\alpha_1 + \beta_1 = 180 - \phi, \quad (\text{primary bubble}) \quad (6.2\text{a})$$

$$\alpha_2 + \beta_2 = \phi. \quad (\text{secondary bubble}) \quad (6.2\text{b})$$

Then, the jet angles are defined as:

$$\alpha_1 = \frac{\delta_o + 0.5\gamma_o}{\delta_o}(180 - \phi), \quad (\text{primary bubble}) \quad (6.3\text{a})$$

$$\alpha_2 = \frac{\delta_o + \gamma_o(0.5 + \cos \phi)}{\delta_o + \gamma_o \cos \phi} \phi. \quad (\text{secondary bubble}) \quad (6.3\text{b})$$

Given the initial configuration of the problem, one can estimate the jet, and migration angles of both primary and secondary bubbles using Eq. 6.3. We further examine this relation against the results from numerical simulations.

6.4.1 Secondary bubble

Numerical simulations show that the secondary bubble collapses prior to the primary bubble for all configurations, except for $\phi = 90^\circ$, in which case the two bubbles collapse at the same time; this is discussed in more detail in section 6.5. Although the two mechanisms inducing jet formation promote different angles, they are both on the right side of the secondary bubble. Thus, it is anticipated that, the jet points towards the bottom-right and that the vortex ring convects in that same direction. Figure 6.3 shows the jet morphology immediately before impact, at different values of angle ϕ , for $\delta_o = 1.5$, and $\gamma_o = 2.5$. The jet points in the direction perpendicular to the wall ($\alpha_2 = 0^\circ$) at $\phi = 0^\circ$, where the secondary bubble is located directly behind the primary bubble. By increasing the angle ϕ , the jet of the secondary bubble starts to turn away from the horizontal, and reaches the maximum absolute value of $\alpha_2 = 49^\circ$, at $\phi = 90^\circ$. This is shown further in Figure 6.4, where we plot the jet angle (α_2), as a function of the initial configuration angle, ϕ , for fixed distances, $\delta_o = 1.5$, and $\gamma_o = 2.5$. The results show a good agreement with our simplified

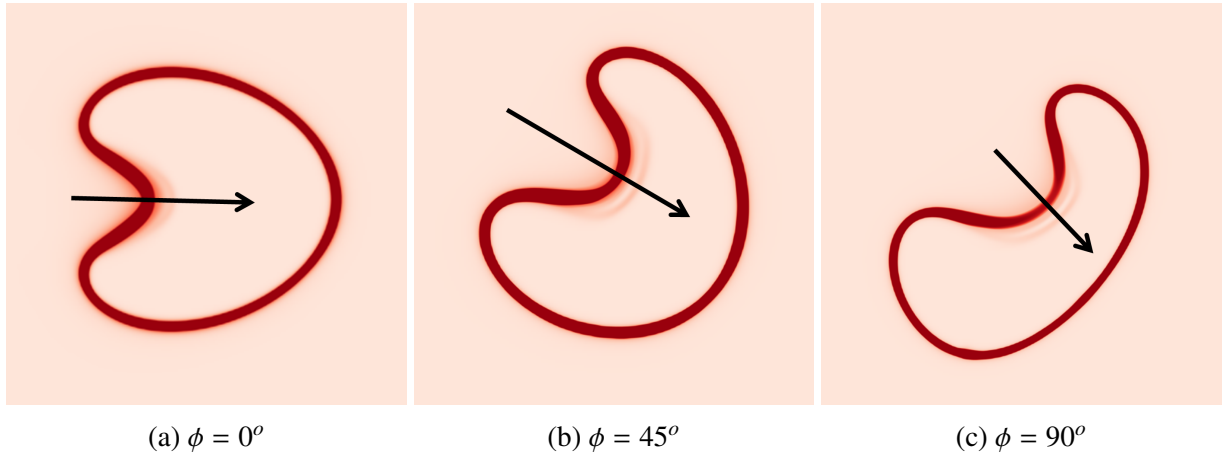


Figure 6.3: Jet of the secondary bubble at different angles, with $\delta_o = 1.5$, $\gamma_o = 2.5$, $p_\infty = 5$ MPa; black arrow defines the jet directionality.

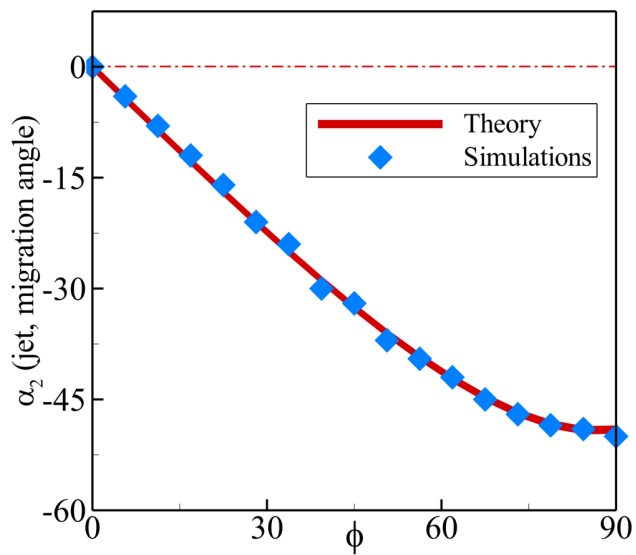


Figure 6.4: Jet angle as a function of the initial angle ϕ , with $\delta_o = 1.5$, $\gamma_o = 2.5$, $p_\infty = 5$ MPa; red dashed-dotted line represents the jet angle in single bubble case.

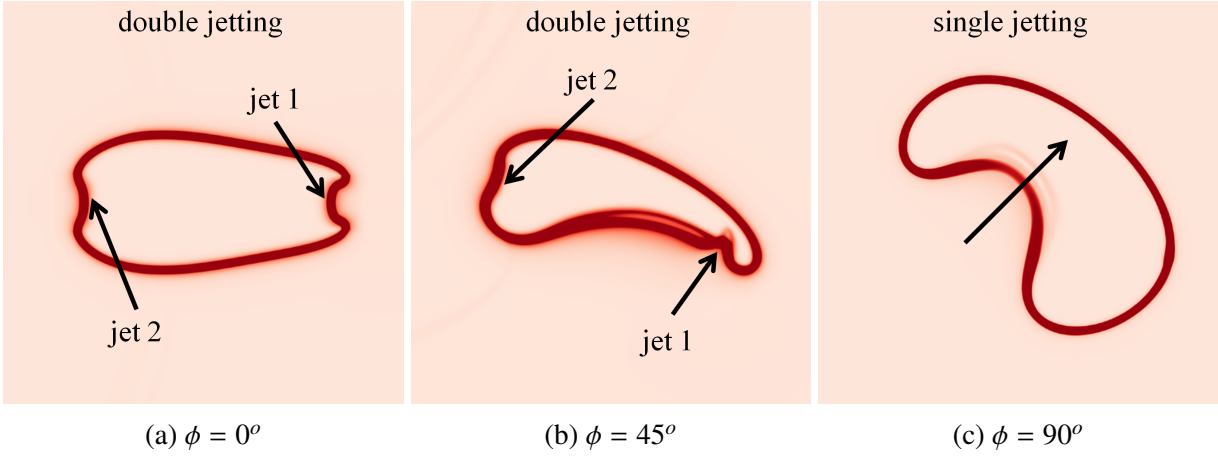


Figure 6.5: Jet of the primary bubble at different angles, with $\delta_o = 1.5$, $\gamma_o = 2.5$, $p_\infty = 5$ MPa.

theory. As expected, the absolute value of the jet angle increases by increasing the angle ϕ .

6.4.2 Primary bubble

Unlike the secondary bubble, the mechanisms leading to jet formation (presence of another bubble and of a wall) lie on opposite sides of the primary bubble, which can lead to a more non-spherical behavior and eventually complicate the dynamics further. Figure 6.5 qualitatively illustrates the primary bubble shape, and the jet(s) formation, just before the impact, for three different values of ϕ , with $\delta_o = 1.5$, and $\gamma_o = 2.5$. Figure 6.6 shows jet and migration angles versus the initial configuration angle, ϕ , for fixed distances, $\delta_o = 1.5$, and $\gamma_o = 2.5$. According to the simulations, two re-entrant jets are observed to form within the primary bubble at $\phi = 0^\circ$; one with angle 0° , and the other one with angle 180° in the exact opposite direction. At $\phi = 45^\circ$, “jet 1” is about to hit the distal side, while “jet 2” is still developing. However, for $\phi = 90^\circ$, only one single jet at angle 49° is observed. By increasing ϕ from 0° to 90° , the jets start deforming, and ultimately at $\phi \approx 56^\circ$, double-jetting no longer occurs and a single jet is observed. Although our simplified theory can predict the direction of the primary bubble migration after the collapse, it cannot determine the jet angles in the regime where double jetting occurs; after this threshold, a single jet is formed and the proposed model accurately describes the jet angle and, subsequently, the direction of the bubble migration. The emergence of double jetting affects the dynamics, the generated shock waves, and

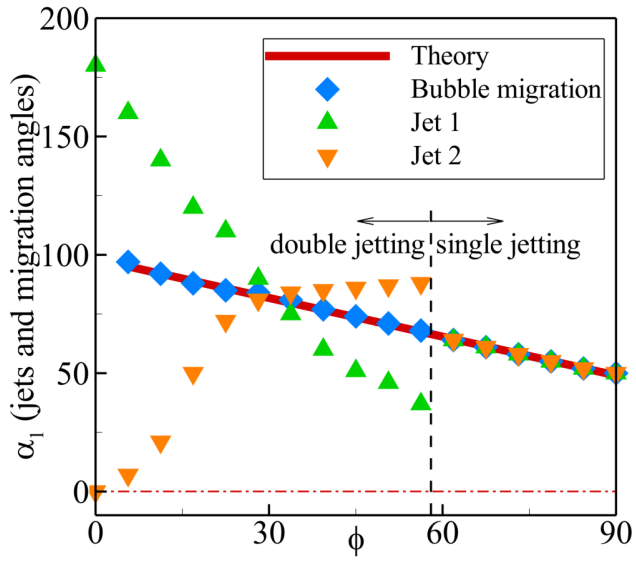


Figure 6.6: Jet and migration angles as a function of the initial angle ϕ , with $\delta_o = 1.5$, $\gamma_o = 2.5$, $p_\infty = 5$ MPa; red dashed-dotted line represents the jet angle in single bubble case.

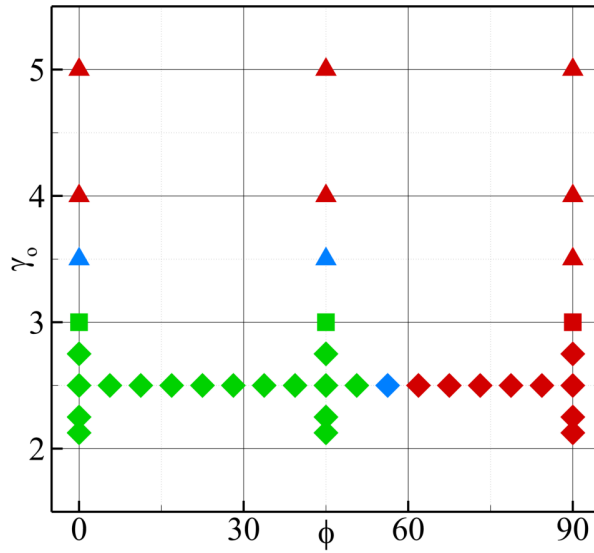


Figure 6.7: Occurrence of the double jetting event during the collapse of a bubble pair near a wall as a function of ϕ and γ_o ($\delta_o = 1.5$, and $p_\infty = 5$ MPa); green: double jetting is observed, red: single jetting is detected, and blue: neutral line; squares: both secondary bubble and rigid wall meet the primary bubble at the exact same time, triangles: rigid wall meets first, diamonds: secondary bubble meets first.

pressure loadings produced at the collapse; this is discussed in more detail below. The occurrence of the double jetting event in the $\gamma_o - \phi$ parameter space is presented in Figure 6.7; the green color shows that the double jetting has occurred, while the red color illustrates that only one single jet is observed within the primary bubble. As explained above, the two mechanisms leading to jet formation compete to attract the primary bubble towards themselves; Figure 6.7 further shows which of the two mechanisms wins this competition. It is observed that if the bubbles are initially located far apart from each other ($\gamma_o \geq 3.5$), regardless of the angle ϕ , a single jet forms in the primary bubble. However, if the bubbles are initially close to each other, the angle ϕ is important in that for small angles the double jetting is detected, while large angles lead to the formation of a single jet. At $\phi = 90^\circ$, no matter how close the bubbles are to each other, a jet is observed in the primary bubble. It can be concluded that the role of initial configuration (e.g., the arrangement of the bubbles and their proximity to the rigid wall) on the collapse non-sphericity and overall dynamics is non-negligible.

6.5 Collapse properties

In this section, we report some of the collapse properties, such as the collapse time ($t_{collapse}$), the normalized collapse location with respect to the wall (δ_c), and the maximum pressure produced at the collapse (p_{max}). To investigate the role of the angle ϕ on collapse dynamics, and specifically on the desirable parameters, we set the initial stand-off distance of the primary bubble from the wall to $\delta_o = 1.5$, and the distance between the two bubbles to $\gamma_o = 2.5$.

Accordingly, Figure 6.8 plots the collapse time versus the angle ϕ . Single bubble studies, both experimental (Philipp & Lauterborn, 1998) and numerical (Johnsen & Colonius, 2009), have shown that for the bubbles with lower proximity to the rigid wall, the collapse occurs faster. Here, we observe that for all cases, the secondary bubble, which is farther away from the wall compared to the primary bubble collapses faster, except for $\phi = 90^\circ$, where both bubbles have the same initial stand-off distance from the wall, and the problem is symmetric with respect to the plane between

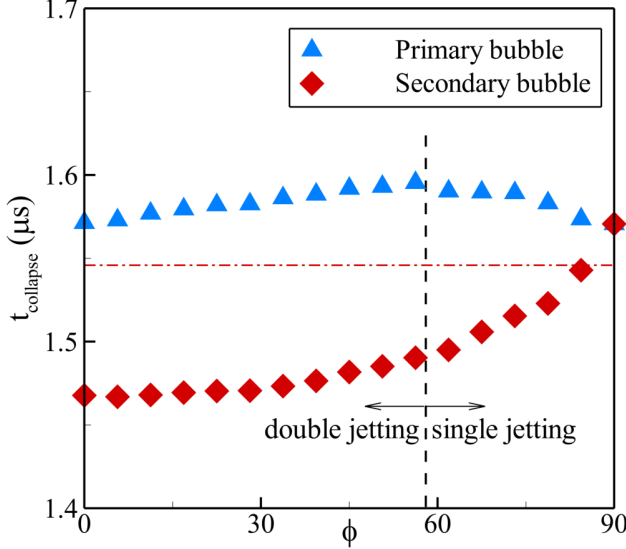


Figure 6.8: Collapse time as a function of the angle ϕ , with $\delta_o = 1.5$, $\gamma_o = 2.5$, $p_\infty = 5$ MPa; red dashed-dotted line represents the collapse time in single bubble case.

the two bubbles; thus both primary and secondary bubbles collapse at the exact same time. However, varying the angle ϕ does not significantly affect the collapse time of the primary bubble, since both distances, from the secondary bubble and the wall, are fixed. On the other hand, increasing the angle ϕ initially delays the primary bubble collapse; $t_{collapse}$ reaches a maximum at $\phi = 56^\circ$ (the threshold at which the double jetting no longer occurs), and then decreases monotonically. It is also noticed that the time difference between the two collapses decreases as the angle ϕ increases, leading to more synchronized collapses. This is especially important when measuring the pressures along the wall, since superposition of pressure pulses from each collapse at the point of intersection on the wall can considerably increase the impact loads; more synchronization pushes the pressure peaks closer to one another in time.

It is known that the peak pressure of the radially propagating shocks decays as $1/r$, where r is distance from the origin; [Johnsen & Colonius \(2009\)](#) show that the bubbles collapsing closer to the wall lead to higher pressures along the wall. Therefore, collapse location is a key player in creating high pressure regions on the wall. We plot the collapse location, δ_c , as a function of angle ϕ in Figure 6.9. The collapse location for both primary and secondary bubbles monotonically decreases as the angle ϕ increases, meaning that for larger angles, the shock waves from the collapse are

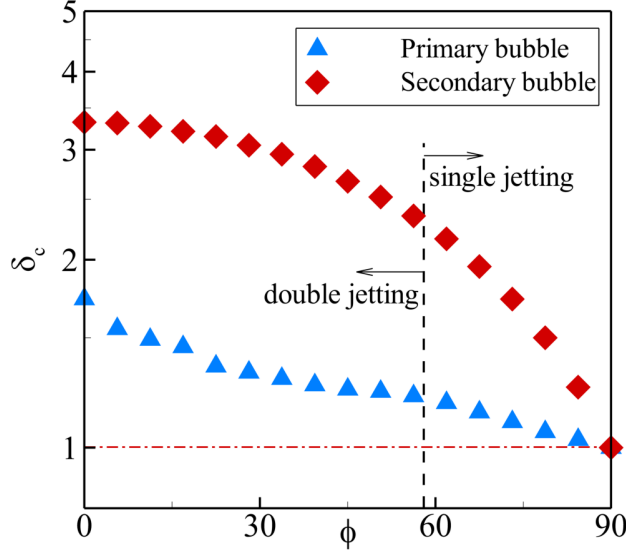


Figure 6.9: Collapse location as a function of the initial angle ϕ , with $\delta_o = 1.5$, $\gamma_o = 2.5$, $p_\infty = 5$ MPa; red dashed-dotted line represents the collapse time in single bubble case.

generated closer to the rigid wall surface.

Furthermore, Figure 6.10 shows the maximum pressure produced at the collapse of both primary and secondary bubbles as a function of angle ϕ . Overall, the collapse intensity and, subsequently, the maximum pressure produced by the collapse decrease with increasing the angle. It is observed that in the region where double jetting takes place, the maximum pressure produced by the primary bubble is high, showing the effects of the double jetting event on collapse intensity. In fact, at smaller angles where double jetting is observed, the maximum pressure is higher than that of a single bubble, while at greater angles pressures lower than that of a single bubble are achieved. However, the maximum pressure from the collapse of the secondary bubble is always lower than that of a single bubble.

6.6 Wall pressure

The wall pressure p_{mw} is a quantity of interest for erosion. Figure 6.11 shows how this quantity depends on the angle. The maximum wall pressure behaves in a non-monotonic fashion: it initially increases and reaches a local maximum as the angle is increased; thereafter, it starts to decrease to

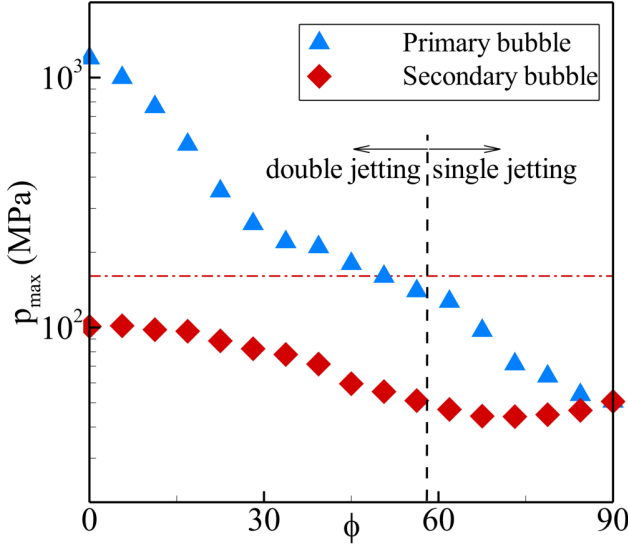


Figure 6.10: Collapse pressure as a function of the initial angle ϕ , with $\delta_o = 1.5$, $\gamma_o = 2.5$, $p_\infty = 5$ MPa; red dashed-dotted line represents the collapse time in single bubble case.

a minimum value at $\phi = 75^\circ$, and increases again thereafter to reach its highest value at $\phi = 90^\circ$. For all cases, p_{mw} is lower than that of a single bubble, except for $\phi = 90^\circ$ where the reported value is slightly higher than the pressure produced by a single bubble.

As explained above, collapse time, location, and intensity all combine to generate the high pressure regions along the wall. Although the collapse intensity increases and thus creates higher pressures at lower angles, the time difference between the two collapses and the collapse location increases accordingly. In fact, a combination of these three factors, which all behave in a different non-linear fashion with respect to angle ϕ , defines the non-monotonic behavior of maximum wall pressure along the wall. In general, the presence of the secondary bubble lowers the impact loads along the wall surface.

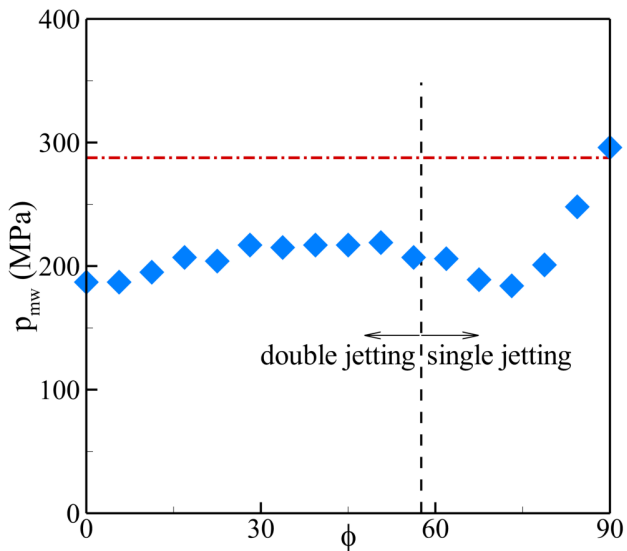


Figure 6.11: Maximum wall pressure as a function of the initial angle ϕ , with $\delta_o = 1.5$, $\gamma_o = 2.5$, $p_\infty = 5$ MPa; red dashed-dotted line represents the collapse time in single bubble case.

CHAPTER 7

Conclusions and future work

This chapter provides a summary of this research, and suggests several active topics for potential future studies.

7.1 Concluding remarks

The main objectives of this study were (i) to develop a novel numerical model, and a robust computational framework, capable of simulating compressible multiphase flows with shocks and interfaces, and (ii) to explore the inertial collapse of individual bubbles in the vicinity of rigid boundaries, investigate the overall bubble dynamics, and quantify the potential damage induced by the collapse process.

7.1.1 Numerical approach

We developed an interface-capturing approach capable of accurately and robustly representing shock waves and high-density-ratio material interfaces. We showed that a naive implementation of shock capturing gives rise to spurious pressure and temperature oscillations across the material discontinuities. Although such errors in temperature are not relevant in Euler simulations, they become problematic in Navier-Stokes calculations by giving rise to energy errors due to heat conduction. We showed that the numerical errors described herein can significantly overpredict pressures and temperatures (sometimes with over 100% error), and affect vortical structures, in

situations of engineering relevance, e.g., bubble collapse.

To prevent these errors, we extended the approach of [Johnsen & Ham \(2012\)](#) to several multiphase models (γ , volume fraction, and mass fraction models), solving the compressible Navier-Stokes equations for a binary gas-liquid system, where all the materials obey a single equation of state with spatially varying properties. We explained that these pressure and temperature errors can be prevented by computing the material properties in the equation of state based on appropriate transport equations in conservative and non-conservative forms, depending on the multiphase model. This volume fraction model (also sometimes referred to as the five-equations model), which is adaptable to different equations of state, served as the basis for investigations of bubble dynamics in this study. To resolve the bubble interface, the dilatational source term in the volume fraction equation in advection form needs to be included, for which care must be taken to overcome certain numerical difficulties.

For discretization, we developed a solution-adaptive central/discontinuity-capturing approach. Our spatial scheme is high-order accurate in smooth regions and nominally non-dissipative; high-order discontinuity capturing is applied only at sharp gradients detected by a discontinuity sensor. This approach was specially designed to simulate non-spherical dynamics of individual bubbles and the resulting shock waves produced during collapse. An in-house computational code, implementing the Message Passing Interface (MPI) paradigm for parallelization, and Hierarchical Data Format (HDF5) for I/O, was developed in C++ to perform the proposed three-dimensional high-resolution simulations. The code was verified and validated using a suite of problems.

7.1.2 Flow physics

The foundation of our physical investigations is based on the observation that at the small-scales (individual bubbles) the collapse of a single bubble should only be a function of the pressure driving the collapse and the initial stand-off distance. In other words, the macroscopic flow, which is problem-/geometry-dependent, transports the bubbles and exposes them to pressures driving an inertial collapse; once the pressure ratio and stand-off distance from the surface are known, it is

expected that bubbles collapse in a “universal” fashion. Thus, we considered the collapse of a single bubble at a prescribed initial distance from a solid wall and driven by a given pressure ratio. In other words, given the location of a bubble and the driving pressure in the flow field of any application, we can predict the pressure produced along a neighboring object.

We carried out highly resolved numerical simulations of a single vapor bubble collapsing near a rigid wall. We considered a range of initial stand-off distances from the neighboring wall ($0.5 \leq \delta_o \leq 5.0$, where δ_o is the normalized initial stand-off distance). The presence of the wall breaks the symmetry of the collapse (as evidenced by the formation of a re-entrant jet), gives rise to momentum of non-converging motions and hinders energy concentration that would otherwise occur in a spherical collapse; the energy defocussing ultimately reduces the collapse intensity, thus producing lower pressures and temperatures, compared to a spherical collapse. However, bubbles near a rigid wall collapse in a non-spherical fashion. The non-sphericity of the collapse was quantified, showing that it strongly depends on the bubble proximity to the wall; the collapse is the most non-spherical when $\delta_o \approx 1$. With an appropriate definition of non-sphericity, we can explain the discrepancies between spherical and non-spherical collapse, and scale the main collapse properties (e.g., collapse intensity, bubble migration, and maximum jet velocity).

Using Rayleigh-Plesset analysis and the potential flow theory, we investigated the process leading to jet formation, suggesting that the local pressure increase behind the jet and prior to impact is not the cause for the jet formation, but rather the consequence of it. We studied the sequence of shock waves emitted after the collapse, and showed that the implosion shock (generated at the instant of the collapse, after the bubble reaches its minimum volume) follows the water-hammer shock (produced at jet impact), and eventually merges with it to form a single shock wave. We showed that the merging happens before the shock hits the wall if $\delta_o \geq 2.0$. We identified the directionality of the radially propagating shock wave, showing that the pressure along the shock is not uniform, and in fact is maximum along the axis of symmetry (normal to the wall). As a measure of the damage potential, we quantified the pressure loads produced by the bubble collapse for different geometrical configurations, and found that the bubbles with high proximity to

the wall ($\delta_o \leq 1.25$), are likely to be the most destructive. We developed a scaling describing the dependence of the wall pressure on the initial stand-off distance and the driving pressure.

According to recent experimental studies, soft materials (e.g., Ultra High Molecular Weight Polyethylene, or UHMWPE) exposed to cavitation are prone to damage characteristic of melting, rather than due to impact loads. However, the instantaneous temperatures thereby produced cannot be measured experimentally, thus preventing a quantitative connection between cavitation and heat-induced damage. Therefore, in the first study of this problem, we calculated the temperatures thereby produced. We demonstrated that the maximum temperature along the wall occurs via one of two mechanisms, depending on the initial stand-off distance: the shock produced upon bubble collapse and reflecting off the wall (large stand-off distances), and contact of the hot bubble with the wall due to migration during collapse (small stand-off distances). We described bubble migration during collapse and, using this result, discovered a scaling describing the maximum fluid temperature along the wall as a function of the initial stand-off distance and driving pressure.

To determine the temperature of the neighboring solid, we developed an analytical heat transfer model relying on the simulations results. Given the simulations results as a time-varying boundary condition, we solve the corresponding one-dimensional heat diffusion problem in the solid. Our results indicate that, for certain soft, temperature-sensitive materials, instantaneous temperatures greater than the melting point are produced on the solid surface during bubble collapse, though over a short time ($\lesssim 1 \mu s$). Although the heat transferred to the solid via a single such collapse is small and unlikely to be sufficient to melt the adjacent solid, it is plausible that the repeated collapse of many bubbles gives rise to sufficient heat transfer for melting to occur, especially in soft materials. By investigating the relevant mechanisms raising the wall temperature, this study provided insight into the potential role of thermal damage in cavitation-induced erosion.

Cavitation erosion is generally caused by the collapse of many bubbles. Even the most sophisticated cloud models are based on spherical bubble dynamics. However, given the discrepancy observed in our spherical vs. non-spherical simulations, it is unclear whether cloud models based on spherical bubble dynamics can accurately predict impact loads as they collapse near solids.

Bubble-bubble interactions may result in more complex non-spherical behavior and affect the collapse properties further. To quantify the effects of these interactions on bubble dynamics, we simulated the collapse of a pair of vapor bubbles near a rigid wall.

We showed that if a second bubble is placed in the vicinity of the original bubble (i.e., that in the single-bubble study), the collapse becomes far more complicated. In fact, bubble-bubble interactions increase the non-sphericity of the bubbles, compared to the single-bubble case, such that the scalings we developed for the single bubble dynamics no longer hold. These interactions may amplify or reduce the pressures produced at the collapse, depending on the initial configuration of the problem. We showed that the maximum pressure along the wall behaves non-monotonically in the presence of the secondary bubble as the angle is varied. Bubble-bubble interactions affect the pressures measured on the wall and thus cannot be neglected. Distorted re-entrant jets were observed to form within both bubbles, and it was shown that depending on the geometrical configuration, two jets were detected penetrating the primary bubble, an event we call “double jetting”. Upon the occurrence of double jetting, the flow can be substantially affected, resulting in even more complex dynamics.

7.2 Recommendations for future research directions

7.2.1 Physical model

There are limitations to the numerical model used in this study. The first, is that phase change is neglected. Due to the short time scales of the problems of interest, it is unlikely that phase change affects the bubble dynamics until collapse; for larger driving pressures, non-equilibrium effects may reduce the condensation rate of the water vapor inside the bubble and thus moderate the rebound, which would lead to a less intense collapse with lower pressures and temperatures. On the other hand, the pressure reduction due to propagation of rarefaction waves in water may lead to cavity formation, particularly between the bubble and the wall, that may ultimately collapse and intensify pressures and temperatures thereby produced. Phase change, including under non-

equilibrium conditions, could be implemented by following the Seven-equations model (Saurel & Abgrall, 1999a) or that of Pelanti & Shyue (2014).

Second, capillary effects are neglected. Based on the jet speed and the local curvature of interest, Weber numbers are estimated to be between 2×10^5 to 3×10^6 , though of course in the absence of surface tension. It is thus reasonable to expect surface tension to have little influence on the dynamics. However, in the last stages of the collapse of sub-micron sized bubbles, where high curvatures and small length scales are achieved, surface tension effects may become locally important. In addition, for the collapse of bubbles attached to the wall, representing the contact line accurately would require the inclusion of the capillary effects. Surface tension effects could be incorporated following the work of Schmidmayer *et al.* (2017).

Finally, the neighboring wall was assumed to be perfectly reflecting. Although this assumption is relevant to many applications, deformations of the neighboring solid can be important when simulating collapse near soft materials (e.g., UHMWPE, polyurea, soft tissue). The transmission of the pressure waves into the solid and the subsequent deflections, in particular recoil, are expected to lead to a less intense collapse. Accounting for such flow-structure interactions could also lead to additional effects such as cavitation near recoiling surfaces and localized heating in the possibly viscoelastic medium. A fully coupled fluid-solid-thermal approach may be required to compute the impact loads (Rodriguez & Johnsen, 2018). The results presented in this study, impact (high pressures) and thermal (high temperatures) loads due to the collapse of individual bubbles near a rigid wall, can be used to provide a better understanding of cavitation-induced erosion. However, to develop a comprehensive model that can predict pitting and mass loss in cavitation erosion, incorporation of material sciences is necessary in addition to flow-structure interaction.

7.2.2 Numerical framework

In recent years, Graphics Processing Units (GPU), typically used to handle computer graphics, have been utilized to perform fast and highly parallel vector operations, traditionally handled by the Central Processing Units (CPU). Owing to their effective speedup and energy efficiency com-

pared to CPUs, GPUs have become popular in scientific computing community and prevalent in recent supercomputers. Thus, a multi-GPU parallel paradigm could be a beneficial addition to the current computational framework to take advantage of the high speed, vectorized operations of GPUs. However, communication between GPUs is a challenge; commonly-used algorithms link each GPU to a CPU, and then communicate between the GPUs through the corresponding CPUs, which involves unnecessary memory copies. Thus, it is recommended to consider other approaches such as NVIDIA GPUDirect to perform communications directly between the GPUs, which dramatically reduces CPU overhead and the corresponding latency. Therefore, a computational code leveraging this parallel paradigm, can be used to perform future petascale simulations more efficiently.

Currently the interface capturing approach regularizes the interface over several cells. Throughout long simulations, numerical dissipation can accumulate across the material interface which is a linearly degenerate wave, and affect the dynamics. In addition, the incorporation of interfacial effects, such as surface tension, requires sharp interfaces. Thus, a sharpening approach like that of [Shyue & Xiao \(2014\)](#) could be implemented. However, special care must be taken when implementing such approaches, since the available techniques might violate conservation laws, and/or increase the computational cost.

Numerical simulations of compressible flows can be computationally expensive. However, in the case of cavitation bubble collapse, compressibility effects may be neglected during much of the growth phase and the collapse process. Therefore, introducing a model that can effectively switch between compressible and incompressible will improve the performance of the current method. For instance, a sharp interface approach for incompressible flows, which is computationally less expensive (e.g., Boundary Integral method for potential flow theory), could be used to simulate the flow initially; once compressibility effects become important, the appropriate compressible multiphase model could be activated, to represent the jet impact and shock propagation. This algorithm can substantially reduce the computational cost ([Chahine, 2014](#)).

7.2.3 Physical investigations

In the present study, simulations of a single bubble collapsing near a rigid wall were conducted. The results were used to develop universal scalings based on the initial stand-off distance and the pressure driving the collapse, in order to predict the single-bubble behavior. We found that a bubble with a high non-sphericity exhibits significant deviations from the behavior of spherical bubbles. For instance, the discrepancy between the scaling for the maximum wall pressure and the idealized spherical case is a manifestation of the non-spherical effects. Therefore, we recommend that future research efforts consider incorporating the non-spherical effects of the collapse into the provided scaling laws. The results would help quantify the effects of the bubble non-sphericity on collapse properties, and provide better estimations of the flow dynamics that can be directly used in many engineering applications.

We simulated the collapse of a bubble pair near a rigid wall to investigate the role of bubble-bubble interactions on collapse dynamics, and accordingly develop a model for the collapse of bubble clouds. However, the complex morphologies observed in the simulations made it particularly challenging to identify these interactions. Unlike the single bubble case, the dynamics of a bubble pair depend on at least three additional parameters (inter-bubble distance, relative size and angle), in addition to the stand-off distance and driving pressure. The results show that the dependence on even one of these parameters is complicated; predicting the dependence on all parameters is expected to be exceedingly challenging. The value of such high-resolution simulations to understand or predict the collapse of many bubbles (clouds) is questionable because of the complexity of the problem, i.e., too many parameters. As a result, modeling the behavior of clouds of bubbles in the context of erosion may require alternative approaches. One potential solution could be the implementation of machine learning techniques and data-based modal decomposition methods ([Taira *et al.*, 2017](#)) to model such non-linear flows. One could thus use highly resolved simulations of the collapse of bubble pairs as inputs to model the bubble-bubble/bubble-wall interactions, and the subsequent non-spherical effects on collapse dynamics. The results can be used to develop a

more comprehensive cloud model where the asymmetric nature of the collapse is not neglected.

Pervasive in nature and engineering, turbulence remains one of the outstanding problems in classical physics. Although investigated for decades, turbulent bubbly flows are poorly understood. Additionally, experimental investigations of such flows, especially at high Reynolds numbers, are tedious and expensive, and require specialized diagnostics. The current computational framework can be used to perform direct numerical simulation (DNS) of such flows, in which all dynamical scales of motion of the continuous phase are resolved. However, such calculations are computationally expensive, and require access to substantial computing allocations. Current limitations in computing power allow only incompressible simulations for relatively low Reynolds number ($Re \approx 8000$), simple geometries, short times, few bubbles (100) with negligible volumetric changes and bubble-turbulence interaction ([Lu & Tryggvason, 2013](#)).

APPENDIX A

Non-conservative transport equation for volume fraction

To derive the transport equations for the volume fraction formulation, we follow [Miller & Puckett \(1996\)](#) and start with Eq.(2.16), which can be expanded

$$\frac{\partial \alpha^{(k)}}{\partial t} + \frac{\partial(\alpha^{(k)} u_j)}{\partial x_j} = -\frac{\alpha^{(k)}}{\rho^{(k)}} \frac{\partial \rho^{(k)}}{\partial t} - \frac{\alpha^{(k)} u_j}{\rho^{(k)}} \frac{\partial \rho^{(k)}}{\partial x_j}. \quad (\text{A.1})$$

We define the isentropic bulk modulus for each fluid, $K_s^{(k)}$, assuming isotropic stresses during advection and isentropic processes in any compression of the individual components. These assumptions imply that the pressure change associated with compression of the bulk (∂p) is equal to the pressure change associated with compression of each components ($\partial p^{(k)}$). Then, $K_s^{(k)}$ can be defined as:

$$K_s^{(k)} = \left. \frac{\partial p}{\partial \ln \rho^{(k)}} \right|_s = \rho^{(k)} \left. \frac{\partial p}{\partial \rho^{(k)}} \right|_s = \rho^{(k)} (\alpha^{(k)})^2. \quad (\text{A.2})$$

Differentiating Eq. (2.6) with respect to pressure and assuming constant entropies for each fluid results in:

$$-\frac{1}{\rho} \left(\frac{1}{\rho} \left. \frac{\partial p}{\partial \rho} \right|_s \right) = - \sum_k \frac{z^{(k)}}{\rho^{(k)}} \left(\frac{1}{\rho^{(k)}} \left. \frac{\partial p}{\partial \rho^{(k)}} \right|_s \right). \quad (\text{A.3})$$

By combining Eqs. (A.2) and (2.6), the isentropic bulk modulus and sound speed of the mixture are:

$$\frac{1}{K_s} = \sum_k \frac{\alpha^{(k)}}{K_s^{(k)}}, \quad \frac{1}{\rho a^2} = \sum_k \frac{\alpha^{(k)}}{\rho^{(k)}(a^{(k)})^2}, \quad (\text{A.4})$$

thus recovering Wallis' relation (Wallis, 1969). According to the definition of isentropic bulk modulus and assuming pressure equilibrium between the phases, we can write $K_s \partial \rho / \rho = \partial p = \partial p^{(k)} = K_s^{(k)} \partial \rho^{(k)} / \partial \rho^{(k)}$. Using (2.16) yields:

$$\frac{\partial \alpha^{(1)}}{\partial t} + \frac{\partial(\alpha^{(1)} u_j)}{\partial x_j} = \frac{\alpha^{(1)} K_s}{K_s^{(1)}} \frac{\partial u_j}{\partial x_j}. \quad (\text{A.5})$$

Finally, substituting Eqs. (A.2) and (A.4) into Eq. (A.5) yields, after appropriate manipulations:

$$\frac{\partial \alpha^{(k)}}{\partial t} + u_j \frac{\partial \alpha^{(k)}}{\partial x_j} = \left(\frac{\alpha^{(k)} \alpha^{(k')} [\rho^{(k')} (a^{(k')})^2 - \rho^{(k)} (a^{(k)})^2]}{[\alpha^{(k)} \rho^{(k')} (a^{(k')})^2 + \alpha^{(k')} \rho^{(k)} (a^{(k)})^2]} \right) \frac{\partial u_j}{\partial x_j}, \quad (\text{A.6})$$

which can be further re-written as:

$$\frac{\partial \alpha^{(k)}}{\partial t} + \frac{\partial}{\partial x_j} \left(\alpha^{(k)} u_j \right) = \left[\frac{\alpha^{(k)} \rho^{(k')} (a^{(k')})^2}{\alpha^{(k)} \rho^{(k')} (a^{(k')})^2 + \alpha^{(k')} \rho^{(k)} (a^{(k)})^2} \right] \frac{\partial u_j}{\partial x_j}. \quad (\text{A.7})$$

BIBLIOGRAPHY

- Abgrall, R., & Perrier, V. 2006. Asymptotic expansion of a multiscale numerical scheme for compressible multiphase flow. *Multiscale Model. Simul.*, **5**, 84–115.
- Abgrall, Rémi. 1996. How to prevent pressure oscillations in multicomponent flow calculations: a quasi conservative approach. *J. Comput. Phys.*, **125**, 150–160.
- Allaire, G., Clerc, S., & Kokh, S. 2002. A five-equation model for the simulation of interfaces between compressible fluids. *J. Comput. Phys.*, **181**, 577–616.
- Ando, K., Colonius, T., & Brennen, C. E. Numerical simulation of shock propagation in a polydisperse bubbly liquid. *Intl J. Multiphase Flow*, **37**.
- Arndt, R. E. A. 1981. Cavitation in fluid machinery and hydraulic structures. *Annu. Rev. Fluid Mech.*, **13**, 273–328.
- Arndt, R. E. A. 2002. Cavitation in vortical flows. *Ann. Rev. Fluid Mech.*, **34**, 143–175.
- Baer, M. R., & Nunziato, J. W. 1986. A two-phase mixture theory for the deflagration-to-detonation transition (ddt) in reactive granular materials. *Int. J. Multiph. Flow*, **12**, 861–889.
- Ball, G.J., Howell, B.P., Leighton, T.G., & Schofield, M.J. 2000. Shock-induced collapse of a cylindrical air cavity in water: a free-lagrange simulation. *Shock Waves*, **10**, 265–276.
- Barajas, C., & Johnsen, E. 2017. The effects of heat and mass diffusion on freely oscillating bubbles in a viscoelastic, tissue-like medium. *J. Acoust. Soc. Am.*, **141**, 908–918.
- Barber, B. P., & Puttermann, S. J. 1991. Observation of synchronous picosecond sonoluminescence. *Nature*, **352**, 318–320.
- Beig, S. A., & Johnsen, E. 2015a. Maintaining interface equilibrium conditions in compressible multiphase flows using interface capturing. *J. Comput. Phys.*, **302**, 548–566.
- Beig, S. A., & Johnsen, E. 2015b. Temperature considerations in non-spherical bubble collapse near a rigid wall. **656**, 012044.
- Beig, S. A., Aboulhasanzadeh, B., & Johnsen, E. 2018. Temperatures produced by inertially collapsing bubbles near rigid surfaces. *Under review in J. Fluid Mech.*
- Benjamin, T. B., & Ellis, A. T. 1966. The collapse of cavitation bubbles and the pressure thereby produced against solid boundaries. *Phil. Trans. R. Soc. Lond.*, **260**, 221–240.

- Blake, J. R., & Gibson, D. C. 1987. Cavitation bubbles near boundaries. *Ann. Rev. Fluid Mech.*, **19**, 99–123.
- Blake, J. R., Taib, B. B., & Doherty, G. 1986. Transient cavities near boundaries. part 1. rigid boundary. *J. Fluid Mech.*, **170**, 479–497.
- Bourne, N. K., & Field, J. E. 1992. Shock-induced collapse of single cavities in liquids. *J. Fluid Mech.*, **244**, 225.
- Braconnier, B., & Nkonga, B. 2009. An all-speed relaxation scheme for interface flows with surface tension. *J. Comput. Phys.*, **228**, 5722–5739.
- Bremond, N., Arora, M., Ohl, C. D., & Lohse, D. 2006. Controlled multibubble surface cavitation. *Phys. Rev. Lett.*, **96**, 224501.
- Brennen, C. E. 1995. Cavitation and bubble dynamics. *Oxford University Press*.
- Brenner, M. P., Hilgenfeldt, S., & Lohse, D. 2002. Single-bubble sonoluminescence. *Rev. Mod. Phys.*, **74**, 425–484.
- Brujan, E. A., Keen, G. S., Vogel, A., & Blake, J. R. 2002. The final stage of the collapse of a cavitation bubble close to a rigid boundary. *Phys. Fluids*, **14**, 85–92.
- Brujan, E. A., Ikeda, T., & Matsumoto, Y. 2012. Shock wave emission from a cloud of bubbles. *Soft Matt.*, **8**, 5777–5783.
- Ceccio, S. L., & Brennen, C. E. 1991. Observations of the dynamics and acoustics of travelling bubble cavitation. *J. Fluid Mech.*, **233**, 633–660.
- Chahine, G. L. 2014. *Modeling of cavitation dynamics and interaction with material*. Dordrecht: Springer Netherlands. Pages 123–161.
- Chaves, H., Knapp, M., Kubitzek, A., Obermeier, F., & Schneider, T. 1995. Experimental study of cavitation in the nozzle hole of diesel injectors using transparent nozzles. *SAE Paper*, 950290.
- Coleman, A. J., Saunders, J. E., Crum, L. A., & Dyson, M. 1987. Acoustic cavitation generated by an extracorporeal shockwave lithotripter. *Ultrasound Med. Biol.*, **13**, 69–76.
- Coralic, V., & Colonius, T. 2014. Finite-volume weno scheme for viscous compressible multicomponent flows. *J. comput. phys.*, **274**, 95–121.
- Deplancke, T., Lame, O., Cavaille, J. Y., Fivel, M., Riondet, M., & Franc, J. P. 2015. Outstanding cavitation erosion resistance of Ultra High Molecular Weight Polyethylene (UHMWPE) coatings. *Wear*, **328**, 301–308.
- Duplat, J., & Villermaux, E. 2015. Luminescence from Collapsing Centimeter Bubbles Expanded by Chemical Reaction. *Phys. Rev. Lett.*, **115**, 1–5.
- Escaler, X., Egusquiza, E., Farhat, M., Avellan, F., & Coussirat, M. 2006. Detection of cavitation in hydraulic turbines. *Mech. Syst. Signal Process.*, **20**, 983 – 1007.

- Flannigan, D. J., & Suslick, K. S. 2005. Plasma formation and temperature measurement during single-bubble cavitation. *Nature (London)*, **434**, 52–55.
- Flannigan, D. J., & Suslick, K. S. 2010. Inertially confined plasma in an imploding bubble. *Nature Physics*, **6**, 598–601.
- Flannigan, D. J., Hopkins, S. D., Camara, C. G., Puttermann, S. J., & Suslick, K. S. 2006. Measurement of pressure and density inside a single sonoluminescing bubble. *Phys. Rev. Lett.*, **96**, 204301.
- Flåtten, T., Morin, A., & Munkejord, S. T. 2010. Wave propagation in multicomponent flow models. *SIAM J. Appl. Math.*, **70**, 2861–2882.
- Franc, J. P., & Michel, J. M. 2006. Fundamentals of cavitation. *Springer*.
- Franc, J. P., Riondet, M., Karimi, A., & Chahine, G. L. 2011. Impact load measurements in an erosive cavitating flow. *J Fluids Engng.*, **133**, 121301.
- Fujikawa, S., & Akamatsu, T. 1980. Effects of the non-equilibrium condensation of vapour on the pressure wave produced by the collapse of a bubble in a liquid. *J. Fluid Mech.*, **97**, 481–512.
- Fuster, D., & Colonius, T. 2011. Modelling bubble clusters in compressible liquids. *J. Fluid Mech.*, **688**, 352–389.
- Ganesh, Harish, Mkiharju, Simo A., & Ceccio, Steven L. 2016. Bubbly shock propagation as a mechanism for sheet-to-cloud transition of partial cavities. *J. Fluid Mech.*, **802**, 37–78.
- Gavaises, M., Papoulias, D., Andriotis, A., Giannadakis, E., & Theodorakakos, A. 2007. Link between cavitation development and erosion damage in diesel injector nozzles. *SAE Paper*.
- Giannadakis, E., Gavaises, M., & Arcoumanis, C. 2008. Modelling of cavitation in diesel injector nozzles. *Journal of Fluid Mechanics*, **616**, 153193.
- Gilmore, F. R. 1952. The growth or collapse of a spherical bubble in a viscous compressible liquid.
- Glimm, J., Grove, J. W., Li, X. L., Shyue, K. M., Zeng, Y., & Zhang, Q. 1998. Three-dimensional front tracking. *SIAM J. Sci. Comput.*, **19**, 703–727.
- Goncalvès, E., & Patella, R. F. 2010. Numerical study of cavitating flows with thermodynamic effect. *Comput. Fluids*, **39**, 99–113.
- Gottlieb, Sigal, & Shu, Chi Wang. 1996. Total variation diminishing Runge-Kutta schemes. *Math. Comput.*, **67**, 73–85.
- Han, B., Köhler, K., Jungnickel, K., Mettin, R., Lauterborn, W., & Vogel, A. 2015. Dynamics of laser-induced bubble pairs. *J. Fluid Mech.*, **771**, 706–742.
- Hansson, I., Kedrinskii, V., & Morsch, K. A. 1982. On the dynamics of cavity clusters. *J. Phys. D: Appl. Phys.*, **15**, 1725–1734.

- Harten, A., Lax, P. D., & Van Leer, B. 1983. On upstream differencing and godunov-type schemes for hyperbolic conservation laws. *SIAM Rev.*, **25**, 35–61.
- Hattori, S., Benitani, E., Ruan, W., Suda, Y., Takeuchi, R., & Iwata, T. 2015. Interaction of a strong shockwave with a gas bubble in a liquid medium: a numerical study. *J. Phys.: Conf. Ser.*, **656**, 012048.
- Hawker, N. a., & Ventikos, Y. 2012. Interaction of a strong shockwave with a gas bubble in a liquid medium: a numerical study. *J. Fluid Mech.*, **701**, 59–97.
- Hempel, C. R., Hall, T. L., Cain, C. A., Fowlkes, J. B., Xu, Z., & Roberts, W. W. 2011. Histotripsy fractionation of prostate tissue: local effects and systemic response in a canine model. *J. urol.*, **185**, 1484–1489.
- Henry de Frahan, M. T., Varadan, S., & Johnsen, E. 2015. A new limiting procedure for discontinuous galerkin methods applied to compressible multiphase flows with shocks and interfaces. *J. Comput. Phys.*, **280**, 489–509.
- Hickling, R. 1963. Effects of thermal conduction in sonoluminescence. *J. Acoust. Soc. Am.*, **35**, 967–974.
- Hickling, R., & Plesset, M. S. 1964. Collapse and rebound of a spherical bubble in water. *Phys. Fluids*, **7**, 7–14.
- Hu, X. Y., Khoo, B. C., Adams, N. A., & Huang, F. L. 2006. A conservative interface method for compressible flows. *J. Comput. Phys.*, **219**, 553–578.
- Jiang, G. S., & Shu, C. W. 1996. Efficient implementation of weighted eno schemes. *J. Comput. Phys.*, **126**, 202–228.
- Johnsen, E., & Colonius, T. 2006. Implementation of weno schemes in compressible multicomponent flow problems. *J. Comput. Phys.*, **219**, 715–732.
- Johnsen, E., & Colonius, T. 2009. Numerical simulations of non-spherical bubble collapse. *J. Fluid Mech.*, **629**, 231–264.
- Johnsen, E., & Ham, F. 2012. Preventing numerical errors generated by interface-capturing schemes in compressible multi-material flows. *J. Comput. Phys.*, **231**(17), 5705–5717.
- Johnsen, E., Larsson, J., Bhagatwala, A. V., Cabot, W. H., Moin, P., Olson, B. J., Rawat, P. S., Shankar, S. K., Sjögren, B., Yee, H. C., Xiaolin, Z., & Sanjiva, K. L. 2010. Assessment of high-resolution methods for numerical simulations of compressible turbulence with shock waves. *Journal of Computational Physics*, **229**, 1213–1237.
- Kapila, A. K., Menikoff, R., Bdzhil, J. B., Son, S. F., & Stewart, D. S. 2001. Two-phase modeling of deflagration-to-detonation transition in granular materials: Reduced equations. *Phys. fluids*, **13**, 3002–3024.
- Kawai, S., & Terashima, H. 2011. A high-resolution scheme for compressible multicomponent flows with shock waves. *Int. J. Numer. Methods Fluids*, **66**, 1207–1225.

- Kim, K. H., Chahine, G, Franc, J. P., & Karimi, A. 2014. Advanced experimental and numerical techniques for cavitation erosion prediction. *Springer*.
- Klaseboer, E., Hung, K. C., Wang, C., Wang, C. W., Khoo, B. C., Boyce, P., Debano, S., & Charlier, H. 2005. Experimental and numerical investigation of the dynamics of an underwater explosion bubble near a resilient/rigid structure. *J. Fluid Mech.*, **537**, 387–413.
- Knapp, R. T. 1955. Recent investigations of the mechanics of cavitation and cavitation damage. *Trans. ASME*, **77**, 1045–1054.
- Kokh, S., & Lagoutiere, F. 2010. An anti-diffusive numerical scheme for the simulation of interfaces between compressible fluids by means of a five-equation model. *J. Comput. Phys.*, **229**, 2773–2809.
- Kornfeld, M., & Suvorov, L. 1944. On the destructive action of cavitation. *J. Appl. Phys.*, **15**, 495–506.
- Kreeft, J. J., & Koren, B. 2010. A new formulation of kapilas five-equation model for compressible two-fluid flow, and its numerical treatment. *J. Comput. Phys.*, **229**, 6220–6242.
- Kröniger, D., Köhler, K., Kurz, T., & Lauterborn, W. 2010. Particle tracking velocimetry of the flow field around a collapsing cavitation bubble. *Exp. Fluids*, **48**, 395–408.
- Kubota, A. and Kato, H., Yamaguchi, H., & Maeda, M. 1989. Unsteady structure measurement of cloud cavitation on a foil section using conditional sampling technique. *J. Fluids Eng.*, **111**, 204–210.
- Lauer, E., Hu, X. Y., Hickel, S., & Adams, N. A. 2012. Numerical modelling and investigation of symmetric and asymmetric cavitation bubble dynamics. *Comput. Fluids*, **69**, 1–19.
- Lauterborn, W., & Bolle, H. 1975. Experimental investigations of cavitation-bubble collapse in the neighbourhood of a solid boundary. *J. Fluid Mech.*, **72**, 391–399.
- Lauterborn, W., & Kurz, T. 2010. Physics of bubble oscillations. *Rep. Prog. Phys.*, **73**, 106501.
- Le Métayer, O., & Saurel, R. 2016. The noble-abel stiffened-gas equation of state. *Phys. Fluids*, **28**, 046102.
- Le Métayer, O., Massoni, J., & Saurel, R. 2005. Modelling evaporation fronts with reactive rieemann solvers. *J. Comput. Phys.*, **205**, 567–610.
- Legay, M., Gondrexon, N., Le Person, S., Boldo, P., & Bontemps, A. 2011. Enhancement of heat transfer by ultrasound: review and recent advances. *Int. J. Chem. Eng.*, **670108**, 1–17.
- Lindau, O., & Lauterborn, W. 2003. Cinematographic observation of the collapse and rebound of a laser-produced cavitation bubble near a wall. *J. Fluid Mech.*, **479**, 327–348.
- Lohse, D. 2005. Sonoluminescence - Cavitation hots up. *Nature (London)*, **434**, 33–34.

- Lu, J., & Tryggvason, G. 2013. Dynamics of nearly spherical bubbles in a turbulent channel upflow. *J. Fluid Mech.*, **732**, 166–189.
- Maxwell, A. D., Cain, C. A., Duryea, A. P., Yuan, L., Gurm, H. S., & Xu, Z. 2009. Noninvasive thrombolysis using pulsed ultrasound cavitation therapy histotripsy. *Ultrasound Med. Biol.*, **35**, 1982–1994.
- McClintock, D. A., Riemer, B. W., Ferguson, P. D., Carroll, A. J., & Dayton, M. J. 2012. Initial observations of cavitation-induced erosion of liquid metal spallation target vessels at the spallation neutron source. *J. Nucl. Mater.*, **431**, 147–159.
- Miller, Gregory Hale, & Puckett, Elbridge Gerry. 1996. A high-order godunov method for multiple condensed phases. *J. Comput. Phys.*, **128**, 134–164.
- Movahed, P., & Johnsen, E. 2013. A solution-adaptive method for efficient compressible multifluid simulations, with application to the richtmyer–meshkov instability. *J. Comput. Phys.*, **239**, 166–186.
- Murrone, A., & Guillard, H. 2005. A five equation reduced model for compressible two phase flow problems. *J. Comput. Phys.*, **202**, 664–698.
- Naudé, C. F., & Ellis, A. T. 1961. On the mechanism of cavitation damage by nonhemispherical cavities collapsing in contact with a solid boundary. *J. Basic Engng.*, **83**, 648–656.
- Osher, S., & Sethian, J. A. 1988. Fronts propagating with curvature-dependent speed: algorithms based on hamilton-jacobi formulations. *J. comput. phys.*, **79**, 12–49.
- Pailiere, H., Corre, C., & Cascales, J. R. G. 2003. On the extension of the ausm+ scheme to compressible two-fluid models. *Comput. Fluids*, **32**, 891–916.
- Pelanti, M., & Shyue, K. M. 2014. A mixture-energy-consistent six-equation two-phase numerical model for fluids with interfaces, cavitation and evaporation waves. *J. Comput. Phys.*, **259**, 331–357.
- Perigaud, G., & Saurel, R. 2005. A compressible flow model with capillary effects. *J. Comput. Phys.*, **209**, 139–178.
- Petitpas, F., Massoni, J., Saurel, R., Lapebie, E., & Munier, L. 2009. Diffuse interface model for high speed cavitating underwater systems. *Int. J. Multiph. Flow*, **35**, 747–759.
- Philipp, A., & Lauterborn, W. 1998. Cavitation erosion by single laser-produced bubbles. *J. Fluid Mech.*, **361**, 75–116.
- Pishchalnikov, Y. A., Sapozhnikov, O. A., Bailey, M. R., Williams Jr., J. C., Cleveland, R. O., Colonius, T., Crum, L. A., Evan, A. P., & McAteer, J. A. 2003. Cavitation Bubble Cluster Activity in the Breakage of Kidney Stones by Lithotripter Shockwaves. *J. Endourol.*, **17**, 435–446.
- Plesset, M. S. 1949. The dynamics of cavitation bubbles. *J. Appl. Mech.*, **16**, 277–282.

- Plesset, M. S., & Chapman, R. B. 1971. Collapse of an initially spherical vapour cavity in the neighbourhood of a solid boundary. *J. Fluid Mech.*, **47**, 283–290.
- Plesset, M. S., & Prosperetti, A. 1977. Bubble dynamics and cavitation. *Ann. Rev. Fluid Mech.*, **9**, 145–185.
- Plesset, M. S., & Zwick, S. A. 1954. The growth of vapor bubbles in superheated liquids. *J. Appl. Phys.*, **25**, 493–500.
- Preece, C. M. 1979. Cavitation erosion. treatise on material science and technology. *Academic Press*, **16**, 249–308.
- Rayleigh, Lord. 1917. On the pressure developed in a liquid during the collapse of a spherical cavity. *Philos. Mag.*, **34**, 94–98.
- Reisman, G. E., Wang, Y. C., & Brennen, C. E. 1998. Observations of shock waves in cloud cavitation. *J. Fluid Mech.*, **355**, 255–283.
- Riemer, B. W., McClintock, D. A., Kaminskas, S., & Abdou, A. A. 2014. Correlation between simulations and cavitation-induced erosion damage in spallation neutron source target modules after operation. *J. Nucl. Mater.*, **450**, 183–191.
- Robinson, P. B., Blake, J. R., Kodama, T., Shima, A., & Tomita, Y. 2001. Interaction of cavitation bubbles with a free surface. *J. Appl. Phys.*, **89**, 8225–8237.
- Rodriguez, M., & Johnsen, E. 2018. A high-order, finite-difference approach for numerical simulations of shocks interacting with interfaces separating different linear viscoelastic materials. *In preparation for J. Comput. Phys.*
- Saurel, R., & Abgrall, R. 1999a. A multiphase godunov method for compressible multifluid and multiphase flows. *J. Comput. Phys.*, **150**, 425–467.
- Saurel, R., & Abgrall, R. 1999b. A simple method for compressible multifluid flows. *SIAM J. Sci. Comput.*, **21**, 1115–1145.
- Saurel, R., Cocchi, J. P., & Butler, P. B. 1999. Numerical study of cavitation in the wake of a hypervelocity underwater projectile. *J. Propul. Power*, **15**, 513–522.
- Saurel, R., Petitpas, F., & Abgrall, R. 2008. Modelling phase transition in metastable liquids: application to cavitating and flashing flows. *J. Fluid Mech.*, **607**, 313–350.
- Schmidmayer, K., Petitpas, F., Daniel, E., Favrie, N., & Gavrilyuk, S. 2017. A model and numerical method for compressible flows with capillary effects. *J. Comput. Phys.*, **334**, 468–496.
- Schmidt, S. J., Mihatsch, M. S., Thalhamer, M., & Adams, N. A. 2014. Assessment of erosion sensitive areas via compressible simulation of unsteady cavitating flows. *Springer Netherlands*, 329–344.

- Schnerr, G. H., Sezal, I. H., & Schmidt, S. J. 2008. Numerical investigation of three-dimensional cloud cavitation with special emphasis on collapse induced shock dynamics. *Phys. Fluids*, **20**, 040703.
- Seo, J. H., Lele, S. K., & Tryggvason, G. 2010. Investigation and modeling of bubble-bubble interaction effect in homogeneous bubbly flows. *Phys. Fluids*, **22**, 063302.
- Shu, C. W. 1998. Essentially non-oscillatory and weighted essentially non-oscillatory schemes for hyperbolic conservation laws. *Pages 325–432 of: Advanced numerical approximation of nonlinear hyperbolic equations*. Springer.
- Shukla, R. K. 2014. Nonlinear preconditioning for efficient and accurate interface capturing in simulation of multicomponent compressible flows. *J. Comput. Phys.*, **276**, 508–540.
- Shukla, R. K., Pantano, C., & Freund, J. B. 2010. An interface capturing method for the simulation of multi-phase compressible flows. *J. Comput. Phys.*, **229**, 7411–7439.
- Shyue, K. M. 1998. An Efficient Shock-Capturing Algorithm for Compressible Multicomponent Problems. *J. Comput. Phys.*, **142**, 208–242.
- Shyue, K. M. 1999. A fluid-mixture type algorithm for compressible multicomponent flow with van der waals equation of state. *J. Comput. Phys.*, **156**, 43–88.
- Shyue, K. M., & Xiao, F. 2014. An eulerian interface sharpening algorithm for compressible two-phase flow: the algebraic thinc approach. *J. Comput. Phys.*, **268**, 326–354.
- Supponen, O., Obreschkow, D., Tinguely, M., Kobel, P., Dorsaz, N., & Farhat, M. 2016. Scaling laws for jets of single cavitation bubbles. *J. Fluid Mech.*, **802**, 263–293.
- Supponen, O., Obreschkow, D., Kobel, P., Tinguely, M., Dorsaz, N., & Farhat, M. 2017. Shock waves from nonspherical cavitation bubbles. *Phys. Rev. Fluids*, **2**, 093601.
- Sussman, M. 2003. A second order coupled level set and volume-of-fluid method for computing growth and collapse of vapor bubbles. *J. Comput. Phys.*, **187**, 110–136.
- Taira, K., Brunton, S. L., Dawson, S., Rowley, C. W., Colonius, T., McKeon, B. J., Schmidt, O. T., Gordeyev, S., Theofilis, V., & Ukeiley, L. S. 2017. Modal analysis of fluid flows: An overview. *arXiv preprint arXiv:1702.01453*.
- Terashima, H., Kawai, S., & Koshi, M. 2013. Consistent numerical diffusion terms for simulating compressible multicomponent flows. *Computers & Fluids*, **88**, 484–495.
- Thompson, K. W. 1987. Time dependent boundary conditions for hyperbolic systems. *J. comput. phys.*, **68**, 1–24.
- Thompson, K. W. 1990. Time-dependent boundary conditions for hyperbolic systems, ii. *J. comput. phys.*, **89**, 439–461.
- Tiwari, A., Freund, J. B., & Pantano, C. 2013. A diffuse interface model with immiscibility preservation. *J. comput. phys.*, **252**, 290–309.

- Tiwari, A., Pantano, C., & Freund, J. B. 2015. Growth-and-collapse dynamics of small bubble clusters near a wall. *J. Fluid Mech.*, **775**, 1–23.
- Tomita, Y., & Shima, A. 1986. Mechanisms of impulsive pressure generation and damage pit formation by bubble collapse. *J. Fluid Mech.*, **169**, 535–564.
- Tomita, Y., Shima, A., & Sato, K. 1990. Dynamic behavior of two-laser-induced bubbles in water. *Appl. phys. lett.*, **57**, 234–236.
- Turangan, C. K., Jamaluddin, A. R., Ball, G. J., & Leighton, T. G. 2008. Free-lagrange simulations of the expansion and jetting collapse of air bubbles in water. *J. Fluid Mech.*, **598**, 1–25.
- Van Wijngaarden, L. 1968. On the equations of motion for mixtures of liquid and gas bubbles. *J. Fluid Mech.*, **33**, 465–474.
- Vlaisavljevich, E., Kim, Y., Owens, G., Roberts, W., Cain, C., & Xu, Z. 2014. Effects of tissue mechanical properties on susceptibility to histotripsy-induced tissue damage. *Phys. Med. Biol.*, **59**(2), 253–270.
- Vogel, A., Lauterborn, W., & Timm, R. 1989. Optical and acoustic investigations of the dynamics of laser-produced cavitation bubbles near a solid boundary. *J. Fluid Mech.*, **206**, 299–338.
- Wallis, G. B. 1969. One-dimensional two-phase flow. *McGraw-Hill, New York*.
- Xi, X., & Zhong, P. 2001. Dynamic photoelastic study of the transient stress field in solids during shock wave lithotripsy. *J. Acoust. Soc. Am.*, **109**, 1226–1239.
- Yu, T., Wang, Z., & Mason, T. J. 2004. A review of research into the uses of low level ultrasound in cancer therapy. *Ultrasonics Sonochem.*, **11**, 95–103.
- Zhang, D. Z., & Prosperetti, A. 1994. Ensemble phase-averaged equations for bubbly flows. *Phys. Fluids*, **6**, 2956–2970.